UCL Université catholique de Louvain

École polytechnique de Louvain (EPL)

epl

Development of a tight-binding model to study Hofstadter's butterfly in graphene on h-BN exhibiting a moiré pattern

Dissertation presented by
Nicolas MOREAU

for obtaining the Master's degree in
Physical Engineering

Supervisor(s)
Jean-Christophe CHARLIER

Reader(s)
Simon DUBOIS, Benoît HACKENS

Academic year 2016-2017

Acknowledgements

First, I want to thank Simon for all the time he spent for me during this year. I am deeply grateful to him for his availability to answer my questions, to modify quickly his code for solving the problems I faced, and finally for helping me construct my model. This work would not have been possible without him.

I also thank Professor Jean-Christophe Charlier for all his remarks and advice since the beginning of my master. HIs inputs have helped me greatly during these two last years, especially for this thesis. I am also grateful to him for having proposed to me this highly interesting subject which accords well with my interests.

I take this occasion to thank Professor Benoît Hackens for the time he spent constructing with me my doctorate project, as well as for the time he spent reading my work.

More than ever, I thank my parents for having supported me throughout my studies and in all my choices. My fulfillment in my studies and in my life, including the opening of fresh horizons, are also their success. And deeply I am grateful to my family for their encouragement.

Also, I thank all my friends, particularly Thérèse, for having made these five years of study the best of my life.

Finally, I thank Peter for his precious corrections that restore dignity to Shakespeare's language in my thesis.

Contents

Abstract

When submitted both to a magnetic field and a periodic potential, the energy spectrum of electrons exhibits a fractal-like pattern known as Hofstadter's butterfly. Proofs of the existence of this butterfly were reported in a moiré lattice of graphene on hexagonal-boron-nitride (hBN) in 2013.

In this master thesis, two main tight-binding (TB) models are developed to study the butterfly in similar moiré systems. The first model considers the effect of hBN as a periodic electrostatic potential that modifies the on-site terms of graphene TB Hamiltonian. The second model is based on a complete TB approach. Interactions between graphene and hBN are performed by interlayer bond energies. The values of those interlayer parameters have not yet been reported in literature. In this thesis, they are determined with DFT calculations.

Based on those two models, the electronic properties of graphene on hBN are discussed first. Characteristic features, such as the gap opening at the Dirac point, the appearance of secondary Dirac points, and the geometrical influence of the moiré pattern are properly described by the complete TB model. In the latter part of the thesis, the signature of the butterfly is highlighted and compared with corresponding experimental results.

Introduction

In a periodic lattice, energy of electrons is quantized in Bloch bands due to the presence of the periodic atomic potential. A magnetic field also leads to a quantization of energy into discrete energy levels, called Landau levels. Together, the effect of lattice quantization and magnetic quantization leads to a fractal-like energy spectrum. This recursive behaviour of energy was highlighted theoretically for the first time in 1976 by D.R. Hofstadter [1]. Due to the characteristic shape of the fractal-like graph, it is called Hofstadter's butterfly.

The appearance of a fractal-like spectrum depends on the ratio between two characteristic dimensions. These are the magnetic length and the unit cell area [2, 3]. By taking the size of a classical unit cell area, the magnetic field required to observe the recursive behaviour of energy is far too large. Nevertheless, by breaking the lattice symmetry resulting in the appearance of large supercells, the required magnetic field reaches values available in laboratory. As already proposed by Hofstadter in his paper [1], breaking the symmetry can be achieved by applying an external potential having the desired periodicity. Using this technique, experiments performed on two-dimensional electron gas (2DEG) in GaAs/AlGaAs heterostructures have highlighted the presence of Hofstadter's butterfly [4-6]. Since then, a new way to observe Hofstadter's butterfly has been discovered with the arrival of a material with great potential: graphene.

Graphene is a two-dimensional material composed of carbon atoms that form a honeycomb lattice. It was isolated from graphite for the first time in 2004 [7]. Graphene has exceptional electrical properties and is forseen as a predominant actor in electronics [8, 9]. However, when graphene is placed on a classical silicon-based substrate, its electronic properties are significantly lowered [10-12]. This problem has been overcome by using hexagonal-boron-nitride (hBN) as substrate [12-14]. hBN is composed of 2D atomic layers that are isomorphic to graphene, with a lattice mismatch of about 1.8% between the two lattices. When placed on hBN, graphene is extremely flat and its electronic conductivity is close to that in suspended graphene [15].

The lattice mismatch between the two lattices are of major interest for observation of Hofstadter's butterfly. Indeed, it breaks the graphene lattice symmetry, leading to a moiré pattern when graphene is placed on top of hBN [16-18]. Formation of supercells arises from the high periodicity of the moiré pattern and a fractal-like spectrum associated with the superstructure appears at achievable magnetic field. Two papers in 2013 reported the observation of the butterfly in a moiré superlattice [3, 19].

In this master thesis, I investigate the appearance of Hofstadter's butterfly in graphene from a theoretical point of view. Due to the high number of atoms in a moiré supercell, tight-binding (TB) formalism is used to study the behaviour of electrons [20]. The TB model is implemented by the code *SuperTB* developed by Simon Dubois at UCL. In this framework, I elaborate two models of interaction between the layers of graphene and hBN. The first model represents the influence of hBN on graphene with a periodic $1/r$ potential. The second is a complete TB model where the interactions between the two layers are given by hopping parameters [20], determined with DFT calculations [21]. These two models are complementary to other theoretical studies of graphene on hBN systems [22-30].

In chapter 1, I develop the theoretical background of the TB model. The discussion is illustrated theoretically with the case of graphene and numerically with two examples of implementation for a free graphene layer and a free hBN layer.

In chapter 2, I detail two quantization mechanisms. First the quantization due to the lattice periodicity is addressed. Then, the quantization due to a magnetic field is established for both classical conductors and graphene.

Chapter 3 presents the effect of the two quantizations considered together. First, the theory related to the construction of Hofstadter's butterfly; then the results in graphene obtained with numerical calculations. Finally, I present the experimental results reported in [3, 19], providing comparison for my theoretical results.

Chapter 4 details the two models used in this thesis. The three initial sections present and justify the major approximations and assumptions made on the geometry and the construction of the TB Hamiltonian. Then I concentrate on the potential model. At the end of the chapter, I detail the complete TB model for a simple graphene layer and for bilayer graphene (BLG).

Ultimately, in chapter 5, I present results obtained for the two models. The two models are presented following the same structure. First, I concentrate on the electronic properties of graphene under the influence of hBN. These properties are compared with experimental and theoretical results reported in the literature. I then present my results with magnetic field and I compare them with the experimental data presented at the end of chapter 3.

chapter 1

The tight-binding model for graphene

The theoretical study of material properties, such as electrical, mechanical or optical properties, is a complex and rich field of physics. The complexity of interactions between particles that constitute a material leads to unsolvable calculations, analytically and also numerically [21]. Approximations are thus necessary to build models that approach as close as possible to the behaviour of real materials. Computer development has allowed huge progresses in the understanding of materials behaviour, and also in the prediction of new materials. Materials simulation is now one of the most active fields of research in physics and in science in general [31]. Density functional theory (DFT), based on Hohenberg–Kohn theorems [32], is the most used method of simulation, because of its wide range of applications and its accuracy [33]. Appendix A briefly presents the DFT method.

In solid-state physics, whereas DFT leads to very good results for crystals, it can be used only on small unit cells due to the rapid increase of computation time with the number of atoms in the unit cell. Indeed, the computational complexity for a unit cell of N atoms, in a classical DFT method, is $\mathcal{O}(N^3)$ [34]. However, in the present work, it is necessary to consider large unit cells, containing thousands of atoms. The tight-binding model, another approximation, makes it possible to deal with such huge unit cells. Its complexity is $\mathcal{O}(N)$ [34, 35]. This model is developed in this chapter. First, a theoretical and general description of the model is made. Then, application of the model to graphene illustrates the theoretical discussion. Finally, an implementation of two materials is presented.

1.1 Generalities about the tight-binding method

The tight-binding method is based on the LCAO method [35]. The LCAO method (Linear Combination of Atomic Orbital) is used in chemistry to study electronic wave functions in a molecule. The method is built with the atomic orbitals of isolated atoms [36, 37]. The tight-binding method, based on the same idea, is applied to periodic structures. A huge improvement of the model was successed by Slater and Koster in 1954 [20] when they gave a general theory that considers all orbitals, as briefly discussed in section 1.1.2.

1.1.1 The tight-binding Hamiltonian

In this section, energy dispersion in crystal is described by using the tight-binding (TB) method. As always, the electrons in a crystal obey the Schrödinger equation

$$\hat{H}\,|\Psi\rangle = E\,|\Psi\rangle \tag{1.1}$$

where $\hat{H}$ is the Hamiltonian operator, $|\Psi\rangle$ the electronic wave function of the system and E the total energy of the electrons. It is important to note that the wave function $|\Psi\rangle$ has the periodicity of the lattice

and is repeated in each unit cell. Further, it is convenient to assume that there are M atoms in each unit cell. Moreover, in an atom labelled M, Γ_M orbitals are considered to play a role in the electrical properties of the studied material.

As for the LCAO theory, the starting point of the TB model is to consider that an electronic wave function in a crystal is given by the superposition of the wave functions of the isolated atoms. The first step is to decompose the total wave function Ψ as a linear combination of the periodic wave functions $\psi_{i\alpha}$. Here, i stands for the label of an atom in the unit cell ($1 \leqslant i \leqslant M$) and α stands for one orbital of this atom ($1 \leqslant \alpha \leqslant \Gamma_M$). Each $\psi_{i\alpha}$ is multiplied by a factor of proportionality a_i to give the linear combination

$$\Psi = \sum_{i,\alpha} a_{i\alpha} \psi_{i\alpha} \tag{1.2}$$

The second step is to express $\psi_{i\alpha}$, which is periodic, as a superposition of the wave functions of each corresponding atom. The wave function of the orbital α of an isolated atom i is called $\phi_{i\alpha}(\mathbf{r} - \mathbf{R}_i)$, where $\mathbf{R}_i$ stands for the positions of the atom i in one of the lattice unit cell. By applying Bloch's theorem [38], $\psi_{i\alpha}$ can be built with the functions $\phi_{i\alpha}(\mathbf{r} - \mathbf{R}_i)$ as [35, 20]

$$\psi_{i\alpha} = \frac{1}{N^{1/2}} \sum_{\mathbf{R}_i} \exp(i\mathbf{k} \cdot \mathbf{R}_i) \phi_{i\alpha}(\mathbf{r} - \mathbf{R}_i) \tag{1.3}$$

where N is the number of unit cells in the crystal.

The Schrödinger equation 1.1 can be developed thanks to the wave function found in equation 1.2. And by applying $\langle \psi_{j\beta} |$ to the left of the Schrödinger equation

$$\langle \psi_{j\beta} | \hat{H} \left(\sum_{i,\alpha} a_{i\alpha} | \psi_{i\alpha} \rangle \right) = E \langle \psi_{j\beta} | \sum_{i,\alpha} a_{i\alpha} | \psi_{i\alpha} \rangle \tag{1.4}$$

This relation can be rearranged as

$$\sum_{i,\alpha} a_{i\alpha} \langle \psi_{j\beta} | \hat{H} | \psi_{i\alpha} \rangle = E \sum_{i,\alpha} a_{i\alpha} \langle \psi_{j\beta} | \psi_{i\alpha} \rangle \tag{1.5}$$

The two following substitutions makes the notations easier

$$H_{j\beta i\alpha} \equiv \langle \psi_{j\beta} | \hat{H} | \psi_{i\alpha} \rangle \qquad \text{and} \qquad S_{j\beta i\alpha} \equiv \langle \psi_{j\beta} | \psi_{i\alpha} \rangle \tag{1.6}$$

The terms $H_{j\beta i\alpha}$ are called the *Hamiltonian matrix elements*. Indeed, by looking at equation 1.4, it appears that the application of $\langle \psi_{j\beta} |$ leads to $\sum_M \Gamma_M$ equations, and that the sum $\sum_{i,\alpha} a_{i\alpha} | \psi_{i\alpha} \rangle$ carries $\sum_M \Gamma_M$ elements. In other words, equation 1.4 is a matrix system that can be written as

$$H_{km} a_m = E S_{km} a_m \tag{1.7}$$

where the substitutions $i\alpha \rightarrow m$ and $j\beta \rightarrow k$ have been made, with $1 \leqslant k, m \leqslant \sum_M \Gamma_M$, to obtain a two dimensional matrix. By putting all the terms in the right side of the equation, the relation $(H_{km} - E S_{km}) a_m = 0$ appears. A direct implication of this expression is that the determinant of the matrix $\mathbf{H} - E\mathbf{S}$ must be zero, that is

$$\det(\mathbf{H} - E\mathbf{S}) = 0 \tag{1.8}$$

This is, in fact, an equation where the unknown is the energy E. The way to solve it is to diagonalise the matrix $\mathbf{H} - E\mathbf{S}$ to obtain the diagonal matrix $\mathbf{\Lambda}$. Indeed, their determinants are equal: $\det(\mathbf{H} - E\mathbf{S}) = \det(\mathbf{\Lambda})$. Thus, each diagonal term gives an equation $\lambda(E) = 0$. The solution of these equations are the eigenvalues ε_i of the Schrödinger equation 1.1. Each eigenvalue corresponds to an energy dispersion, also called energy band, of the system. Indeed, the components of $\mathbf{H}$ and $\mathbf{S}$ depend on the wavevector $\mathbf{k}$, as shown in the following section. The set of eigenvalues then depends on $\mathbf{k}$, too.

1.1.2 Slater-Koster parameters

The previous section detailed the calculation allowing extraction of the band structure of the studied material. However, the equation 1.8 that, once solved, gives the values of energies ε_i depends on $\mathbf{H}$ and $\mathbf{S}$. The purpose of this section is to go deeper in the study of those matrix elements, to extract what is known as the Slater-Koster coefficients [20]. By departing from relation 1.6 and by inserting relation 1.3, the terms $H_{j\beta i\alpha}$ and $S_{j\beta i\alpha}$ can be developed in real space as [39]

$$H_{j\beta i\alpha} = \frac{1}{N}\sum_{\mathbf{R}_j}\sum_{\mathbf{R}_i}\exp\left(i\mathbf{k}\cdot(\mathbf{R}_i-\mathbf{R}_j)\right)\int \phi^*_{j\beta}(\mathbf{r}-\mathbf{R}_j)\hat{H}\phi_{i\alpha}(\mathbf{r}-\mathbf{R}_i)\mathrm{d}\mathbf{r} \tag{1.9}$$

$$S_{j\beta i\alpha} = \frac{1}{N}\sum_{\mathbf{R}_j}\sum_{\mathbf{R}_i}\exp\left(i\mathbf{k}\cdot(\mathbf{R}_i-\mathbf{R}_j)\right)\int \phi^*_{j\beta}(\mathbf{r}-\mathbf{R}_j)\phi_{i\alpha}(\mathbf{r}-\mathbf{R}_i)\mathrm{d}\mathbf{r} \tag{1.10}$$

Due to the periodicity of the lattice, only the difference of positions $\mathbf{R} = \mathbf{R}_j - \mathbf{R}_i$ between two atoms matters. The position of atom i can be taken as reference, $\mathbf{R}_i = 0$. From this reference, the sum can be effectuated on the other atoms, at positions $\mathbf{R}_j$. If there are N unit cells in the crystal, each distance $\mathbf{R} = \mathbf{R}_j - \mathbf{R}_i$ is taken N times. Relation 1.9 and 1.10 can be simplified as [39]

$$H_{j\beta i\alpha} = \sum_{\mathbf{R}}\exp(-i\mathbf{k}\cdot\mathbf{R})\int \phi^*_{j\beta}(\mathbf{r}-\mathbf{R})\hat{H}\phi_{i\alpha}(\mathbf{r})\mathrm{d}\mathbf{r} \tag{1.11}$$

$$S_{j\beta i\alpha} = \sum_{\mathbf{R}}\exp(-i\mathbf{k}\cdot\mathbf{R})\int \phi^*_{j\beta}(\mathbf{r}-\mathbf{R})\phi_{i\alpha}(\mathbf{r})\mathrm{d}\mathbf{r} \tag{1.12}$$

In equation 1.12, the term

$$\int \phi^*_{j\beta}(\mathbf{r}-\mathbf{R})\phi_{i\alpha}(\mathbf{r})\mathrm{d}\mathbf{r} \tag{1.13}$$

is called the **overlap integral** and is denoted by s_{ij}. In equation 1.11, the term

$$\int \phi^*_{j\beta}(\mathbf{r}-\mathbf{R})\hat{H}\phi_{i\alpha}(\mathbf{r})\mathrm{d}\mathbf{r} \tag{1.14}$$

is called the **bond energy** or the **hopping parameter** or the **Slater-Koster parameter** and is denoted by $\gamma_{j\beta i\alpha}$, $t_{j\beta i\alpha}$ or $E_{j\beta i\alpha}$. This parameter gives the energy difference that occurs when bonding to atoms i and j. The higher this value, the greater the link between the two atoms. A high value of this parameter also indicates that an electron will easily move from atom i to atom j, by tunnelling from one orbital to the other. It implies that the further apart are the two atoms, the weaker is the hopping parameter.

The most general formulation of the hopping parameter is given by the Slater-Koster (SK) coefficients and has been introduced for the first time in 1954 [20]. They take into account the symmetries of orbitals and their spatial arrangement. An SK coefficient is composed of two kinds of terms. The first depends on the angle between the two atoms (given by l, m, n, the direction cosines). The second (denoted by Γ) gives the bond integrals between two orbitals. It also depends on the distance between the two atoms.

Taking the notations of the initial article [20], the orbitals s are denoted by s, the orbitals p by x, y and z, following their symmetry axis, and the orbitals d by xy, yz, zx, x^2-y^2, $3z^2-r^2$ where the polynomials have the same angle dependence as the orbitals. The bond integrals are denoted by $\Gamma_{\alpha\beta J}$ where α and β represent the orbital type of atoms i and j, and J represents the angular momentum of the bond (given by σ, π or δ). Finally, the angle dependence is expressed by the direction cosines l, m, n. A complete list of the SK parameters is given in table I of [20] and some are included in table 1.1.

1.1.3 The effect of a magnetic field

This section describes the effect of a magnetic field in the scope of the tight-binding model. The magnetic field acts on the hopping parameter of equation 1.14, that was expressed as

$$\gamma_{j\beta i\alpha} = \int \phi^*_{j\beta}(\mathbf{r}-\mathbf{R}_j)\hat{H}_0\phi_{i\alpha}(\mathbf{r}-\mathbf{R}_i)\mathrm{d}\mathbf{r} \tag{1.15}$$

$E_{s,s}$:	$\Gamma_{ss\sigma}$
$E_{x,x}$:	$l^2\Gamma_{pp\sigma} + (1-l^2)\Gamma_{pp\pi}$
$E_{x,3z^2-r^2}$:	$l[n^2 - \frac{1}{2}(l^2+m^2)]\Gamma_{pd\sigma} - \sqrt{3}ln^2\Gamma_{pd\pi}$
$E_{xy,yz}$:	$3lm^2n\Gamma_{dd\sigma} + ln(1-4m^2)\Gamma_{dd\pi} + ln(m^2-1)\Gamma_{dd\delta}$

Table 1.1: List of some Slater-Koster coefficients taken from table I in reference [20]. Orbitals s have a spherical symmetry. Therefore, the hopping parameter does not depend on the angle between two atoms. For the other orbitals, the number of symmetries is reduced and the angle between two atoms has an importance. The angle is given in term of the direction cosines l, m and n.

where $\hat{H}_0$ is the Hamiltonian without magnetic field. One can define the translation operator $\hat{T}_{\mathbf{R}}$ such that $\hat{T}_{\mathbf{R}}\phi(\mathbf{r}) = \phi(\mathbf{r}+\mathbf{R})$. This operator has the form

$$\hat{T}_{\mathbf{R}} = \exp\left(\frac{i}{\hbar}\hat{\mathbf{p}}\cdot\mathbf{R}\right) \tag{1.16}$$

where $\hat{\mathbf{p}} = -i\hbar\boldsymbol{\nabla}$ is the impulsion operator. Two important properties derive from this definition

$$\hat{T}^*_{\mathbf{R}} = \hat{T}_{-\mathbf{R}} \tag{1.17a}$$
$$\hat{T}_{\mathbf{R}}\hat{T}^*_{\mathbf{R}} = \mathbb{1} \tag{1.17b}$$

where $\mathbb{1}$ is the unity (neutral) operator. With the use of the translation operator, the relation 1.15 can be expressed as

$$\gamma_{j\beta i\alpha} = \int \hat{T}_{\mathbf{R}_j}\phi^*_{j\beta}(\mathbf{r})\ \hat{H}_0\ \hat{T}_{-\mathbf{R}_i}\phi_{i\alpha}(\mathbf{r})\mathrm{d}\mathbf{r} \tag{1.18}$$

Magnetic field derives from a more fundamental object, the vector potential **A add ref**, and is expressed as $\mathbf{B} = \boldsymbol{\nabla}\times\mathbf{A}$. With this definition, the impulsion operator of a particle with charge $-e$ can be generalized in its gauge-invariant form with the Pierls substitution [40],

$$\hat{\mathbf{p}} \ \rightarrow\ \hat{\mathbf{\Pi}} = \hat{\mathbf{p}} + e\mathbf{A}(\mathbf{r}) \tag{1.19}$$

By using this substitution in the expression 1.16 of the translation operator, the following equation is obtained [41]

$$\hat{T}_{\mathbf{R}}\phi(\mathbf{r}) = \exp\left(\frac{ie}{\hbar}\int_{\mathbf{r}}^{\mathbf{r}+\mathbf{R}}\mathbf{A}\cdot\mathrm{d}\mathbf{r}\right)\phi(\mathbf{r}+\mathbf{R}) \tag{1.20}$$

The presence of a magnetic field adds a phase to the wave function. This phase depends on the vector potential. The Hamiltonian $\hat{H}_0$ of equation 1.15 is modified as

$$\hat{H} = \frac{1}{2m}(\hat{\mathbf{p}} + e\mathbf{A}(\mathbf{r}))^2 \tag{1.21}$$

The hopping parameter of relation 1.18 becomes

$$\gamma_{j\beta i\alpha}(\mathbf{A}(\mathbf{r})) = \int \hat{T}_{\mathbf{R}_j}\phi^*_{j\beta}(\mathbf{r})\ \hat{H}\ \hat{T}_{-\mathbf{R}_i}\phi_{i\alpha}(\mathbf{r})\mathrm{d}\mathbf{r} \tag{1.22}$$

With the help of some algebra, this expression can be transformed as

$$\gamma_{j\beta i\alpha}(\mathbf{A}) = \exp\left(\frac{ie}{\hbar}\int_{\mathbf{R}_i}^{\mathbf{R}_j}\mathbf{A}\cdot\mathrm{d}\mathbf{r}\right)\int\phi^*_{j\beta}(\mathbf{r}-\mathbf{R}_j)\hat{H}_0\phi_{i\alpha}(\mathbf{r}-\mathbf{R}_i)\mathrm{d}\mathbf{r} \tag{1.23}$$

As a final result, the hopping parameter, in presence of a magnetic field, is transformed as [41]

$$\gamma_{j\beta i\alpha}(\mathbf{A}) = \exp\left(\frac{ie}{\hbar}\int_{\mathbf{R}_i}^{\mathbf{R}_j}\mathbf{A}\cdot\mathrm{d}\mathbf{r}\right)\gamma_{j\beta i\alpha} \tag{1.24}$$

1.1.4 The second quantization

In the previous sections, the tight-binding model has been developed in the frame of the first quantization. The purpose of this section is to express the tight-binding model in the second quantization formalism, as it is made in most of the recent literature [8]. A presentation of the second quantization formalism is made in appendix D. By departing from equation D.14 of appendix D and by using the notation developed in section 1.1.1, the Hamiltonian is expressed as

$$\hat{H} = \sum_{i\alpha,j\beta} \langle \phi_{j\beta} | \hat{\mathcal{H}}_{i\alpha,j\beta} | \phi_{i\alpha} \rangle c^{\dagger}_{j\beta} c_{i\alpha} \tag{1.25}$$

where $c^{\dagger}_{j\beta}$ creates an electron in orbital β of atom j, and $c_{i\alpha}$ annihilates an electron in orbital α of atom i. In other words, an electron hops from orbital $j\beta$ to orbital $i\alpha$. And the term $\langle \phi_{j\beta} | \hat{\mathcal{H}}_{i\alpha,j\beta} | \phi_{i\alpha} \rangle$ is the hopping parameter $t_{j\beta i\alpha}$, already presented in section D.14.

1.2 Derivation of the band structure of graphene

Graphene is a two-dimensional material, composed of carbon atoms organised in an honeycomb lattice as shown in figure 1.1a. It was produced for the first time in 2004 [7] and has been the subject of a high number of studies since then. Indeed, electrons in graphene have a specific behaviour, as detailed in section 1.2.3. First, the band structure of graphene is derived using the tight-binding model described in section 1.1. Then, the implications of the very specific band structure of graphene are discussed.

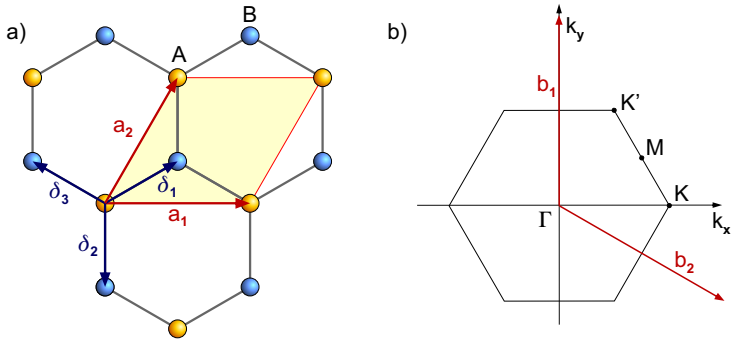

Figure 1.1: Structure of graphene. **(a)** Representation of the lattice in real space. Graphene is composed of two sublattices, in blue and yellow. The periodicity of the lattice is given by the lattice vectors $\mathbf{a}_1$ and $\mathbf{a}_2$ **(b)** Representation of the Brillouin zone in the reciprocal space. Four characteristic points of the Brillouin zone are denoted by Γ, M, K and K'.

1.2.1 The structure of graphene

The hexagonal structure of graphene is made possible by sp_2 hybridisation. Each carbon atom carries three sp_2 orbitals, which form an angle of 120° between each other, and one p_z orbital out of the graphene plane. The sp_2 orbitals form σ bonds, as shown in figure 1.2, and the p_z orbitals form π bonds, as shown in figure 1.2b. In graphene, electrons flow by hopping from one p_z orbital to another, through the π bonds [42, 43].

The two-dimensional periodic lattice of graphene can be described by its unit cell, represented in figure 1.1a. The unit cell contains two carbon atoms that form two sublattices, denoted by A and B. The primitive vectors $\mathbf{a}_1$ and $\mathbf{a}_2$ represented in figure 1.1a are given by the following expressions

$$\mathbf{a}_1 = a(1,0) \qquad \text{and} \qquad \mathbf{a}_2 = \frac{a}{2}(1,\sqrt{3}) \tag{1.26}$$

with a the lattice parameter of graphene, equals to 2,46 Å. In the same way, the reciprocal vectors $\mathbf{b}_1$ and $\mathbf{b}_2$ shown in figure 1.1b, can be found by following the condition $\mathbf{a}_i \cdot \mathbf{b}_j = 2\pi\delta_{ij}$. It gives

$$\mathbf{b}_1 = \frac{2\pi}{\sqrt{3}a}(\sqrt{3},-1) \qquad \text{and} \qquad \mathbf{b}_2 = \frac{2\pi}{\sqrt{3}a}(0,2) \tag{1.27}$$

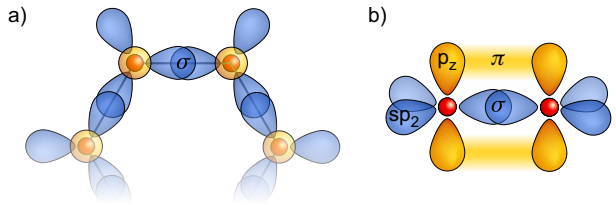

Figure 1.2: Description of the orbitals in graphene. **(a)** The hexagonal structure of graphene is achieved by σ bonds that form a 120° angle between each other. **(b)** Each carbon atom has three sp_2 orbitals and the p_z orbitals form π bonds with the neighbouring atom. The electrons in graphene circulate across the π bonds.

1.2.2 Tight-binding model for graphene

The first development of the band structure of graphene using tight-binding formalism was achieved by P.R. Wallace in 1947 [44]. A similar derivation of the band structure is presented in this section by finding the expression of the eigenvalues E of equation 1.8, $\det(\mathbf{H} - E\mathbf{S}) = 0$. The matrices H and S can be constructed from equations 1.11 and 1.12. In these equations the different orbitals $\phi_{i\alpha}$ and $\phi_{j\beta}$ must be considered, with i and j the label of the atoms in the unit cell, and α and β the labels of the orbitals.

As stated in section 1.2.1, we can assume that orbitals p_z are entirely at the origin of the conduction of the electrons. The labels α and β of $\phi_{i\alpha}$ and $\phi_{j\beta}$ thus account only for the orbitals p_z and are not included in the following expressions. This gives $\phi_{i\alpha} \equiv \phi_i$ and $\phi_{j\beta} \equiv \phi_j$. Because there are only two atoms per unit cell, the labels i and j of ϕ_i and ϕ_j can refer to the atom of lattice A (yellow in figure 1.1a) or to the atom of lattice B (blue in figure 1.1). Matrices H and S are then 2×2 matrices, expressed as

$$H = \begin{pmatrix} H_{AA} & H_{AB} \\ H_{BA} & H_{BB} \end{pmatrix} \qquad \text{and} \qquad S = \begin{pmatrix} S_{AA} & S_{AB} \\ S_{BA} & S_{BB} \end{pmatrix} \tag{1.28}$$

Equation 1.11 leads indeed to four equations, for H_{AA}, H_{AB}, H_{BA} and H_{BB}. However, these expressions only depend on the difference of distance $\mathbf{R}$ between the atoms. The term H_{AA} is thus equal to the term H_{BB} in the sense that these are exactly the same sublattices shifted by vector δ_1 in figure 1.1a. The terms H_{AB} and H_{BA} are also linked by the relation $H_{AB} = H_{BA}^*$. Therefore, the two equations 1.29 and 1.30 given below remain from system 1.28.

$$H_{AA} = H_{BB} = \sum_{\mathbf{R}_{AA'}} \exp(-i\mathbf{k}\cdot\mathbf{R}_{AA'}) \int \phi_A^*(\mathbf{r} - \mathbf{R}_{AA'}) \hat{H} \phi_A(\mathbf{r}) \mathrm{d}\mathbf{r} \tag{1.29}$$

with $\mathbf{R}_{AA'} = \mathbf{R}_{BB'} = n_1\mathbf{a}_1 + n_2\mathbf{a}_2$, the position vector between atom A (resp. B) of the reference unit cell and atom A' (resp. B') of the unit cell labelled (n_1, n_2).

$$H_{AB} = H_{BA}^* = \sum_{\mathbf{R}_{AB}} \exp(-i\mathbf{k}\cdot\mathbf{R}_{\mathbf{AB}}) \int \phi_B^*(\mathbf{r} - \mathbf{R}_{AB}) \hat{H} \phi_A(\mathbf{r}) \mathrm{d}\mathbf{r} \tag{1.30}$$

with $\mathbf{R}_{AB} = n_1\mathbf{a}_1 + n_2\mathbf{a}_2 + \delta_1$ and $\mathbf{R}_{BA} = n_1\mathbf{a}_1 + n_2\mathbf{a}_2 - \delta_1$, where δ_1 is the position vector between atoms A and B inside the same unit cell, as shown in figure 1.1a.

In a same way, there are four terms S_{AA}, S_{AB}, S_{BA} and S_{BB}. These are the overlap terms. The usual approximation is to neglect the off-diagonal terms that represent the overlap between the orbitals of remote atoms[42, 43]. That is, $S_{AB} = S_{BA} = 0$. The expression of S_{AA} and S_{BB} are also equal, for the same reasons invoked before to obtain equation 1.29. The expression 1.12 becomes

$$S_{AA} = S_{BB} = \sum_{\mathbf{R}} \exp(-i\mathbf{k}\cdot\mathbf{R}_{AA'}) \int \phi_A^*(\mathbf{r} - \mathbf{R}_{AA'}) \phi_A(\mathbf{r}) \mathrm{d}\mathbf{r} \tag{1.31}$$

In this expression, all the terms of the sum cancel for $A \neq A'$. By considering normalized wave functions, it then leads to the simple relation

$$S_{AA} = S_{BB} = \int \phi_A^*(\mathbf{r}) \phi_A(\mathbf{r}) \mathrm{d}\mathbf{r} = 1 \tag{1.32}$$

Using the properties that obtain relations 1.29, 1.30 and 1.32, and inserting equation 1.28 in equation 1.8, produces the following determinant

$$\det \begin{pmatrix} H_{AA} - E & H_{AB} \\ H_{AB}^* & H_{AA} - E \end{pmatrix} = 0 \tag{1.33}$$

There are two eigenvalues[1] $E_\pm$ that are given by

$$E_\pm = H_{AA} \pm |H_{AB}| \tag{1.34}$$

The last step is to develop the terms H_{AA} and H_{AB}. This can be achieved by developing the sum of equation 1.29. The first term is $\mathbf{R} = 0$. It corresponds to the on-site integral.

$$H_{AA}(\mathbf{R} = 0) \equiv E_0 = \int \phi_A^*(\mathbf{r}) \hat{H} \phi_A(\mathbf{r}) \mathrm{d}\mathbf{r} \tag{1.35}$$

This term is called E_0 as it is simply the expression of the energy of an isolated atom submitted to Hamiltonian $\hat{H}$. This energy will be taken as a reference and set to 0. The second step in developing equation 1.29 is to consider all the nearest atoms of the same sublattice, called the next-nearest neighbours. They are located at the set of positions $\mathbf{d}_{nn} = \{\pm\mathbf{a}_1,\ \pm\mathbf{a}_2,\ \pm\mathbf{a}_1 \mp \mathbf{a}_2\}$, shown in figure 1.1a. These positions are located at the same distance $|\mathbf{d}_{nn}|$ from the reference atom, thus the integral in equation 1.29 is the same for all the next-nearest neighbour atoms

$$\gamma_{nn} \equiv \int \phi_A^*(\mathbf{r} - \mathbf{d}_{nn}) \hat{H} \phi_A(\mathbf{r}) \mathrm{d}\mathbf{r} \tag{1.36}$$

γ_{nn} is the hopping parameter, already described in section 1.1.1, for the next-nearest neighbour. By introducing this parameter in equation 1.29 and by developing the sum with the set of vectors $\mathbf{d}_{nn}$ in the exponential, it gives this function [42, 44]

$$H_{AA'}(\mathbf{R} = \mathbf{d}_{nn}) = \gamma_{nn} \underbrace{\left(2\cos\left(\sqrt{3}k_x a\right) + 4\cos\left(\frac{\sqrt{3}}{2}k_x a\right)\cos\left(\frac{3}{2}k_y a\right)\right)}_{f(\mathbf{k})} \tag{1.37}$$

A similar development can be effectuated for all the atoms of the lattice. However, the value of the hopping parameter decreases with the distance between atoms. In this discussion, the hopping parameter for atoms further than the next-nearest neighbours are neglected.

The term H_{AB} of equation 1.30 can be developed in the same way. The first term of the sum is given for the nearest neighbours of the reference atom, given by the set of positions $\mathbf{d}_n = \{\delta_1,\ \delta_2,\ \delta_3\}$, shown in figure 1.1a. The integral of equation 1.30 gives

$$\gamma_n = \int \phi_B^*(\mathbf{r} - \mathbf{d}_n) \hat{H} \phi_A(\mathbf{r}) \mathrm{d}\mathbf{r} \tag{1.38}$$

By inserting this relation back into equation 1.30 and by setting the positions $\mathbf{d}_n$ in the exponential

$$|H_{AB}(\mathbf{R} = \mathbf{d}_n)|^2 = \gamma_n^2 \left(1 + 4\cos^2\left(\sqrt{3}k_x a\right) + 4\cos\left(\frac{\sqrt{3}}{2}k_x a\right)\cos\left(\frac{3}{2}k_y a\right)\right) \tag{1.39}$$

Looking at equation 1.37, it appears that the previous relation can be expressed as $|H_{AB}|^2 = \gamma_n^2(3 + f(\mathbf{k}))$. By inserting the three terms 1.35, 1.37 and 1.39 in equation 1.34, the eigenvalues are finally given by [42, 44]

$$E_\pm = \pm\gamma_n \sqrt{3 + f(\mathbf{k})} - \gamma_{nn} f(\mathbf{k}) \tag{1.40}$$

The plot corresponding to relation 1.40 is presented in figure 1.3. The presence of two atoms in the unit cell gives rise to two energy bands. One is the valence band, denoted π and shown in red in figure 1.3. The other is the conduction band, denoted π^*, shown in blue.

[1] The presence of two eigenvalues is logical as there are two atoms in the unit cell. This is discussed in section 2.1.1

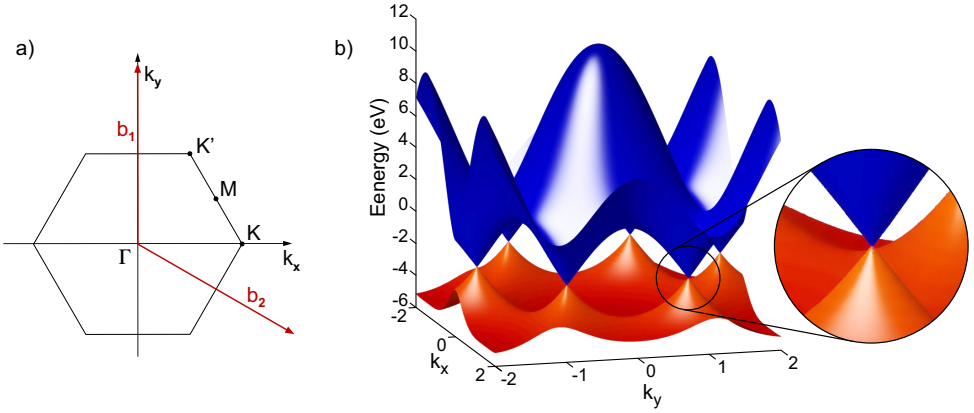

Figure 1.3: Band structure of graphene calculated until the next nearest-neighbours on basis of the equation 1.40. **(a)** Reciprocal lattice of graphene **(b)** The energy in the reciprocal lattice is a function of k_x and k_y. The red surface is the valence band and the blue surface is the conduction band. The hopping parameters used here are $\gamma_n = 2.8$ and $\gamma_{nn} = 0.2\gamma_n$. These values are given in reference [8]. The inset highlights the shape of the *Dirac cones* that are located at positions K and K' shown in a. The band structure has been plotted with Matlab. The code is presented in section E.1 of appendix E.

1.2.3 Emergence of Dirac fermions

By looking at figure 1.3b, six particular points appear at positions K and K' in the reciprocal lattice shown in figure 1.3a. At those points, valence band and conduction band exhibit a shape of cone and touch themselves at the point K (resp. K'). Graphene is thus a semi-metal. The positions of K and K' points are given by the following vectors in the reciprocal lattice

$$\mathbf{K} = \frac{2\pi}{\sqrt{3}a}(1,0) \qquad \text{and} \qquad \mathbf{K}' = \frac{\pi}{\sqrt{3}a}(1,\sqrt{3}) \tag{1.41}$$

By introducing these coordinates in equation 1.40, it gives $E_\pm = 0$, which corresponds effectively to the contact point between the valence and the conduction bands. In order to analyse the energy dispersion around the K points, we can construct the vector $\mathbf{k} = \mathbf{K} + \mathbf{q}$ with $|\mathbf{q}| \ll |\mathbf{K}|$. The coefficient $f(\mathbf{k})$ of equation 1.37 becomes

$$f(\mathbf{K}+\mathbf{q}) \simeq -3 + \frac{9}{2}a^2\mathbf{q}^2 \tag{1.42}$$

By considering only the influence of the nearest neighbour (that is, $\gamma_{nn} = 0$ in equation 1.36), the energy dispersion exclusively depends on $\mathbf{q}$

$$E_\pm(\mathbf{q}) \simeq \pm\hbar v_F|\mathbf{q}| \tag{1.43}$$

with the coefficient $v_F \equiv 3\gamma_0 a/(2\hbar)$ that expresses the Fermi velocity. The value of the Fermi velocity in graphene is generally estimated to $v_F \approx 10^6 m/s$ [8, 45].

Looking at equation 1.43, it appears very similar to the energy dispersion of a massless particle travelling at the speed of light c and expressed as

$$E = \hbar c k \tag{1.44}$$

The energy given in equation 1.44 is the eigenvalue of the Dirac Hamiltonian, used to represent relativistic particles. By analogy, we can assume that an electron close to a K point obeys the same formalism as a relativistic massless particle, with the major difference that the speed of light c present in equation (1.44) has to be replaced by the Fermi velocity v_F. Electrons close to the K point are then described by the Dirac equation for a massless fermion, called the Weyl equation, in two dimesions[2] [8, 46]. The Dirac Hamiltonian H_D has the form

$$H_D = v_F \boldsymbol{\sigma} \cdot \hat{\mathbf{p}} \tag{1.45}$$

[2] A brief introduction to the Dirac and the Weyl equations is in appendix B.

where $\hat{\mathbf{p}} = -i\hbar\boldsymbol{\nabla}$ is the impulsion operator and $\boldsymbol{\sigma} = (\sigma_x, \sigma_y)$ with σ_x and σ_y are the Pauli matrices

$$\sigma_x = \begin{pmatrix} 0 & 1 \\ 1 & 0 \end{pmatrix} \qquad \sigma_y = \begin{pmatrix} 0 & -i \\ i & 0 \end{pmatrix}$$

The Dirac equation $H_D\psi = E\psi$ is then expressed as

$$-i\hbar v_F \boldsymbol{\sigma} \cdot \boldsymbol{\nabla}\psi = E\psi \tag{1.46}$$

Wave function ψ is the one of an electron, called the *Dirac fermion*. In section B.2 of appendix B, it is shown that the eigenstate ψ of the Weyl equation has two components. In particle physics, these two components are the wave functions for spin up and spin down. However, in the case of graphene, these two components give what is called a *pseudo-spin* [46]. This pseudo-spin gives the sub-lattice of the particle. Instead of a spin up and down, there are sub-lattices A and B, shown in figure 1.1a, and the wave function is

$$\psi_n = \begin{pmatrix} \phi_n^A \\ \phi_n^B \end{pmatrix} \tag{1.47}$$

Another elegant parallel with the Dirac formalism used in particle physics can be done. One of the greatest successes of the Dirac equation was the prediction of the antiparticles (see appendix B). In graphene, the concept of antiparticles can be replaced by the concept of holes near the Dirac point. The holes appear in the valence band π when an electron jumps to the conduction band π^*. As a little anecdote, Dirac first interpreted antiparticles as holes [47]. He thought that the vacuum was filled with *negative energy states* and that couples of particles-antiparticles were created, in the same way as electron-hole pairs, thanks to the energy of a photon. It turned out to be a poor interpretation in the case of positrons, but it appears now to be very convenient in solid state physics.

1.3 Implementation of the tight-binding model

In this section, two examples illustrate the tight-binding model developed in section 1.1. The band structure and the density of state of graphene and hexagonal boron nitride (hBN) are derived. The code *SuperTB* used to build and compute the TB Hamiltonian is presented in appendix C.

1.3.1 The case of graphene

This section presents a simulation using a TB model with three-nearest neighbours approximation. The three hopping parameters of graphene (γ_n, γ_{nn} and γ_{nnn}) were found by adjusting the band structure to fit a DFT calculation as detailed in section C.2 of appendix C. Calculations were performed for different values of the lattice parameter a of graphene in order to determine the spacial dependence of the hopping parameters. Each hopping parameter is assumed to depend on the distance according to the function 1.48

$$\gamma(\mathbf{R}) = \gamma_0 \left[\alpha \exp(-\beta \left|\mathbf{R}\right|^{\eta})\right] \tag{1.48}$$

Table 1.2 presents the values of γ_0, α, β, η for the three hopping parameters γ_n, γ_{nn}, γ_{nnn}.

TB param.	γ_0 (eV)	α	β	η
γ_n	$-3.455 \cdot 10^{-3}$	1.766	-7.830	-0.597
γ_{nn}	-0.259	4.923	$1.290 \cdot 10^{-3}$	7.881
γ_{nnn}	-0.359	519.354	1.731	1.226

Table 1.2: Table of the coefficients of equation 1.48 that gives the hopping parameters for graphene found by adjusting the TB band structure on the DFT band structure.

The band structure of graphene has been computed with the code *SuperTB* with the parameters of table 1.2 for the stable lattice parameter of graphene $a = 2.46$ Å. The computation has been achieved by considering first the nearest neighbour only, then until the next-nearest neighbour and finally until the third nearest-neighbours. This is presented in figure 1.4a. The corresponding DOS are shown in figure 1.4b.

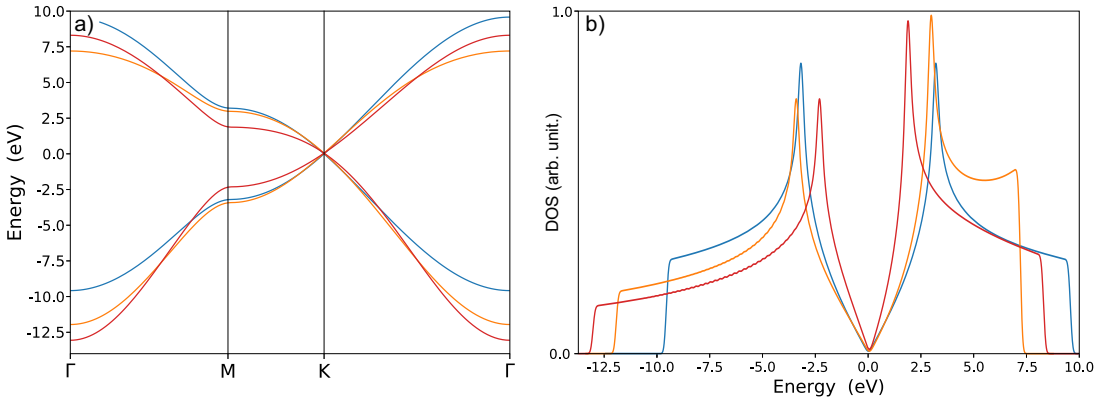

Figure 1.4: Electronic properties of graphene near the Fermi level (energy 0). Only the π orbitals were taken into account as justified in section 1.2. The properties for the nearest neighbour only (blue), until the next-nearest neighbour (orange) and finally until the third nearest-neighbours (red) are compared on **(a)** the band structure plotted on the path shown in figure 1.5b **(b)** the dennsity of state (DOS).

As discussed in section C.2, the band structure of graphene has been optimized for low energies around the Fermi level. The band structure between the two plateaus located at ± 2.5 eV above the M-point is well represented when considering the third nearest-neighbour (red curve). However, the band structure outside the interval between the plateaus is no more coherent with DFT calculations. In order to represent the band structure with more accuracy at low and large energies, more neighbours must be considered as well as the σ orbitals.

1.3.2 The case of hBN

Hexagonal boron nitride (hBN), as graphite, is formed by a staking of 2D layers. In each layer, atoms are disposed in a honeycomb lattice, as is the case for graphene (see section 1.2.1). The lattice parameter a of the stable configuration is 2.504 Å [48, 49]. Figure 1.5 represents the hBN lattice and its reciprocal lattice.

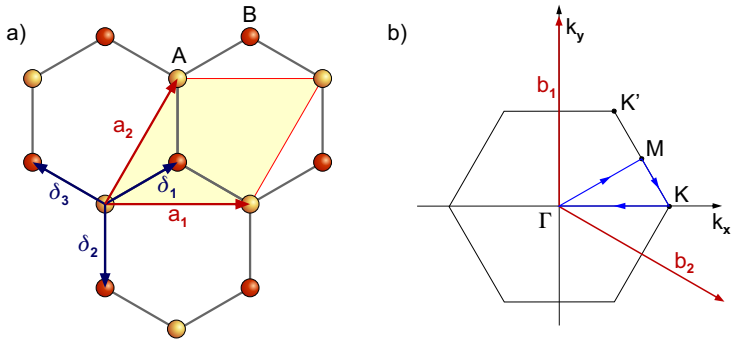

Figure 1.5: Structure of hexagonal boron nitride (hBN). **(a)** Representation of the lattice in real space. hBN is composed of boron atoms (yellow) that form sublattice A and of nitrogen atoms (red) that form sublattice B. The periodicity of the lattice is given by the lattice vectors $\mathbf{a}_1$ and $\mathbf{a}_2$. **(b)** Representation of the Brillouin zone in the reciprocal space. Four characteristic points of the Brillouin zone are denoted by Γ, M, K and K'.

The same method as presented for graphene in section 1.48 is used to compute the hBN band structure and DOS. The coefficients of equation 1.48 are given in table 1.3.

TB param.	γ_0 (eV)	α	β	η	type of liaison
γ_n	-2.851	0.011	-5.689	-0.619	B-N or N-B
γ_{nn}	-0.415	34.600	0.778	1.647	B-B or N-N
γ_{nnn}	-0.384	$5.079 \cdot 10^{-7}$	-20.441	-0.323	B-N or N-B

Table 1.3: Table of the hopping parameters of hBN found by adjusting the TB band structure on the DFT band structure.

The band structure and the DOS computed from the TB parameters of table 1.3 are shown in figure 1.6, by considering until the third-nearest neighbours. The free configuration of hBN is studied where the lattice parameter is $a = 2,504$ Å. As made for graphene, only the π orbitals are considered. The band gap that appears in hBN is about 4.7 eV, which is slightly lower than the experimental value of 5.955 eV reported in the literature [50-52].

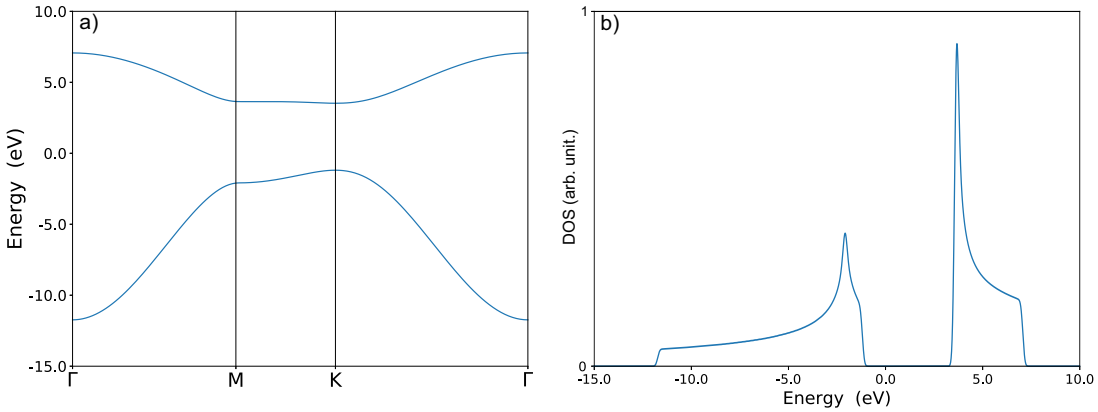

Figure 1.6: Electronic properties of hBN. hBN exhibits a band gap of about 4.7 eV. **(a)** Band structure of hBN. **(b)** Density of state (DOS) of hBN.

chapter 2

Energy quantizations in solid state physics

Quantum mechanics, as the name indicates, is the world of quantization. Solid-state physics, which obeys quantum formalism, is no exception to the rule. This chapter develops two effects that lead to quantization of the energy dispersion in solid-state physics. First, quantization due to the periodicity of the lattice is presented. Then, the effect of a magnetic field on energy is detailed.

2.1 The quantization in a periodic structure

In a single atom, each electron occupies an energy level, given by one eigenvalue of the atomic Hamiltonian. When N atoms are grouped together, the electrons that occupied the same state are not allowed to stay on the same energy level, due to the Pauli exclusion principle. The N degenerate energy levels split into N new levels, clustered around the initial level. When the number of atoms becomes extremely large, those levels form a continuum called an energy band. This section discusses the formation of those energy bands in a periodic structure.

2.1.1 The Bloch bands of the tight-binding model

The tight-binding model has been widely developed in chapter 1. Equation 1.8 states that energy dispersion for a unit cell containing N orbitals is given by a linear system of $N \times N$ matrices. The solution of the system consists then in N eigenvalues, each of them accounting for a periodic energy dispersion, called *energy band*. This short section focuses on the fact that the tight-binding model leads to quantization of the energy, with the creation of energy bands. The energy inside a band is continuous along k but is bounded between two limit energies. In this sense, the energy is quantized.

2.1.2 The effect of a weak potential

In this section, the effect of a weak potential V is studied. The development that follows is widely inspired by the book *Solid state physics*, by Ashcroft and Mermin [53]. The Hamiltonian of a free electron is given by $\hat{H} = \hat{\mathbf{p}}/2m$ and its energy is given by $\varepsilon^0_{\mathbf{k}} = \hbar^2\mathbf{k}^2/2m$. By adding the influence of the potential, the Schrödinger equation becomes

$$\frac{\hat{\mathbf{p}}}{2m}\psi_{\mathbf{k}} + V\psi_{\mathbf{k}} = E\psi_{\mathbf{k}} \tag{2.1}$$

In a crystal, the reciprocal lattice is periodic. The smallest pattern that is repeated periodically in all the space is called the Brillouin zone (BZ). The periodicity of the reciprocal space is given by the reciprocal lattice vectors denoted by $\mathbf{K}$. By Bloch's theorem [38], the wave function of an energy level can be written as [53]

$$\psi_{\mathbf{k}-\mathbf{K}}(\mathbf{r}) = \sum_{\mathbf{K}} C_{\mathbf{k}-\mathbf{K}} \exp(i(\mathbf{k}-\mathbf{K})\cdot\mathbf{r}) \tag{2.2}$$

where $\mathcal{C}_{\mathbf{k}-\mathbf{K}}$ is the Fourier transform of the wave function, discretized due to the periodicity of the crystal. In the reciprocal space, Hamiltonian 2.1 for the periodic lattice becomes

$$\left(\varepsilon^0_{\mathbf{k}-\mathbf{K}} - E\right)\mathcal{C}_{\mathbf{k}-\mathbf{K}} + \sum_{\mathbf{K}'} \mathcal{V}_{\mathbf{K}'-\mathbf{K}}\mathcal{C}_{\mathbf{k}-\mathbf{K}'} = 0 \tag{2.3}$$

where $\varepsilon^0_{\mathbf{k}-\mathbf{K}} = \hbar(\mathbf{k}-\mathbf{K})^2/2m$ is the energy of the free electron, $\mathcal{V}_{\mathbf{k}}$ is the Fourier transform of the potential V and the sum corresponds to the discrete convolution between $\mathcal{V}_{\mathbf{k}}$ and $\mathcal{C}_{\mathbf{k}-\mathbf{K}}$.

Here, the case of two electrons is studied in the presence of the weak potential. The two electrons belong to different BZs, located at positions $\mathbf{K}_1$ and $\mathbf{K}_2$ in the reciprocal space. When the electrons are free, their behaviour is given by equation 2.2 with all the coefficients $\mathcal{C}_{\mathbf{k}-\mathbf{K}} = 0$ for $\mathbf{K} \neq \mathbf{K}_1$ (resp. $\mathbf{K}_2$). Their energies are then given by $\varepsilon^0_{\mathbf{k}-\mathbf{K}_1}$ and $\varepsilon^0_{\mathbf{k}-\mathbf{K}_2}$. This is shown in figure 2.1.

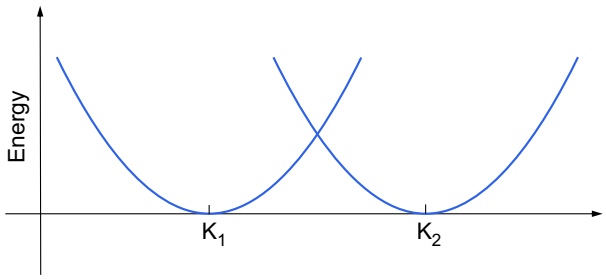

Figure 2.1: One-dimensional representation of the energies $\varepsilon^0_{\mathbf{k}-\mathbf{K}_1}$ and $\varepsilon^0_{\mathbf{k}-\mathbf{K}_2}$ of two free electrons. The energy dispersions are quadratic. The vectors $\mathbf{K}_1$ and $\mathbf{K}_2$ indicate the Brillouin zone (BZ) of each electron.

The hypothesis of a weak potential is given by the condition [53]

$$\left|\varepsilon^0_{\mathbf{k}-\mathbf{K}_{1,2}} - \varepsilon^0_{\mathbf{k}-\mathbf{K}'}\right| \gg \mathcal{V} \qquad \text{for } \mathbf{K}' \neq \mathbf{K}_1, \mathbf{K}_2 \tag{2.4}$$

With the presence of the potential, the eigenfunctions $\psi_{\mathbf{k}}$ change and the coefficients $\mathcal{C}_{\mathbf{k}-\mathbf{K}}$ with $\mathbf{K} \neq \mathbf{K}_1, \mathbf{K}_2$ are now of order $\mathcal{O}(\mathcal{V})$. By developing equation 2.3 for the first electron,

$$\left(E - \varepsilon^0_{\mathbf{k}-\mathbf{K}_1}\right)\mathcal{C}_{\mathbf{k}-\mathbf{K}_1} = \mathcal{V}_{\mathbf{K}_2-\mathbf{K}_1}\mathcal{C}_{\mathbf{k}-\mathbf{K}_2} + \sum_{\mathbf{K}'\neq\mathbf{K}_1,\mathbf{K}_2} \underbrace{\mathcal{V}_{\mathbf{K}'-\mathbf{K}}\mathcal{C}_{\mathbf{k}-\mathbf{K}'}}_{\mathcal{O}(\mathcal{V}^2)} \tag{2.5}$$

Because the last term is of order $\mathcal{O}(\mathcal{V}^2)$, it can be neglected, as made below in equation 2.6a. The same equation can be derived for the second electron, as written in equation 2.6b. By making the substitutions $\mathbf{q} = \mathbf{k} - \mathbf{K}_1$ and $\mathbf{K} = \mathbf{K}_1 - \mathbf{K}_2$, the two following equations can be found

$$\left(E - \varepsilon^0_{\mathbf{K}}\right)\mathcal{C}_{\mathbf{K}} = \mathcal{V}_{\mathbf{K}}\mathcal{C}_{\mathbf{q}-\mathbf{K}} \tag{2.6a}$$

$$\left(E - \varepsilon^0_{\mathbf{q}-\mathbf{K}}\right)\mathcal{C}_{\mathbf{q}-\mathbf{K}} = \mathcal{V}^*_{\mathbf{K}}\mathcal{C}_{\mathbf{K}} \tag{2.6b}$$

The potential term in the second equation comes from the property of the Fourier transform $\mathcal{V}_{-\mathbf{K}} = \mathcal{V}^*_{\mathbf{K}}$. This system finally gives the solution [53]

$$E = \frac{1}{2}\left(\varepsilon^0_{\mathbf{q}} + \varepsilon^0_{\mathbf{q}-\mathbf{K}}\right) \pm \sqrt{\left(\frac{\varepsilon^0_{\mathbf{q}} - \varepsilon^0_{\mathbf{q}-\mathbf{K}}}{2}\right)^2 + |\mathcal{V}_{\mathbf{K}}|^2} \tag{2.7}$$

This expression indicates that the effect of the weak potential is visible when the values $\varepsilon^0_{\mathbf{q}}$ and $\varepsilon^0_{\mathbf{q}-\mathbf{K}}$ are close. In the case of free electrons, the weak potential opens gaps at the borders of the BZ (the Bragg plane), where $|\mathbf{q}| \sim |\mathbf{K} - \mathbf{q}|$. In the Bragg plane, the opening of the gaps leads to a vanishing derivative of energy, $\partial E/\partial \mathbf{q} = 0$. This condition is indispensable to ensure the continuity of energy dispersion, and its derivative, in the periodic lattice. This continuity leads to the formation of energy bands, that is, to quantization of electrons energy in the periodic structure. This is shown in figure 2.2.

The conclusion of expression 2.7 can be generalized further than the case of free electrons. The term $\varepsilon^0_{\mathbf{k}}$ then accounts for the energy dispersion of an electronic band without the application of the potential V. As for the free electrons, the effect of the weak potential is visible when the functions $\varepsilon^0_{\mathbf{q}}$ and $\varepsilon^0_{\mathbf{q}-\mathbf{K}}$ are close, that is, where tthe graph trace lines of the energy bands cross. It induces the opening of gaps at the crossings. This is of major interest in further discussions.

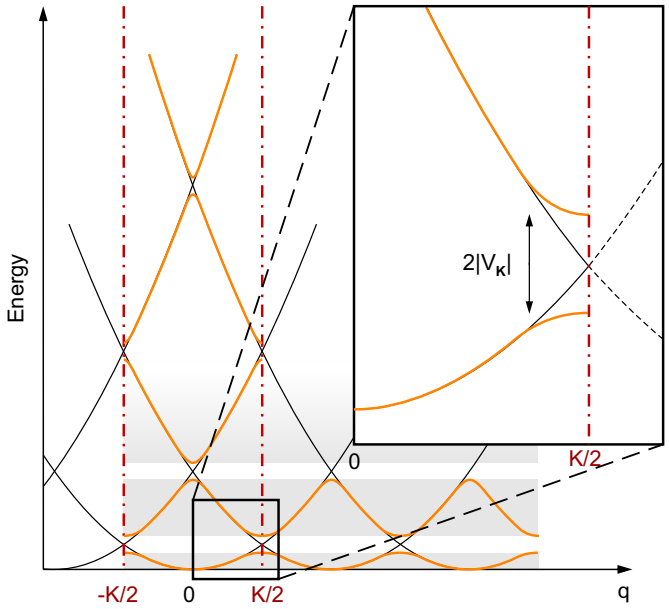

Figure 2.2: Representation of the one-dimensional energy dispersion (ED) of electrons under a weak potential. The thin black lines represent the ED of free electrons centered in successive BZs. The limits of the BZ are marked with dotted red lines and are positioned in $\pm\mathbf{K}/2$. The orange lines represent the ED of an electron under a weak potential. The effect of the potential leads to the formation of energy bands, shown in grey. This is due to gaps opening at the borders of the BZ. The inset zooms on one gap that presents an opening equal to $2\mathcal{V}_{\mathbf{K}}$. Inspired by [53].

2.2 The effect of a strong magnetic field

In the previous section, quantization due to a periodic lattice was presented. When a strong magnetic field is applied to a gas of electrons, their energy is also quantized [54-57]. For the following developments, the Drude model will be used [58]. This model considers a free electron gas; the influence of the nuclei potentials is then neglected. The electron behaviour is also studied in a constant magnetic field oriented along the z-axis, B_z. As a final comment, the movement of electrons is only considered along the coordinates x and y, perpendicular to the magnetic field. This is because the magnetic field does not influence the behaviour of electrons that displace in the same direction as the field.

In this section, the influence of a magnetic field on an electronic system is developed first in the second quantization formalism. Then, this formalism is applied for classical electrons and, finally, for Dirac fermions presented in section 1.2.3.

2.2.1 Electrons and magnetic field in the second quantization formalism

This section develops the tools used to express the quantization of classical and relativistic electrons. The starting point of the development is the Peierls substitution of relation 1.19 of section 1.1.3

$$\hat{\mathbf{p}} \;\rightarrow\; \hat{\mathbf{\Pi}} = \hat{\mathbf{p}} + e\mathbf{A}(\mathbf{r}) \tag{2.8}$$

When no magnetic field is applied, the impulsion operators along the different directions of space commute [59] as, for example, $[\hat{p}_x, \hat{p}_y] = 0$. The impulsions along different directions are then totally decorrelated. This is not the case when a magnetic field is added. The commutation relation for the gauge invariant form of the impulsion operator, for coordinates x and y, becomes [43]

$$[\hat{\Pi}_x, \hat{\Pi}_y] = -ie\hbar\left(\frac{\partial A_y}{\partial x} - \frac{\partial A_x}{\partial y}\right) = ie\hbar B_z \tag{2.9}$$

The impulsion terms along x and y are not decorrelated any more. A constrain is added and is at the origin of the energy quantization of the electronic system. Furthermore, when a conduction electron is in a magnetic field, the lattice length a has to be compared to the magnetic length, defined as [3, 43]

$$l_B = \sqrt{\frac{\hbar}{eB_z}} \tag{2.10}$$

When the magnetic field increases, with l_B becoming comparable to length a, the effect of the lattice cannot be neglected, making the Drude model invalid. This remark is the subject of chapter 3. Equation 2.9 can be expressed in terms of the magnetic length

$$[\hat{\Pi}_x, \hat{\Pi}_y] = -i\frac{\hbar^2}{l_B^2} \tag{2.11}$$

In appendix D, creation and annihilation operators are developed. These operators can be constructed by using the expression of the gauge invariant impulsion operator of equation 2.8,

$$a = \frac{l_B}{\sqrt{2}\hbar}(\hat{\Pi}_x - i\hat{\Pi}_y) \qquad \text{and} \qquad a^\dagger = \frac{l_B}{\sqrt{2}\hbar}(\hat{\Pi}_x + i\hat{\Pi}_y) \tag{2.12}$$

As detailed in equations D.7 and D.12, creation and annihilation operators created in expression 2.12 obey given commutation relations. In this case, the commutation relation is

$$[a, a^\dagger] = 1$$

This is an anti-commutator, indicating that the system is bosonic, as described by expression D.7. The final step to express Π_x and Π_y in terms of a and $a^\dagger$ is

$$\hat{\Pi}_x = \frac{\hbar}{\sqrt{2}l_B}(a^\dagger + a) \qquad \text{and} \qquad \hat{\Pi}_y = \frac{\hbar}{i\sqrt{2}l_B}(a^\dagger - a) \tag{2.13}$$

These two relations have major importance for the next two sections.

2.2.2 Quantization for classical electrons

This section describes the behaviour of electrons in a magnetic field. Because we work with the Drude model that considers a free electron gas, the electronic Hamiltonian is expressed as

$$\hat{H} = \frac{\hat{\mathbf{p}}^2}{2m}$$

with $\hat{\mathbf{P}} = -i\hbar\boldsymbol{\nabla}$ the impulsion operator. With the Peierls substitution of equation 2.8, the Hamiltonian of an electron in a magnetic field then becomes

$$H = \frac{\hat{\mathbf{\Pi}}^2}{2m} = \frac{1}{2m}\left(\hat{\mathbf{p}} + e\hat{\mathbf{A}}(\mathbf{r})\right)^2 \tag{2.14}$$

The presence of the vector potential in this Hamiltonian is at the origin of the energy quantization, for the reason explained in the previous section. Because only the x and y components of displacement are considered, equation 2.14 becomes

$$H = \frac{1}{2m}\left(\hat{\Pi}_x^2 + \hat{\Pi}_y^2\right) \tag{2.15}$$

By using expression 2.13 and the fact that $aa^\dagger + a^\dagger a = 2a^\dagger a + [a, a^\dagger]$, equation 2.15 can be expressed in terms of creation and annihilation operators as

$$H = \frac{\hbar^2}{ml_B^2}\left(a^\dagger a + \frac{1}{2}\right) \tag{2.16}$$

The term $a^\dagger a$ is equivalent to the occupation number operator $\hat{n}$ of equation D.9.

From equation D.3, the eigenvalues of Hamiltonian 2.16 are

$$E_n = \frac{\hbar^2}{ml_B^2}\left(n + \frac{1}{2}\right) \tag{2.17}$$

It corresponds to quantized energies, as predicted at the beginning of the section. These quantized energies are called **Landau levels**. Each level corresponds to a label n. The distance between two levels is proportional to the magnetic field B_z, indeed, $\hbar/ml_B^2 = eB_z/m$. The result 2.17 is represented in figure 2.3.

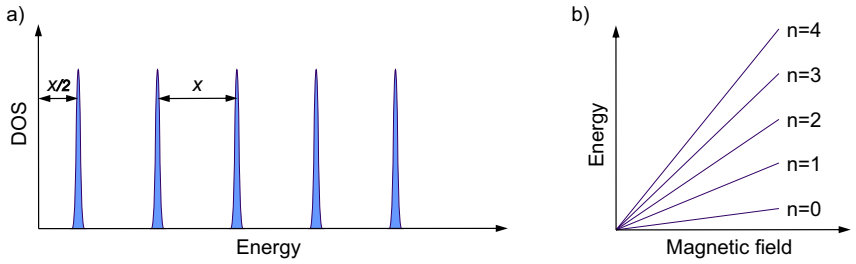

Figure 2.3: Representation of the Landau levels (LL's) of equation 2.17 **(a)** Density of state (DOS) as a function of energy E. The sharp peaks represent LLs. The LLs are separated by the distance $x = \hbar^2/ml_B^2$. **(b)** Evolution of quantized energy levels as a function of the magnetic field. Each LL E_n is labelled by its value of n.

2.2.3 Quantization for Dirac fermions

Section 1.2.3 discusses the behaviour of electrons in graphene, near the Fermi level which gives rise to Dirac fermions. This section develops Landau quantization in Dirac formalism. The first step is to consider the Hamiltonian for Dirac fermions expressed by equation 1.45

$$H_D = v_F \boldsymbol{\sigma} \cdot \hat{\mathbf{p}} \tag{2.18}$$

The Peierls substitution of equation 2.8 is used to add the effect of the magnetic field in the Dirac Hamiltonian

$$H_D = v_F \begin{pmatrix} 0 & \Pi_x - i\Pi_y \\ \Pi_x + i\Pi_y & 0 \end{pmatrix} \tag{2.19}$$

By using expression 2.12, the Dirac Hamiltonian can be written in term of annihilation and creation operators as [43]

$$H_D = \sqrt{2}\frac{\hbar v_F}{l_B}\begin{pmatrix} 0 & a \\ a^\dagger & 0 \end{pmatrix} \tag{2.20}$$

As discussed in section 1.2.3, the eigenvector ψ_n of the Dirac Hamiltonian for massless particles has two components which are the wave functions of lattices A and B. It is expressed by the relation (1.47)

$$\psi_n = \begin{pmatrix} \phi_n^A \\ \phi_n^B \end{pmatrix} \tag{2.21}$$

The Dirac equation for Hamiltonian 2.20 is given by $H_D\psi_n = E_n\psi_n$ where E_n are the eigenvalues of the system. The sublattices A and B give the two equations

$$\frac{\sqrt{2}\hbar v_F}{l_B} a\phi_n^B = E_n\phi_n^A \qquad \text{and} \qquad \frac{\sqrt{2}\hbar v_F}{l_B} a^\dagger\phi_n^A = E_n\phi_n^B \tag{2.22}$$

This leads to a relation for the lattice B only

$$a^\dagger a \phi_n^B = \frac{1}{2}\left(\frac{E_n l_B}{\hbar v_F}\right)^2 \phi_n^B \tag{2.23}$$

And the term $a^\dagger a$ is the occupation number operator $\hat{n}$ of equation D.9. From equation D.3, the energies E_n of Hamiltonian 2.20 are

$$E_n^2 = 2\left(\frac{\hbar v_F}{l_B}\right)^2 n \tag{2.24}$$

Finally, by expressing magnetic length as a function of the magnetic field, $l_B = \sqrt{\frac{\hbar}{eB_z}}$, energies are given by [43]

$$E_n = \pm v_F \sqrt{2\hbar e}\sqrt{nB_z} \tag{2.25}$$

As obtained in section 2.2.2, the energy of the system is quantized in Landau levels E_n. They are represented in figure 2.4. Many observations can be made about this figure. First, the most striking difference with equation 2.17 is the term $\sqrt{nB_z}$ that is not linear anymore. Secondly, there are not only positive values, as was the case for classical electrons of section 2.2.2. Positive Landau levels (LLs) correspond to electrons of the conduction band π represented in figure 1.3, whereas negative LLs correspond to holes of the valence band π^*.

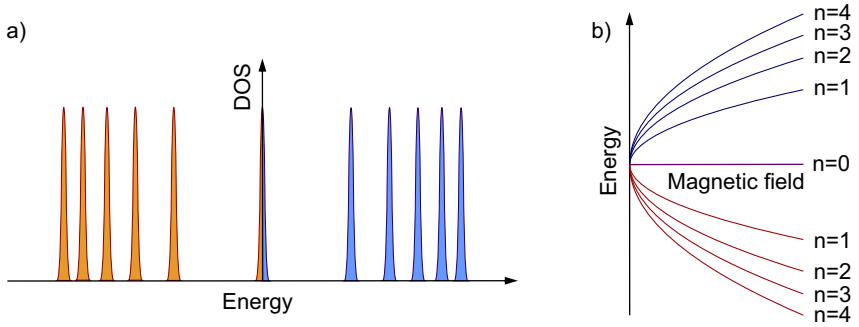

Figure 2.4: Representation of the relativistic Landau levels (LLs) of equation 2.25. The two graphics have to be compared with the classical LLs of figure 2.3. **(a)** Density of state (DOS) as a function of the energy E. The sharp peaks represent LLs. The red LLs represent LLs in the valence band and then filled by holes, whereas the blue LLs represent LLs of the conduction band filled by relativistic electrons (Dirac fermions) **(b)** Evolution of quantized energy levels as a function of the magnetic field. Each LL E_n is labelled by its value of n in the valence and the conduction bands

2.2.4 Quantization of the conductance

The appearance of LLs leads to a quantized Hall conductance. This is due to the quantum Hall effect, discovered by K.v.Klitzing, G.Dorda, and M.Pepper in 1980 [60]. Figure 2.5 represents a Hall bar used to measure the longitudinal resistance R_L and the Hall resistance R_H in the presence of a magnetic field, here along z; electrons are confined in the $x-y$ plane.

Ohm's law is expressed in its tonsorial form as $\mathbf{E} = \rho\mathbf{j}$ with ρ the resistivity tensor and reciprocally, $\mathbf{j} = \sigma\mathbf{E}$ with σ the conductance tensor. These two tensors have the following expressions

$$\rho = \begin{pmatrix} \rho_L & \rho_H \\ -\rho_H & \rho_L \end{pmatrix} \qquad \text{and} \qquad \sigma = \begin{pmatrix} \sigma_{xx} & \sigma_{xy} \\ \sigma_{yx} & \sigma_{yy} \end{pmatrix} \tag{2.26}$$

In expression 2.26, longitudinal resistivity and Hall resistivity have the form

$$\rho_L = \frac{m_e}{n_e e^2 \tau} \qquad \text{and} \qquad \rho_H = \frac{B_z}{e n_e} \tag{2.27}$$

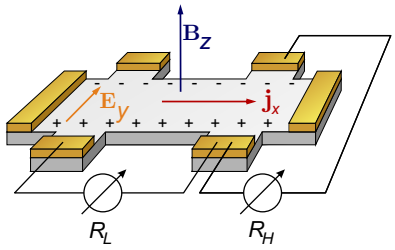

Figure 2.5: Representation of a Hall bar. This kind of device allows measurements of the longitudinal resistance R_L and Hall resistance R_H in the presence of a magnetic field.

where m_e is the electron mass, n_e the electronic density and τ the mean time between two scattering events. The resistivity tensor can also be expressed as the inverse of the conductivity tensor

$$\rho_L = \frac{\sigma_{xx}}{\sigma_{xx}^2 + \sigma_{xy}^2} \qquad \text{and} \qquad \rho_H = \frac{\sigma_{xy}}{\sigma_{xx}^2 + \sigma_{xy}^2} \tag{2.28}$$

If the Fermi level E_F stands in an LL[1] as shown in figure 2.6a, the entire Hall bar can conduct electricity, leading to a finite resistivity $\rho_L \neq 0$. However, if E_F stands outside an LL, as shown in figure 2.6b, only the edges of the Hall bar will contribute to the current [61-63]. In this case, the current flows without dissipation and resistivity drops to zero. Equation 2.28 implies that the conductivity term σ_{xx} is also zero for finite values of σ_{xy}. Hall resistivity is then expressed as $\rho_H = \sigma_{xy}^{-1}$.

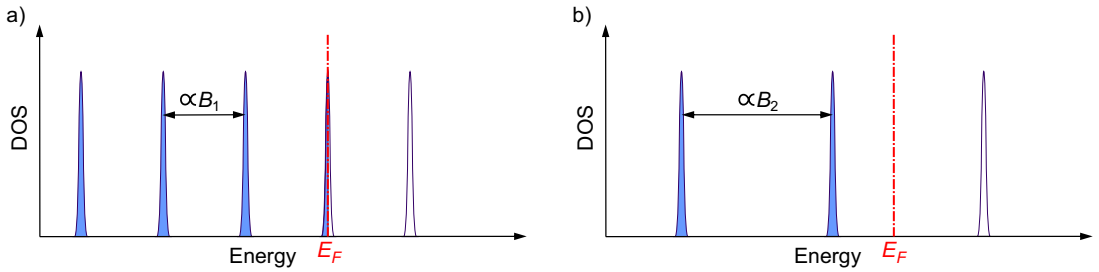

Figure 2.6: Effect of the increase of magnetic field ($B_1 < B_2$) on the LLs repartition. **(a)** For value B_1, the Fermi energy stands in an LL leading to a finite value for the longitudinal resistivity of the Hall bar of figure 2.5 **(b)** For value B_2, the Fermi energy is outside any LL. It leads to vanishing longitudinal resistivity of the Hall bar.

The last step is to determine Hall resistivity and conductivity where Fermi energy stands outside an LL (figure 2.6b). In this situation, each LL is totally filled by electrons. It can be demonstrated that each quantum state has a contribution of one magnetic flux quantum $\phi_0 = h/e$ [43, 60]. The number of quantum states is given by

$$N_B = \frac{\phi}{\phi_0} = \frac{B_z A}{h/e} \tag{2.29}$$

The density of N_B is expressed as $n_B = eB_z/h$. One can define what is known as the *filling factor* [43, 60, 64]

$$\nu \equiv \frac{n_e}{n_B} \tag{2.30}$$

This factor gives the number of completely filled LLs below the Fermi level. However, when the magnetic field is not strong enough to induce Zeeman splitting [65, 66], LLs corresponding to the two spin states are degenerated. Therefore, in the classical case, the filling factor can be given in terms of apparent LLs, n as [43]

$$\nu = 2n \tag{2.31}$$

In the relativistic case, LLs are degenerated because of the spin and also because of the two lattices. Furthermore, the central LL is located at $E = 0$ such as the upper part accounts for the electrons and the

[1] In this section, LLs are considered to be entirely formed by extended states. Localised states that do not contribute to the electronic transport are considered to be *outside* LLs. For further information, see [61, 62, 64]

lower part for the holes, as shown in figure 2.4a. The filling factor is then given in term of apparent LLs, n as [43]

$$\nu = 4(n + 1/2) \tag{2.32}$$

By replacing electron density n_e of equation 2.27, longitudinal resistivity is given in terms of the filling factor as

$$\rho_H = \frac{h}{\nu e^2} \tag{2.33}$$

The quantized resistivity of equation 2.33 is shown for both the classical and the relativistic cases in figure 2.7. Hall conductivity σ_{xy} is also quantized and forms plateaus at values proportional to the filling factor and the ratio e^2/h, called the quantum of conductance [60, 64]

$$\sigma_{xy} = \nu \frac{e^2}{h} \tag{2.34}$$

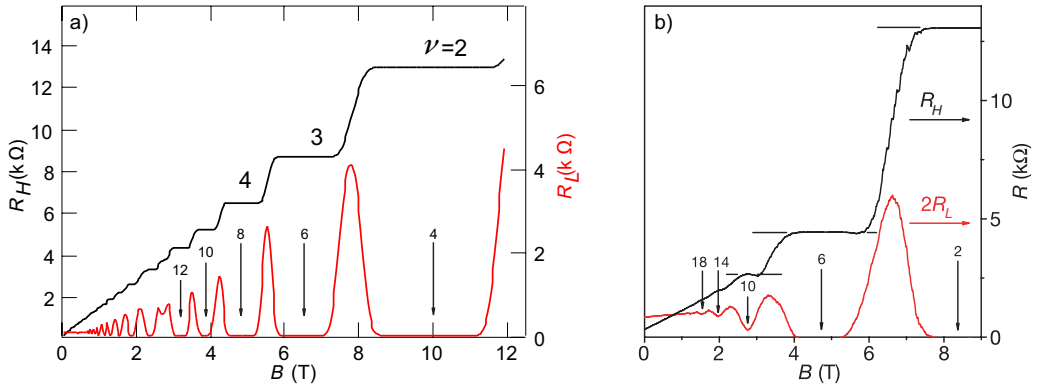

Figure 2.7: Experimental measurements of longitudinal (L) and Hall (H) resistivity: **(a)** for classical electrons in a GaAs-AlGaAs heterostructure at 0.3K, adapted from [67]. **(b)** for Dirac electrons in graphene at 30mK, adapted from [68].

chapter 3

Hofstadter's butterfly

As seen in chapter 2, the electronic energy of a crystal can be quantized in two ways by the lattice potential and by an applied magnetic field. In the two previous chapters, these two quantizations were treated independently. A natural question arises as to what happens when both effects are considered together. This chapter first presents theoretically the combined effect of both quantizations in a simple square lattice, as developed in the paper of Douglas Hofstadter [1]. Then, the case of graphene is discussed. Finally, experimental evidence of this double quantization is presented.

3.1 Hofstadter butterfly in a simple square lattice

In 1955, P.G. Harper wrote a paper [69] in which he develops the effects of the lattice potential and an external magnetic field on a two dimensional square lattice. This study led to what is now called *Harper's equation*, presented in section 3.1.1. However, Harper did not succeed in finding the solution of his equation for different values of the magnetic field.

In 1976, Douglas Hofstadter published a paper [1] in which he performs the calculation of Harper's equation. The combined effect of the potential and the magnetic field gives rise to a quantization of the energy that exhibits a fractal pattern. This section develops the basics of the calculation, the results and the interpretation of those results.

3.1.1 Harper's equation

This section will closely follow the derivation of Harper's equation developed by Hofstadter in [1]. As a starting point, a two dimensional square lattice is considered, as represented in figure 3.1.

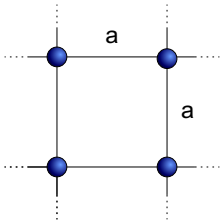

Figure 3.1: Schematic of a two dimensional square lattice. The unit cell has dimension $a \times a$.

The simplest way to describe the behaviour of an electron in this lattice is given by the tight-binding formalism of section 1.1. Only one orbital per site is considered. Energy dispersion, called the *Bloch band*,

is then given by

$$E(\mathbf{k}) = 2\gamma_0(\cos k_x a + \cos k_y a) \tag{3.1}$$

This expression is directly related to the following effective Hamiltonian (by substituting $\mathbf{k}$ by the impulsion operator $\hat{\mathbf{p}}$)

$$H = \gamma_0 \left[\exp\left(\frac{ia\hat{p}_x}{\hbar}\right) + \exp\left(\frac{-ia\hat{p}_x}{\hbar}\right) + \exp\left(\frac{ia\hat{p}_y}{\hbar}\right) + \exp\left(\frac{-ia\hat{p}_y}{\hbar}\right)\right] \tag{3.2}$$

As described in section 1.1.3, each exponential $\exp\left(\pm ia\hat{p}_{\{x,y\}}/\hbar\right) \equiv \hat{T}_{\{x,y\}}(\pm a)$ is a translation operator that expresses the periodicity of the lattice. The effect of the translational operators on a two-dimensional wave function is

$$\hat{T}_x(a)\psi(x,y) = \psi(x+a,y) \qquad \text{and} \qquad \hat{T}_y(a)\psi(x,y) = \psi(x,y+a) \tag{3.3}$$

The effect of an external magnetic field $\mathbf{B}$ is expressed by the Peierls substitution of equation 1.19. By considering a magnetic field perpendicular to the two-dimensional plane (along z), the Landau gauge can be used: $\mathbf{A} = (0, Bx, 0)$. The Peierls substitution and the Landau gauge are applied to the translational operator along y, it leads to

$$\exp\left(\frac{ia(\hat{p}_y + eA_y)}{\hbar}\right) = \exp\left(\frac{ia(\hat{p}_y + eBx)}{\hbar}\right) \equiv \exp\left(\frac{ieBax}{\hbar}\right)\hat{T}_y(a) \tag{3.4}$$

The relation 3.4 can be included in equation 3.2.

$$\gamma_0\left[\psi(x+a,y) + \psi(x-a,y) + e^{ieBax/\hbar}\psi(x,y+a) + e^{-ieBax/\hbar}\psi(x,y-a)\right] = E\psi(x,y) \tag{3.5}$$

This relation is coherent with the result of section 1.1.3 where it was shown that the presence of a magnetic field adds a phase to the hopping parameter γ_0.

A parameter that will turn out to be essential in this study can be defined as

$$\alpha \equiv \frac{a^2 B}{h/e} = \frac{\phi}{\phi_0} \tag{3.6}$$

This dimensionless parameter turns out to be the quotient between the flux ϕ through the unit cell area and the magnetic flux quantum $\phi_0 = h/e$. Furthermore, the presence of both lattice parameter a and magnetic field B are of central importance for following this work. Indeed, thanks to the expression of magnetic length l_B in equation 2.10, $\alpha = (a/l_B)^2/2\pi$. The value of α is directly given by the ratio between the lattice parameter a and magnetic length l_B.
As discussed in section 2.2.1, when the value a is much smaller than l_B, the influence of the lattice can be neglected and the Drude model can be used. It leads to the Landau quantization described in section 2.2.2.
However, if value a is comparable to l_B, the effect of the lattice cannot be neglected any more. The Drude model is not suited and both quantizations of the lattice and of the magnetic field enter into account.

In order to reveal a difference equation, the following substitutions are achieved

$$x \equiv ma \qquad y \equiv na \qquad \varepsilon \equiv E/\gamma_0 \tag{3.7}$$

Parameter ε describes the energies of the Bloch band and, by equation 3.1, is bounded from -4 to 4. The final step of the development is to express the wave function $\psi(x,y)$ as a product of a wave function along x (or m) and y (or n). By looking at equation 3.5, the y-component can be expressed as a simple harmonic. Then

$$\psi(ma,na) \equiv e^{i\kappa n}\chi(m) \tag{3.8}$$

Expression 3.5 can then be rewritten to give what is called Harper's equation

$$\chi(m+1) + \chi(m-1) + 2\cos(2\pi m\alpha - \kappa)\chi(m) = \varepsilon\chi(m) \tag{3.9}$$

3.1.2 Plotting the butterfly

This section presents the solution of Harper's equation 3.9, mainly based on Hofstadter's paper. The goal here is not to go deep into the mathematical description of the solution but essentially to draw out the important physical interpretations. The solution of Harper's equation is directly represented in a graph of energy as a function of the magnetic field (expressed throughout the parameter α). This is shown in figure 3.2.

The starting point to solving Harper's equation is to impose a periodicity of the wave function along x (and thus m) to ensure that it is bounded. A periodicity q is imposed along m. It implies that $\chi(m+q) = \chi(m)$. The cosine in Harper's equation 3.9 must also have the periodicity q. Therefore, there should exists an integer p that obeys the following equality,

$$2\pi\alpha(m+q) - \kappa = 2\pi\alpha m - \kappa + 2\pi p \tag{3.10}$$

Equation 3.10 leads to the following essential condition on α

$$\alpha = \frac{p}{q} \tag{3.11}$$

p and q both being integers, this relation imposes α to be a rational number. The first main result of Harper's equation concerns energy ε of the Bloch band. At each value α, only certain values of ε are solutions of the equation. It transpires that, for each value of q in α, the initial Bloch band is split into q energy bands, separated by a band gap.

An important point is the case (called pure case[1] in [1]) where $\alpha = p/q = 1/N$ with N an integer. As said previously, at each value of N there are corresponding N energy bands. These bands can be plotted in a graphic, as shown in figure 3.2a. Two successive values of N form a cell (indexed by N) as shown by a black quadrilateral in figure 3.2b. These cells form the skeleton of the graph. When N becomes large (and α small), the cells shrink in size and converge towards thin energy bands. These energy bands are the Landau levels (LLs, see section 2.2.2), as highlighted by green lines in figure 3.2a.

The second main result of Harper's equation is that cells are at the basis of the recursive behaviour of the graph. As just discussed, energy bands at integer values of N form the skeleton of the graph. This skeleton is repeated recursively in each cell. This is illustrated by figure 3.2c. Each energy band included in the N^{th} cell is indexed by integer N_2, such as the associated value of α is given by[2] $1/(N + 1/N_2)$. The operation can be repeated indefinitely, such as each new cell created in cell N_n is indexed N_{n+1}. Each energy band of the skeleton is then located at a value of α expressed as

$$\alpha = \cfrac{1}{N + \cfrac{1}{N_2 + \cfrac{1}{N_3 + \cfrac{1}{\cdots}}}} \tag{3.12}$$

A last consideration concerns the meaning of integer p that has not yet been treated. As precised in [70, 71], integer p gives the number of subbands inside an LL described by cell N. In absence of any lattice potential, the LLs are not split in subbands. The integer p then accounts for the effect of the lattice potential. Based on the results of this section, two definitions will be necessary for further discussions.

[1] In [1], a *special case* is also discussed, altough it is not further elaborated here. Special case allows constuction of the central part of the graph of figure 3.2, near the value $\alpha = 1/2$

[2] The presence of N_2 gives a value of $p \neq 1$ in the expression of α. Indeed, if $\alpha = 1/(N + 1/N_2)$, the value of p is N_2 and the value of q is $NN_2 + 1$. The pure case $\alpha = 1/N$ is obtained when $N_2 \to \infty$. It corresponds to an infinite number of subbands in cell N, that is, to a continuous energy subband in cell N. This continuous band is one of the N subbands at position $\alpha = 1/N$ in the main skeleton. This is shown with the vertical colour lines in figure 3.2a.

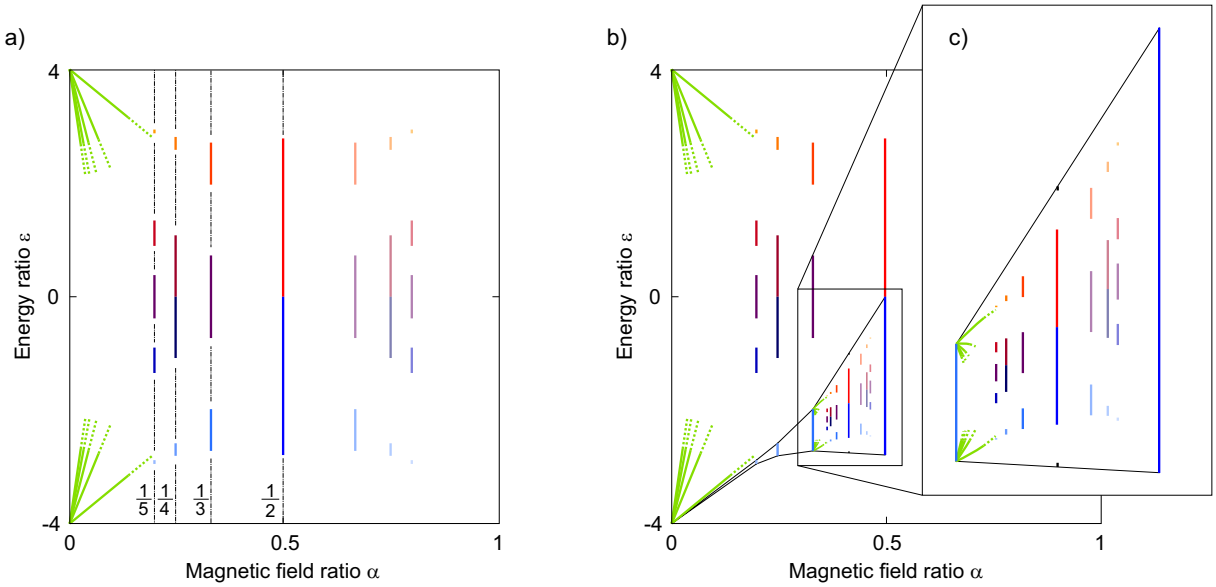

Figure 3.2: Construction of Hofstadter's butterfly. The horizontal axis is energy ratio $\varepsilon = E/\gamma_0$ and the vertical axis is magnetic field ratio $\alpha = a^2B/(h/e) = p/q$. Figure based on [1]. **(a)** The coloured vertical bands represent the energy bands corresponding to $p/q = 1/N$, with integer values of N from 2 to 5. The symetrical graph is shown for the corresponding values $1 - 1/N$ in the right part. The central band for even values of N touch at $\varepsilon = 0$. The green lines represent Landau levels at low magnetic field. **(b)** Two successive integer values N form a cell as shown with black quadrilaterals. The graph construction is recursive, such as the energy bands traced in a) are arranged in the same way in a cell. **(c)** Detail of the cell drawn in b).

The main energy bands

The main energy bands are basically Landau levels. At low values of α, LLs are formed by sharp energy bands. When α increases, LLs acquire an internal structure. They are formed by the cells shown in figure 3.2b. The number of main bands at a given value of α is indicated by the label N of the cell above α.

The subbands

The subbands constitute the internal structure of a main band. They are located inside a cell, as shown in figure 3.2c. At a given value of $\alpha = p/q$, there are p subbands in the each cell (and therefore in each main band). The total number of subbands along all the height of the diagram is given by q.

All previous discussions allow plotting of the final graphic of energy as a function of the magnetic field, as shown in figure 3.3, directly borrowed from [1].

3.1.3 Wannier diagram

Looking at the construction of Hofstadter's butterfly made in the previous section, it is apparent that energy levels are not defined for all the values of the magnetic field. Indeed, the allowed values of α can only take rational values p/q. By using equations 3.11 and 3.6, the values of the magnetic field where energy levels are defined are proportional to the same rational value p/q

$$B = \frac{h}{ea^2}\frac{p}{q} \tag{3.13}$$

This section presents what happens for irrational values of α. Hofstadter, in his paper of 1976, proposes an argument to explain the behaviour of his butterfly at irrational values of the field [1]. He argues that, at irrational field, energy levels are located continuously between two finite gaps (the gaps are described by the rational structure of the butterfly). This argument leads to a continuous behaviour of the butterfly, between two successive rational values of the field. However, Hofstadter does not give a formal proof of his argument.

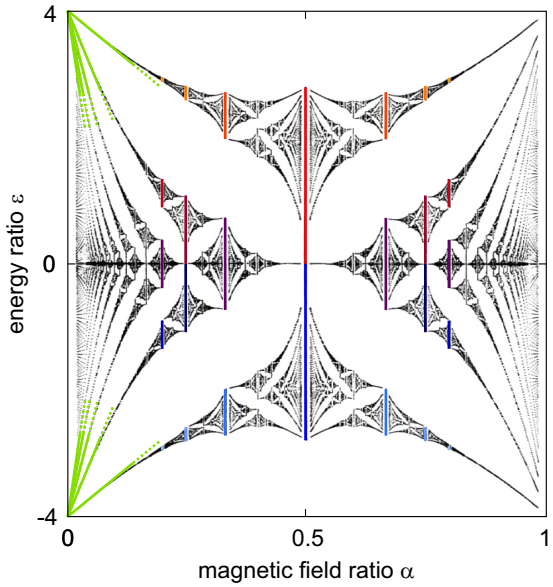

Figure 3.3: Hofstadter's butterfly as represented for the first time in [1]. The horizontal axis is energy ratio $\varepsilon = E/\gamma_0$ and the vertical axis is magnetic field ratio $\alpha = a^2B/(h/e) = p/q$. The graph represents all values for $q < 50$. Adapted from [1].

In 1978, Wannier introduces an interpretation of Hofstadter's butterfly independent of rationality [70]. Instead of considering energy levels as a function of the magnetic field, he considers the integrated density of state to construct what is now known as the Wannier diagram. In Hofstadter's butterfly of figure 3.3, the black regions correspond to the presence of energy levels. Density of state (DOS) in the black regions is therefore different from zero, $\rho(\varepsilon) \neq 0$. In the same way, the gaps correspond to values where DOS is zero, $\rho(\varepsilon) = 0$. Integrated DOS used by Wannier is thus defined as

$$n(\varepsilon_1, \varepsilon_2) \equiv \int_{\varepsilon_1}^{\varepsilon_2} \rho(\varepsilon) \mathrm{d}\varepsilon \tag{3.14}$$

By integrating over the whole tight-binding band (from $\varepsilon_1 = -4$ to $\varepsilon_2 = 4$), integrated DOS corresponds to the number of states of the completely filled tight-bind band n_0. Using these definitions, Wannier proposes to associate a statistical weight w to each energy band. A band is defined as the set of energy levels located between to successive gaps (here denoted by gap 1 and gap 2) such as weight w is defined as

$$w \equiv \frac{1}{n_0} \int_{\varepsilon_1 \in \text{ gap } 1}^{\varepsilon_2 \in \text{ gap } 2} \rho(\varepsilon) \mathrm{d}\varepsilon \tag{3.15}$$

This definition has an important implication. As outlined in [70], each band must have the same weight. As represented in figure 3.2, the main energy bands correspond to values $\alpha = 1/N$. It was shown in the previous section that there are N bands for each value of $\alpha = 1/N$. Using Wannier's argument, each band must then have a weight $1/N$.

As a last definition, total integrated DOS n is taken between the lower point of the band (here -4) and Fermi energy ε_F. The corresponding total weight is defined as:

$$W = \frac{n}{n_0} \tag{3.16}$$

As explained at the end of the previous section, for general value $\alpha = p/q$, energy is split into q subbands. Each subband has a weight of $1/q$. Subbands cluster together, by group of p, to form main bands. The total weight of each main band is, by consequence, $p/q = \alpha$. The total weight of one main band then evolves $W = \alpha$, for two main bands as $W = 2\alpha$, and so on. It corresponds to straight lines in a graph of total weight W as a function of α. This is shown in red in figure 3.4. Due to the symmetry of Hofstadter's butterfly along the energy axis, the total weight is given by $W = 1 - \alpha$ when one upper band is removed, $W = 1 - 2\alpha$ when two bands are removed, and so on. This is shown in blue in figure 3.4. This reasoning is essential as it gives a continuous description for all the values of the magnetic field, no matter if it is rational or irrational.

A general description, taking into account the subbands, can be obtained using a recursive reasoning. This is detailed in [70] and the general result is that the total weight (or integrated DOS) can be given by all the straight lines of the form

$$W = s + t\alpha \qquad\qquad s, t \in \mathbb{Z} \tag{3.17}$$

The case $s = 0$ or $s = 1$ has still been treated and correspond to the main bands. In that case, the coefficient t gives the number N of main band. The higher values of s account for the subband. It describes the substructure of Hofstadter's butterfly. An example for higher values of s is given in figure 3.4 with two green lines.

Equation 3.17 is a Diophantine equation. Using definitions 3.6 and 3.16 gives

$$\frac{n}{n_0} = t\frac{\phi}{\phi_0} + s \tag{3.18}$$

When s is set to 0, a parallel can be made immediately with the Landau quantization and equation 2.29 in section 2.2.4. Coefficient t is indeed the filling factor of equation 2.30 and gives the effect of the magnetic quantization. Parameter s corresponds to the Bloch band filling factor brought by the periodicity of the crystal [72, 3].

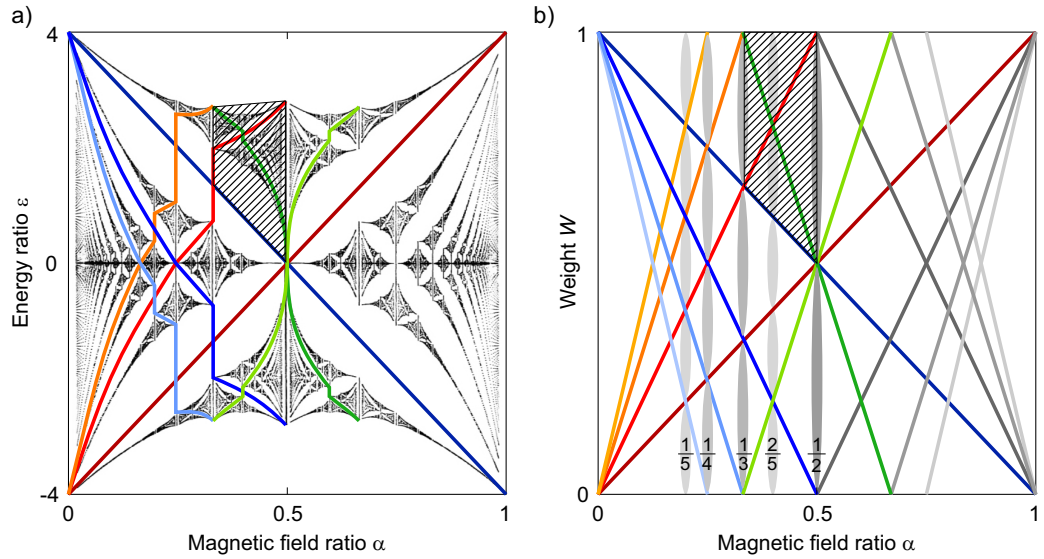

Figure 3.4: Construction of the Wannier diagram based on Hofstadter's butterfly. **(a)** Hofstadter butterfly as represented in figure 3.3. The colour lines stand in the gaps between two main bands (LLs for $\varepsilon < 1/2$). **(b)** Representation of the Wannier diagram for $t \leqslant 4$. The total weight (integrated DOS) at a certain value of α is given by the value of the straight lines (here in colour). The correspondence of these lines is shown in a). The two green lines give an example of the total weight obtained by considering the structure of the subcells and subbands. The grey ellipses represent the equal weights of each band. When a band is located at α, the weight of a band is α. The case $\alpha = 2/5$ gives an example of the structure inside a cell. Finally, the hatched zones represent a cell in Hofstadter's butterfly, as described in 3.2 and its correspondence in the Wannier diagram

3.1.4 Study of the conductance

As detailed in section 2.2.4, the Hall conductance in the presence of a magnetic field is quantized as a function of the number of Landau levels (LLs) located below the Fermi level. The value of the conductance remains constant when the Fermi level stands inside a gap. A generalisation of this quantization can be made for all two-dimensional systems in presence of a magnetic field. Due to gauge invariance, conductance is quantized as integer multiples of e^2/h and only changes when the Fermi level shifts from one gap to another [73]. In the case of the butterfly, LLs are split in sub-levels at high value of the magnetic field. This section describes the behaviour of the conductance in the substructure of LLs.

By assuming Landau quantization for a free electrons gas, the expression of conductance found in equation 2.34 is $\sigma_{xy} = \nu e^2/h$. This is well represented at low values of α in figure 3.6. Each colour corresponds to a value of conductance (integer number of conductance quanta) that remains constant in the same energy gap. When Fermi levels stand in the lower part of the graph ($\varepsilon_F < 0$ represented by the red zone in figure 3.5a), conductance increases by steps as the Fermi energy increases on the energy axis.

When Fermi energy is located in the upper half of the Bloch band, another formalism is needed. The Bloch band is first considered as totally filled. Then, all electrons above the Fermi energy are removed. These missing electrons are called *holes* and are located between the Fermi level and the upper part of the band, as represented in blue in figure 3.5b. They carry a charge $+e$. The situation here is perfectly symmetric with what is discussed previously for electrons. However, conductance is negative for holes, and its value decreases when the Fermi level goes down from the top of the Bloch band.

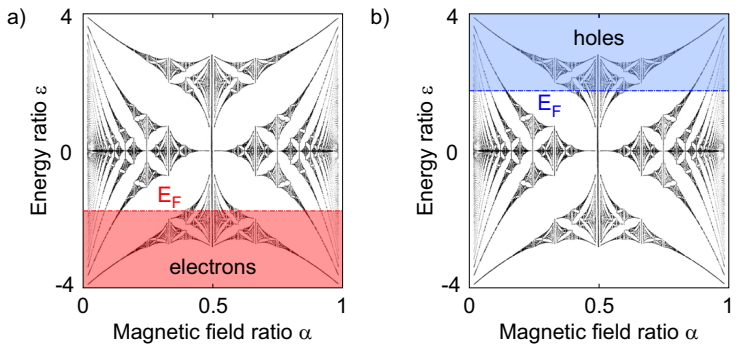

Figure 3.5: Representation of the Fermi level in Hofstadter's butterfly. **(a)** the Fermi level is in the lower half part of the graph (along the energy axis). The Bloch band is filled with electrons. **(b)** The Fermi level stands in the upper half of the graph. The Bloch band can be seen as filled with holes, represented by the light blue area.

Due to the recursive behaviour of the graph, changes of the conductance in the sub-levels of the graph is also observed. The values of the conductance inside the gaps of the sub-structure have been investigated by Thouless et al. [71]. They use the Kubo formula [74] to make the link between the Hall conductance σ_{xy} and the wave function $\chi(m)$ in Harper's equation 3.9. In their development, they label by r the rth gap at a given value of $\alpha = p/q$. As explained in section 3.1.2, there are q subbands at $\alpha = p/q$. There are thus $q-1$ gaps. Each subband is associated to a gap[3] and carries a density $w = 1/q$ (given by equation 3.15). It is then possible to relate the label r of the gap to the total density n of the bands below the gap: $r = q\, n/n_0$. By using equation 3.18, it leads to

$$r = t_r p + s_r q \tag{3.19}$$

By specifying a value of r for a given value of α, the integer factors s_r and t_r can be found by taking t_r between $-1/2q$ and $1/2q$, as precised in [71]. An example for $\alpha = 4/13$ is given below.

The knowledge of integer t_r allows conductance to be determined. Indeed, conductance is given by $\sigma_{xy} = t_r e^2/h$ in the case of a tight-binding as given in [71]. Figure 3.6 shows the corresponding Hofstadter butterfly where the gaps are coloured as a function of conductance in the gap.

Example for $\alpha = 4/13$

In this example, $q = 13$, thus $-6 < t < 6$, and the equation 3.19 becomes

$$r = 4t + 11s$$

The allowed values for t and their corresponding values of $pt = 4t$ are presented in table 3.1.
And the four first values of s and the corresponding $qs = 13s$ are given in table 3.2.

Each value of r, going from $q = 1$ to $q - 1 = 12$, corresponds to only one couple of values of s and t given in the table 3.3

[3] If q is even, the central gap is shared both by the upper ($\varepsilon > 0$) and the lower band ($\varepsilon < 0$). If q is odd, the central band is associated to the two adjacent gaps.

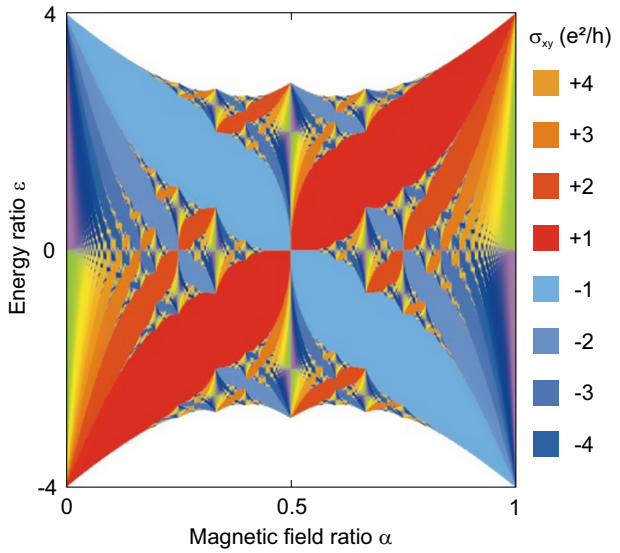

Figure 3.6: Schematic of the coloured butterfly. The colours represent the integer factors t of Hall conductance $\sigma_{xy} = te^2/h$ as labelled with the coloured bar on the right. Adopted from [75]

$\|t\|$	1	2	3	4	5	6
$4t$	±4	±8	±12	±16	±20	±24

Table 3.1: Allowed values of t.

$\|s\|$	0	1	2	3
$13s$	0	±13	±26	±39

Table 3.2: Four first values of s.

r	1	2	3	4	5	6	7	8	9	10	11	12
$t = \sigma_{xy}\, h/e^2$	-3	-6	4	1	-2	-5	5	2	-1	-4	6	3
s	1	2	-1	0	1	2	-1	0	1	2	-1	0

Table 3.3: Couples of values for t and s for each gap labelled by r. The values of $t = \pm1$ are highlighted in blue. They always appear at positions $r = p$ and $r = q - p$.

Interesting observations can be extracted from table 3.3. First is the presence of the values $t = \pm1$ at $r = p$ and $r = q - p$. This is due to each band being divided into p subbands. The case $r = p$ automatically considers the first gap associated to the first Landau level. This gap is given by the straight line $\varepsilon = \alpha$ in the Wannier diagram in figure 3.4. The second observation is the symmetry of the table; the value t_r is equal to $-t_{q-r}$. This is due, of course, to the symmetry of the butterfly. The minus sign is from the upper part of the butterfly which gives a holes current, leading to a conductance of opposite sign, as developed at the beginning of the section and in figure 3.5. All these observations are synthesized in the Wannier diagram in figure 3.7. Only the straight lines corresponding to table 3.3 were drawn, highlighting clearly the band and subbands of this case.

3.2 Hofstadter's butterfly in graphene

The case of a simple square lattice discussed in section 3.1 is quite unrealistic. One can wonder if the fractal-like energy spectrum also arises in more realistic structures. A good candidate to take on this role is graphene. Indeed, it is a two-dimensional structure, as was the simple square lattice. Furthermore, it only contains two atoms in the unit cell and its geometrical structure is quite simple. In the first section

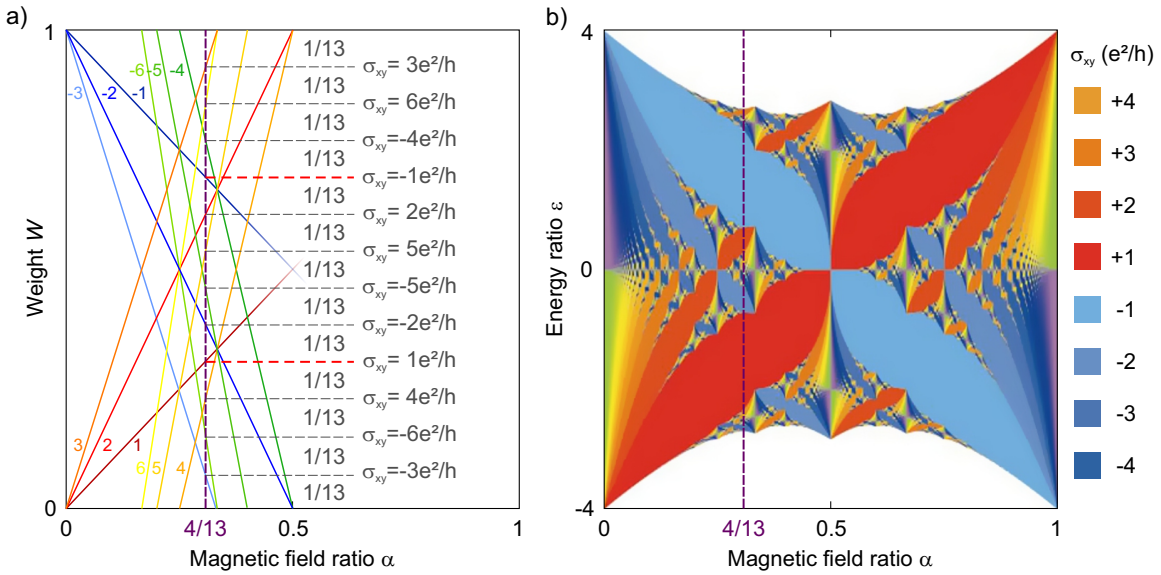

Figure 3.7: Wannier diagram constructed for the case $\alpha = 4/13$ as developed in the example above and its correspondence on Hofstadter's butterfly. **(a)** The straight lines are of the form $w = t\alpha + s$ with the couples of coefficients t and s given in table 3.3. Each straight line represents a gap and crosses the vertical purple line $\alpha = 4/13$ at a value of $r/13$ on the energy axis, with r the label of the gap corresponding to each couple t, s in table 3.3. The intersection of a line of slope t and the vertical line $\alpha = 4/13$ gives the value of the Hall conductance te^2/h in the rth gap. The values of the slopes t of the lines are given next to the lines. Red lines correspond to $s = 0$, blue to $s = 1$, yellow to $s = -1$ and green to $s = 2$. This schematic also highlights the presence of three Landau levels, shown by dotted red lines, and four subbands in each Landau level. **(b)** coloured Hofstadter butterfly. The color in each gap corresponds to the value given in the Wannier diagram a).

below, the Wannier diagram for graphene is constructed, and in the second section, Hofstadter's butterfly is presented.

3.2.1 Wannier diagram for graphene

As discussed in section 1.2.2, there are two bands that contribute to conduction. They join together at the Fermi level, at K-points. The first, located in the negative energies, is the valence band. The second, located in the positive energies, is the conduction band. To construct the Wannier diagram, these two bands must be taken into account. Because the two bands touch at the Fermi level without crossing, the Wannier diagram is simply given by two superposed diagrams, each of them similar to figure 3.4b. This is shown in figure 3.8.

3.2.2 Hofstadter's butterfly for relativistic Landau levels

In section 2.2.3, the LLs in graphene were found to follow a square root dependence on the magnetic field. This major difference compared with the linear dependence of the classical LLs will logically affect the butterfly of graphene. In the limits of a small magnetic field, it is expected to obtain this square-root dependence around the energy 0 (where are located the K points). Hofstadter's butterfly for graphene is shown in figure 3.9. The LLs at low magnetic field are indicated with green lines. The central LLs have the characteristic square-root behaviour predicted in graphene whereas the upper and lower LLs are linear. This is due to the fact that electrons far from the energy 0 are no more Dirac fermions. As shown in figure 3.8b, the energy dispersion at the top of conduction band and at the bottom of valence band is not linear with the wave vector anymore.

The graph of figure 3.9 is obtained by calculating the DOS in a supercell made of 10×10 unit cells of graphene at different values of magnetic field B. The values used to obtain the different DOS are determined by setting a integer number N of magnetic flux quanta $\phi_0 = h/e$. That is, $B = N\phi_0/(nA)$, where A is the are of a unit cell of graphene and n is the number of unit cells in the supercell (here 100) such that nA is the area of the supercell. As discussed in section 3.1.2, the butterfly is ploted for values of

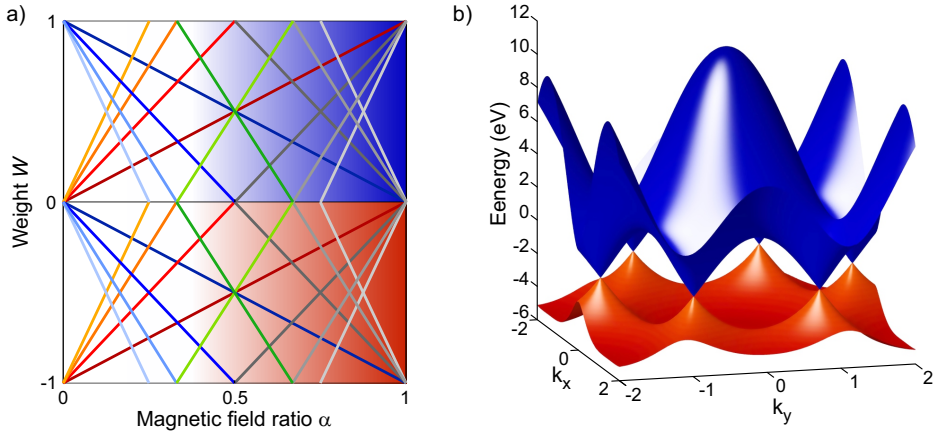

Figure 3.8: Construction of the Wannier diagram (WD) for graphene. **(a)** In graphene, the valence and conduction bands touch at the Fermi level. A WD as constructed in figure 3.4 can be associated to each band. The total diagram is then given by a superposition of two classical WDs. The red part corresponds to the valence band and the blue part to the conduction band. **(b)** Band structure of graphene, similar to the one of figure 1.3. The valence band is in red, the conduction band in blue.

the parameter α between 0 and 1. This is achived by imposing $N \leq n$. Hofstadter's butterfly of figure 3.9 is therefore computed for 100 successive values of B.

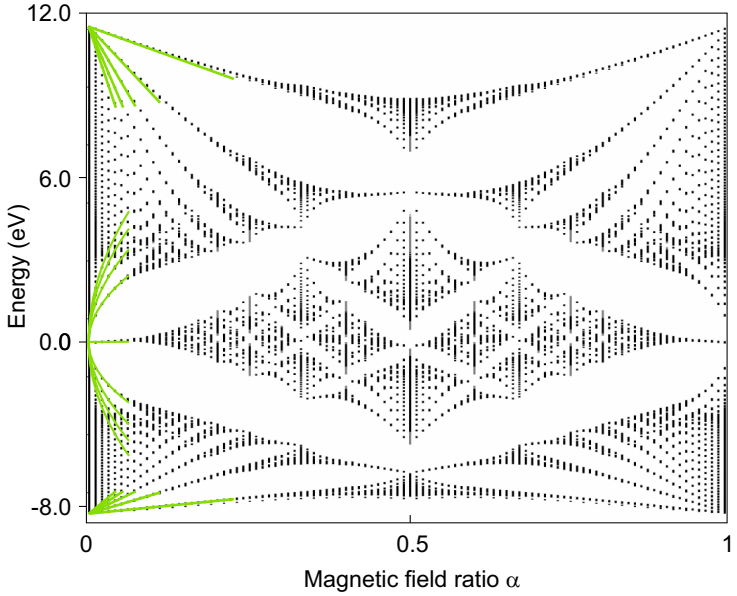

Figure 3.9: Hofstadter's butterfly in graphene related to the Wannier diagram of figure 3.8a. The butterfly has been computed in a superlattice of 10×10 unit cells of free graphene by considering the first and second nearest neighbours. The hopping parameters are $\gamma_n = 2.8$ eV and $\gamma_{nn} = 0.28$ eV. Each vertical line represents the DOS at a given magnetic field (white if lower than 5% of the maximum of the DOS and black if higher than 5%). The green lines indicate the position of the LLs.

3.3 Observation of Hofstadter's butterfly

This section presents and discusses the experimental evidences that have confirmed the existence of Hofstadter's butterfly. As explained in the first section below, it is necessary to build a supercell to observe the butterfly. The two last sections present the signature of the butterfly in such supercells, highlighted in two concomitant papers [3, 19].

3.3.1 The moiré pattern

As discussed in section 3.1.1, the observation of Hofstadter's butterfly depends on two characteristic lengths. The first is a, the lattice parameter, and the second is l_B the magnetic length. The fractal behaviour of energy spectrum appears when l_B becomes comparable to a; in other words, when the coefficient $\alpha = (a/l_B)^2$ is such that $\alpha \sim 1$. From the definition of the magnetic length of relation 2.10, it leads to a condition on the magnetic field as a function of the lattice parameter a. That is,

$$B_z \sim \frac{\hbar}{ea^2} \tag{3.20}$$

By taking a typical value of the lattice parameter, the one of graphene for example, it gives $a = 2,46$ Å. The magnetic field needed to observe Hofstadter's butterfly should have a value of the order of 10 000 T! This value is by far beyond the reachable magnetic field available in laboratories. Nevertheless, if it is not possible to play on magnetic field, the idea is to play on the lattice parameter. This path was still discussed by D. Hofstadter at the end of its paper [1]. Figure 3.10 gives the evolution of magnetic field needed to reach $\alpha \sim 1$ as a function of the lattice parameter a.

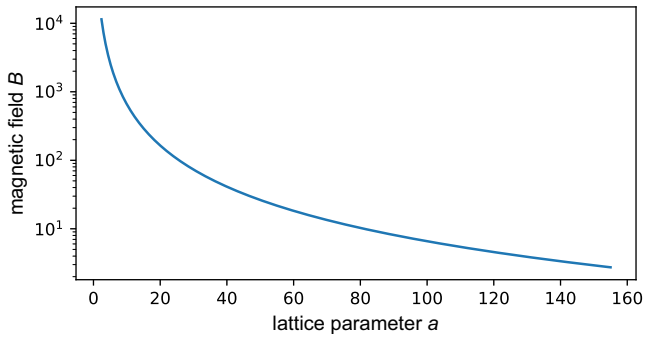

Figure 3.10: Evolution of magnetic field B_z as a function of the lattice parameter a in order to have $\alpha \sim 1$

Many experimental studies highlighted the fractal-like behaviour of Hofstadter's butterfly in GaAs-AlGaAs [4-6]. The arrival of graphene in 2004 has opened a new way to observe the butterfly. In order to increase the mobility of charge carriers in graphene, hexagonal-boron-nitride (hBN) is used as a substrate for graphene [12-14]. hBN, whose structure is described in section 1.3.2, is isomorphic to graphene but has a lattice parameter slightly different from that of graphene. When placed on hBN, graphene is extremely flat compared with other substrates and exhibits a moiré pattern, due to the lattice mismatch, as highlighted in figure 3.11. This moiré pattern breaks the initial translational symmetry of graphene and leads to a periodicity much more higher, given by a large supercell represented in figure 3.11a.

The moiré pattern has been highlighted by using scanning tunnelling microscope (STM) topography [16, 17, 18]. The results of figure 3.11 show clearly the effect of the hBN substrate on the graphene structure, giving rise to a moiré pattern (figure 3.12a). The Fourier transform of the STM image also highlights the presence of a superstructure. Around the points that give the periodicity (spacial frequency) of the graphene lattice in reciprocal space, extra points correspond to the spacial frequency of the moiré lattice [76]. The spacial frequency of the superstructure is of course much smaller than the one of graphene. This is shown in figure 3.12b. This properties can be related to the construction of the Brillouin zone (BZ) of the moiré lattice from BZs of graphene and hBN as shown in figure 3.12c.

As discussed previously, graphene placed on an hBN substrate leads to a visible moiré pattern. But the effects of hBN on the electronic properties of graphene remains to be discussed. This can be achieved by measuring the local density of state (LDOS) of graphene. The LDOS of an isolated graphene layer has a perfect V shape, in the same way as the DOS presented in figure 1.4b. By adding hBN, some *dips* arise at given energies, as shown in figure 3.13a. The dips appear at symmetrical positions on the energy axis but the dip corresponding to hole (negative energy) is much more pronounced. The energy at which dips appear depends on the wavelength of the moiré lattice (given by $\mathbf{L}_1$ and $\mathbf{L}_2$ in figure 3.11a). The

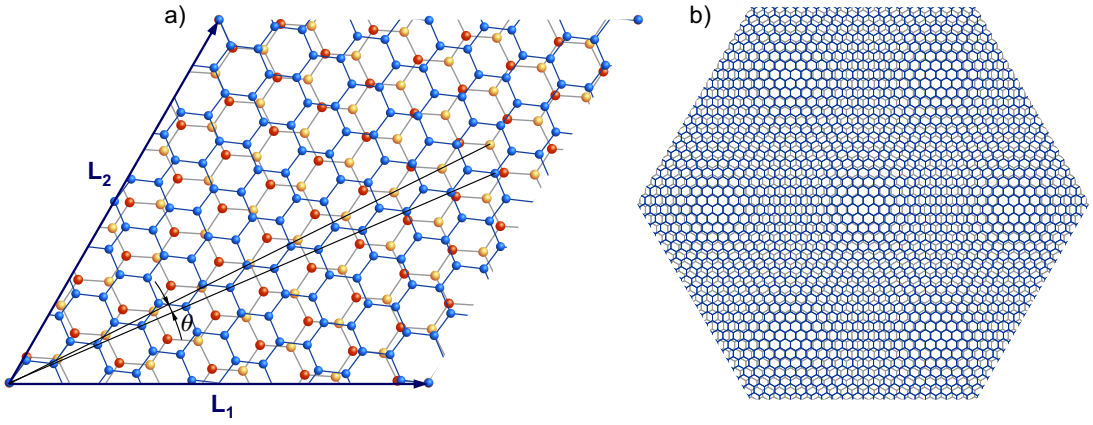

Figure 3.11: Formation of a moiré pattern when placing graphene on top of hBN. **a)** representation of the supercell of the moiré lattice. The lattices of graphene and hBN are rotated with angle θ with respect to each other. The lattice vectors of the supercell are given by $\mathbf{L}_1$ and $\mathbf{L}_2$. **(b)** view of the moiré lattice for angle $\theta = 0$.

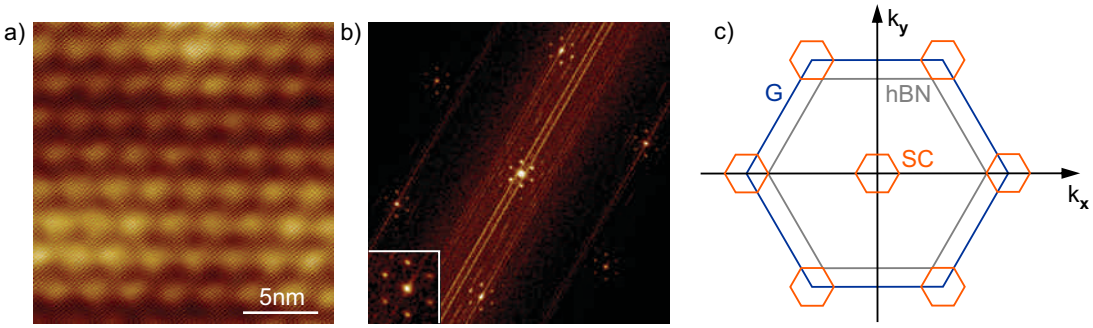

Figure 3.12: STM measurements of a graphene layer placed on top of hBN. Figures a) and b) are adapted from [17] and figure c) is inspired from [22] **a)** STM topography image of the moiré pattern. The light zone shows the borders of the superstructure. **(b)** Fourier transform of figure a). The external dots correspond to the *graphene lattice points*. Each of these points is surrounded by moiré lattice points, as highlighted in the inset. **(c)** Representation of the Brillouin zone of graphene (blue), of hBN (grey) and of the supercell (orange). This schematic corresponds perfectly to the results found in figure c).

conclusion is that hBN acts as a weak periodic potential [3, 16, 19], in the same way as the simple potential presented in section 2.1.2. This implies the creation of new Dirac cones at the corners of the superlattice BZ of figure 3.12c [16, 19]. It is predicted theoretically [77, 78] and is discussed in more detail in section 5.2.

The observation of a moiré pattern has been confirmed. The moiré pattern leads to the formation of a supercell, as described in figure 3.11a. This is the key to observing Hofstadter's butterfly. Indeed, the lattice parameter has to be increased to highlight the butterfly at reachable magnetic field, as represented in figure 3.10. This is exactly what happens in the moiré lattice.

3.3.2 Bilayer graphene on hBN

In 2013, the butterfly was experimentally observed for the first time in graphene by two groups simultaneously [3, 19]. In this section, the observation of the fractal-like energy spectrum by P. Kim's group is presented [3]. The experiment was performed on a Hall bar (see figure 3.14a) made of Bernal-stacked bilayer graphene (BLG) placed on an hBN substrate. A moiré pattern was observed between the BLG and the hBN layers. Figure 3.14 shows the evolution of longitudinal and Hall resistance (R_{xx} and R_{xy} respectively) as a function of the gate voltage V_g. The gate voltage modifies the position of the Fermi level, and the resistance depends on the LDOS (shown in figure 3.13a). It explains the presence of the two *satellite* peaks in R_{xx}, coherent with the dips of figure 3.13a. It indicates the presence of secondary Dirac points.

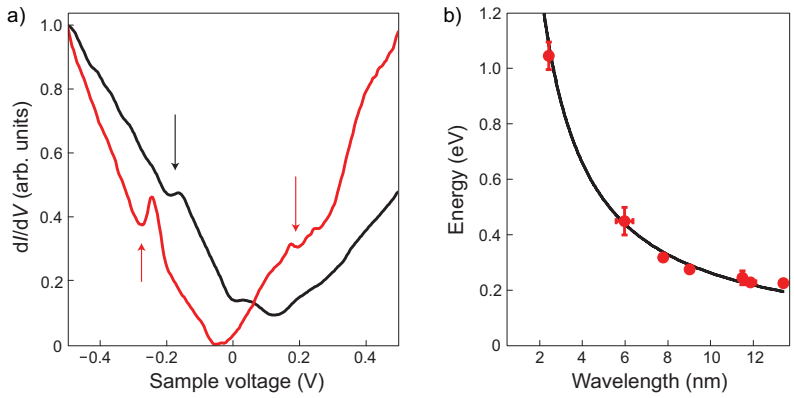

Figure 3.13: Signature of the effect of the hBN substrate on the electronic properties of graphene. **(a)** dI/dV curve for graphene on hBN exhibiting a moiré pattern with a period of 9.0 nm (black curve) and 13.4 nm (red curve). dI/dV is proportional to the LDOS. Dips in the valence and conduction bands are marked with arrows. **(b)** Evolution of the position of the dips on the energy axis as a function of the wavelength of the moiré pattern. Adapted from [16]

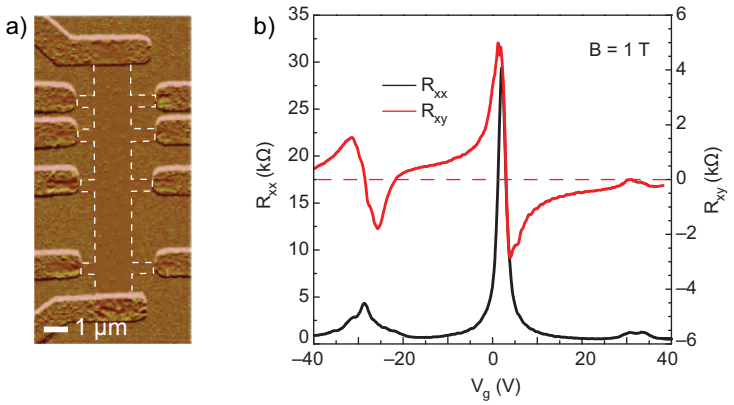

Figure 3.14: Experimental device **(a)** Hall bar made of a BLG layer placed on an hBN substrate and exhibiting a moiré pattern. **(b)** Evolution of longitudinal resistance R_{xx} and Hall resistance R_{xy} as a function of the gate voltage V_g. The peaks are coherent with the dips of figure 3.13. Adapted from [3].

It is extremely difficult to have access directly to the energy levels of a material. The direct observation of the butterfly is therefore not currently possible. However, it is possible to measure easily the density of charge carriers, proportional to the gate voltage. And this density is precisely present in the Diophantine equation 3.18, which allowed construction of the Wannier diagram of figure 3.4. The observation of the butterfly will thus be indirect and will be achieved with the Wannier diagram. As discussed in section 3.1.4, position of gaps in the Wannier diagram modifies the conductance that only takes values which are multiple of the quantum of conductance e^2/h. The measurement of conductivity as a function of both the magnetic field and the gate voltage is normally sufficient to observe fractal-like behaviour. This measurement is shown in figure 3.15.

In figure 3.15a, the Landau levels (LLs) classically observed in graphene are marked with white straight lines. They are localized in the plateaus of conductivity (see figure 3.15c) as discussed in section 2.2.4. The correspondence of those LLs is shown with blue lines in the Wannier diagram of figure 3.15b. All those lines join at $n/n_0 = 0$ and correspond to $s = 0$ in the Diophantine equation 3.18

$$\frac{n}{n_0} = t\frac{\phi}{\phi_0} + s$$

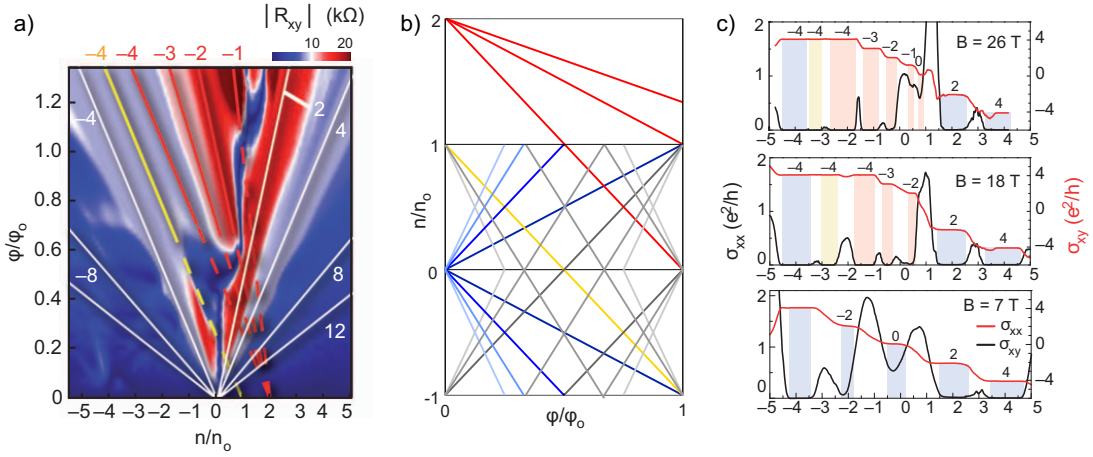

Figure 3.15: Observation of fractal-like behaviour in the conductivity of graphene placed on an hBN substrate and exhibiting a moiré pattern with a periodicity of 15.5 nm. **(a)** Hall conductivity map (also called *Landau fan diagram*) as a function of the density ratio n/n_0 and the magnetic flux ratio ϕ/ϕ_0. It is possible to trace straight lines by following the directions where conductivity is quantized in plateaus. White lines correspond to the Landau levels (LLs), and yellow and red lines to the substructure of Hofstadter's butterfly. **(b)** Wannier diagram for graphene. The correspondence with the lines of figure a) is made. Blue lines are given by $s = 0$ in the Diophantine equation and correspond to the LLs. The yellow line is given by $s = 1$ and red lines by $s = 2$. **(c)** Conductivity given as a function of the ratio n/n_0 for three values of the magnetic field. At 7 T, the evolution of conductivity is coherent with the quantum hall effect described in section 2.2.4. At 18 and 26 T, some extra plateaus appear at non-integer values of the filling fraction (coefficient t for $s = 0$ in the Diophantine equation). It corresponds to the lines of the substructure given by $s \neq 0$. Adapted from [3].

The proof of fractal-like behaviour is given by the presence of straight lines given by values of $s \neq 0$, shown in yellow and red in figure 3.15a. Indeed, they correspond to the presence of gaps in the substructure of the fractal-like pattern of the butterfly, as presented in figure 3.4. The corresponding lines are highlighted in the Wannier diagram in figure 3.15b.

The clear signature of the fractal-like substructure is also seen in the Hall conductivity of figure 3.15c. The conductivity forms plateaus quantized in integer multiples of e^2/h, but those plateaus are localized at non-integer LLs filling fractions (the value t when $s = 0$ in the Diophantine equation). In other words, their positions are given by straight lines that describe the substructure of the butterfly (with an integer slope t but with values of $s \neq 0$).

Figure 3.16b gives a clear view of the butterfly's fractal-like structure. Hall conductivity is shown at the top. It is quantized as integer multiples of e^2/h, but it does not just increase by steps with the gate voltage as it is the case for the sole Landau quantization. The conductivity presents a complex shape of quantized plateaus, as discussed in section 3.1.4.

The main feature of Hofstadter's butterfly is the periodicity of the substructure, leading to the fractal-like behaviour, as discussed in section 3.1.2. The butterfly is built with sub-cells inside which the butterfly structure is repeated recursively. This recursivity is highlighted in figure 3.17. Conductivity is given as a function of the magnetic field for a given value of density. The conductivity exhibits a clear periodic behaviour. A similar pattern is repeated for different values of the number of LLs below the Fermi level. The number of LLs below the Fermi level evolves with the magnetic field, as described in section 2.2.4.

3.3.3 Single graphene on hBN

In the previous section, the observation of the butterfly by P. Kim's group is described in a BLG layer. In the same volume of *Nature*, Novoselov and Geim's group also reported the observation of the butterfly [19]. The experiments were conducted with a single layer of graphene placed on a hBN substrate.

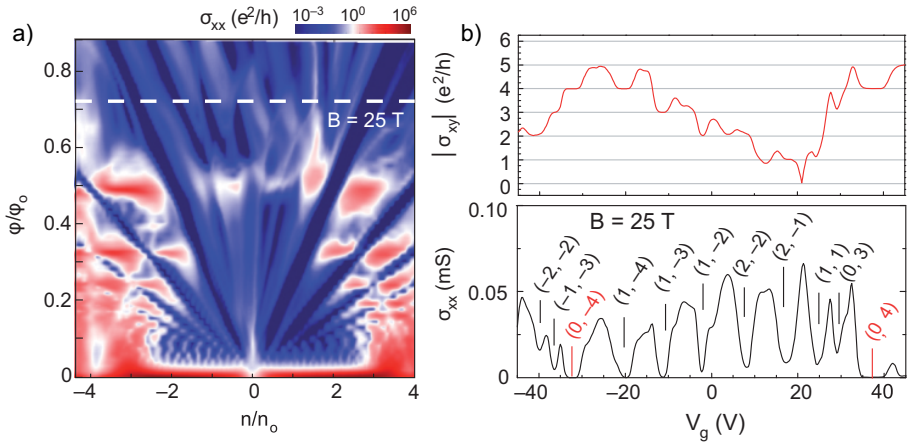

Figure 3.16: Description of graphene conductivity in a sample exhibiting a moiré periodicity of 11.6 nm. **(a)** Longitudinal conductivity map as a function of the density ratio n/n_0 and the magnetic flux ratio ϕ/ϕ_0. The effect of secondary Dirac points are visible for $n/n_0 = \pm 4$. **(b)** Hall conductivity (top) and longitudinal conductivity (bottom) at $B = 25$ T. Hall conductivity is quantized in integer multiples of e^2/h and its evolution is coherent with the substructure of the fractal-like energy spectrum. The labels in parentheses in the bottom figure give the couples (s, t) of the lines in the fan diagram, as explained in figure 3.15. Adapted from [3].

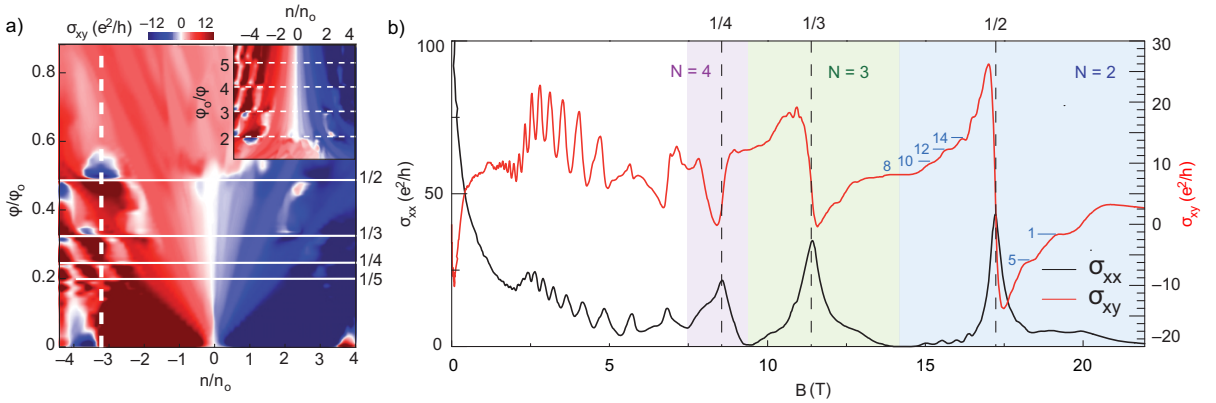

Figure 3.17: Recursive behaviour of conductivity. **(a)** Hall conductivity map of the device described in figure 3.16. The horizontal white lines indicate the values of $\phi/\phi_0 = 1/n$ with n an integer. This corresponds to the pure case introduced in section 3.1.2 where n was the label of the sub-cells. **(b)** Hall conductivity exhibits a periodic behaviour as a function of the magnetic field. A similar pattern is repeated at each values of n. The purple, green and blue zones give the number of LLs below the Fermi level. Adapted from [3].

Figure 3.18 reports the evolution of longitudinal and Hall resistivity as a function of the charge carrier density. This density is adjusted by applying a gate potential. In figure 3.18a, longitudinal resistivity exhibits tree peaks. The central peak corresponds to the main neutrality point (MNP), or Dirac point in graphene. The peaks situated at the left and right side of this MNP correspond to secondary neutrality points (SNPs), already described in section 3.3.1. An interesting feature is the height of the SNP in the hole side (valence band). At 10 K, it is three times taller than the MNP. In the electron side (conduction band), the SNP is less marked. This is coherent with the results reported in figures 3.13 and 3.14. In figure 3.18b, Hall resistivity is also modified, due to the presence of SNPs, at positions coherent with the longitudinal resistivity of figure 3.18a. The change of sign of Hall conductivity around the SNPs suggests the presence of electrons in the valence band and holes in the conduction band. The shape of the Hall resistivity suggests that energy dispersion around the SNPs is linear. This implies that the secondary neutrality points are in fact Dirac-points, as described theoretically in [77, 78].

Due to the moiré superlattice, the presence of fractal-like behaviour of the energy dispersion emerges. As discussed in the previous section, Hofstadter's butterfly is visible through the conductivity and the

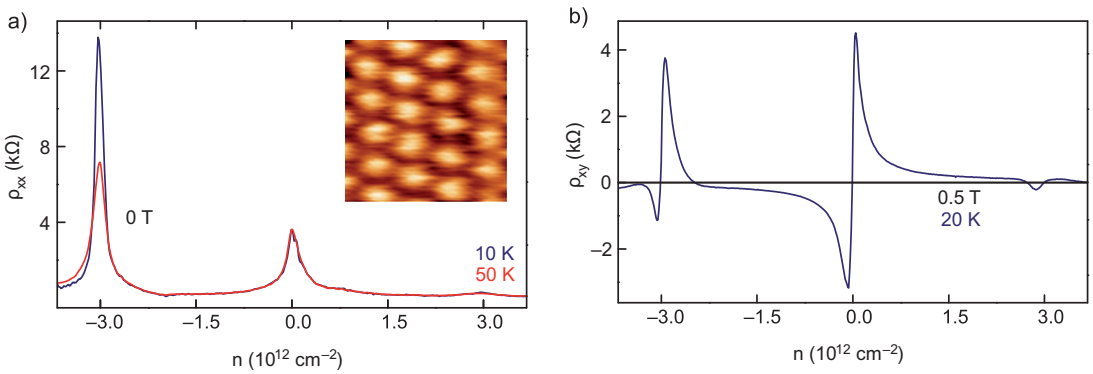

Figure 3.18: Longitudinal and Hall resistivity in the moiré lattice. **(a)** Longitudinal resistivity at 10 K (blue) and 50 K (red) as a function of the carrier density. The central peak corresponds to the main neutrality point (MNP) and the two peaks at the left and right sides correspond to the secondary neutrality points (SNPs). Inset, image of the moiré lattice obtained by a conductive atomic force microcope. The periodicity of the superlattice is around 11 nm. **(b)** Hall resistivity at 20 K under a magnetic field of 0.5 T. The MNP and the SNPs are also visible at the same positions as in figure a). The shape of resistivity around the SNPs suggest the presence of Dirac points at those positions. Adapted from [19].

resistivity when they are determined as a function of the density and the magnetic field. This is shown in figure 3.19.

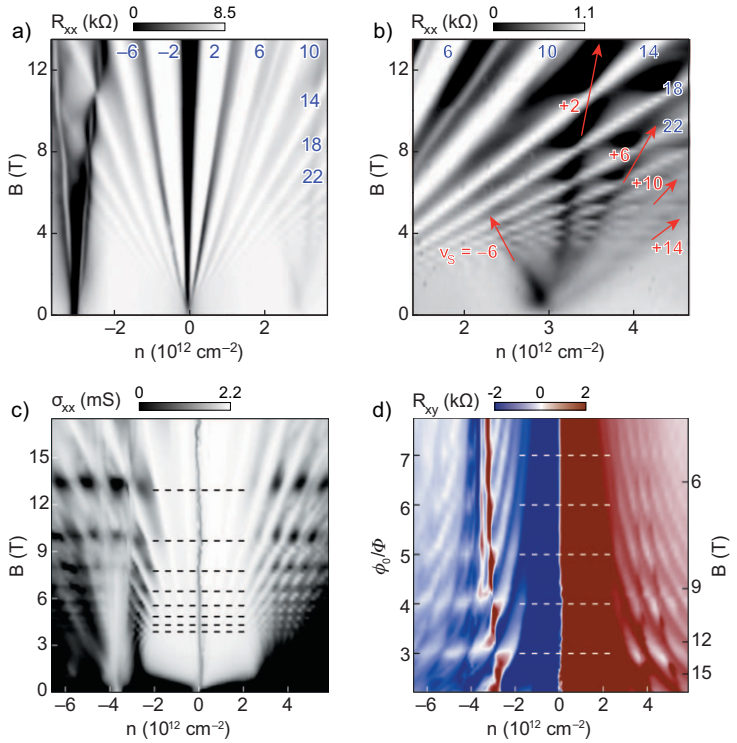

Figure 3.19: Observation of fractal-like behaviour in single graphene on hBN. **(a)** Longitudinal resistivity as a function of density and the magnetic field. The signature of the SNPs is visible at the left and right parts of the figure. Landau levels (LLs) are clearly visible and are labelled with blue numbers (each LL is 4 times degenerated as discussed in section 2.2.4). It is equivalent to figure 3.17a. **(b)** Zoom on figure a) around the right SNP. The red lines correspond to the Landau quantization around the left SNP. These lines corresponds to the straight lines in the Wannier diagram with $t = \nu_s$, the filling factor, and $s \neq 0$. **(c)** Longitudinal conductivity as a function of the magnetic field and density. The dashed lines indicate the value of B such that $\phi/\phi_0 = 1/q$. It is equivalent to figure 3.16a. **(d)** Hall resistivity as a fuction of density and the ratio ϕ_0/ϕ. The white lines correspond to $\phi_0/\phi = q$ $(\propto 1/B)$, that is, to the black lines of figure c). The Hall resistivity exhibits a recursive pattern as it discussed for conductivity in figure 3.17b. Adapted from [19].

chapter 4

The models

In section 3.3, the experimental observations of Hofstadter's butterfly are presented in a moiré pattern of graphene on hBN. This section develops the theoretical model used to obtain the butterfly in a similar system. First, the main hypotheses that are considered in this work are listed and justified. Then, the construction of the lattice and the inclusion of the magnetic field are detailed. Finally, two different models of the interaction between graphene and hBN close this chapter.

4.1 Initial hypotheses

Graphene on hBN is a complex system. The more accurate theoretical study of such a system would be achieved with DFT calculations. However, as discussed at the beginning of chapter 1, the number of atoms needed here is too large for DFT. This is due to the size of the supercell used to build the moiré lattice. Therefore, the choice of the simulation technique is the tight-binding model.

Nevertheless, the drawback of the tight-binding model is the wide range of free parameters that need to be adjusted to fit properly the real system. These free parameters include the position of atoms, the hopping parameters of section 1.1.2, the on-site parameters and, in the present work, the effect of the magnetic field. The hypotheses made on the geometrical arrangement of atoms and on the hopping parameters are detailed in this section.

4.1.1 Hypotheses on the geometrical structure

As discussed in section 3.3.1, graphene exhibits a moiré pattern when placed on an hBN substrate. The hypotheses that concern the geometrical structure of this system are listed below.

1. The hBN substrate is composed of many layers of atomic planes. It is logically very thick compared to graphene and does not deform when graphene is placed on it. The hBN substrate has therefore the geometry of a free hBN layer, with the lattice parameter $a = 2.504$ Å, as discussed in section 1.3.2.

2. Graphene only interacts with the closest layer of hBN. For the mechanical interactions, it is coherent in the sense that graphene interacts with Van der Waals interactions that decrease as d^{-4} in 2D systems, with d the distance between the two planes [23].

3. Graphene remains totally isomorphic to its free configuration. In other words, its lattice parameter a can change uniformely to adjust on top of hBN, as discussed in section 4.2.2. It leads to a uniform straining of the lattice. However, no local strain is considered. If it is not the case, a strain field having the same periodicity as the moiré lattice would appear and, with it, a local strain energy. The

hypothesis of no local strain is made by considering that the addhesion energy between graphene and hBN is weaker than this local strain energy [23]. This is quite a strong hypothesis because strain fields are observed in experimental systems [79, 80]. However, theoretical studies about the effect of relaxation suggest that it does not lead to dramatic changes over the electronic propreties of graphene [24, 25].

4. Graphene is considered to be totally flat on top of hBN. Once again, experimental observations go against this hypothesis. When graphene is placed on top of hBN, the interlayer spacing between the plane varies as a function of the position in the moiré lattice [17, 12]. However, as seen in section 4.2.4, the interlayer distance variation is quite small and its effect can be neglected.

4.1.2 Hypotheses on the tight-binding model

The tight-binding (TB) Hamiltonian is built with hopping parameters (the Slater-Koster (SK) parameters of section 1.1.2). Those parameters are found based on DFT calculations, as described in section C.2 of appendix C. Here are the hypotheses made on the hopping parameters.

5. The TB model is exclusively built with the p_z orbitals of graphene and hBN, as discussed in section 1.2 and 1.3.

6. The orbitals of two different atoms are orthogonal, such as the overlap integral of expression 1.13 is zero except for the on-site term given by $\mathbf{R}_i = \mathbf{R}_j$ (and consequently $i = j$). That is

$$\int \phi_j^*(\mathbf{r} - \mathbf{R}_j)\phi_i(\mathbf{r} - \mathbf{R}_i)\mathrm{d}\mathbf{r} = \delta_{\mathbf{R}_i\mathbf{R}_j} \tag{4.1}$$

   where $\delta_{\mathbf{R}_i\mathbf{R}_j}$ is a function equal to 0 for $\mathbf{R}_i \neq \mathbf{R}_j$ and to 1 for $\mathbf{R}_i = \mathbf{R}_j$.

7. The tight-binding model is limited to the third nearest-neighbours in the plane of graphene and hBN. This approximation is often used in the literature [81].

8. The interlayer SK parameters are limited to a cutting radius of 4Å.

9. The SK parameters are limited to the interactions between the nearest neighbouring layers.

10. The absolute value of the SK parameters of the carbon-boron bond and the carbon-nitrogen bond are considered to be the same. Only the sign changes.

11. The effect of the angle α between two atoms (see figure 4.1a) is ignored for the SK parameter of the p_z orbitals. As described in section 1.1.2, the SK parameters between two orbitals depends on the direction cosines l, m and n. Only the s orbitals, which have a spherical symmetry, have no dependence on these cosines. The p_z orbitals are therefore also assumed to have a spherical symmetry around the atoms, as shown in figure 4.1b. However, even if the effect of the angle is ignored, the distance dependence of the SK parameter is adjusted to fit as well as possible to the results of the DFT calculations.

4.2 Construction of the commensurate supercell

The purpose of this section is to construct a superlattice that presents a moiré pattern, as described in section 3.3.1. However, the superlattice must be periodic so that the Bloch theorem can be applied in order to construct a tight-binding model. The first section gives the conditions on the geometry of two lattices that allows construction of a periodic superlattice. The second section explains the way to implement this condition in the case of graphene on hBN. All the lattices are two-dimensional.

4.2.1 Commensurate and incommensurate lattices

The superposition of two lattices form what is called a *superlattice*. Two lattices are said to be commensurate if it is possible to define a supercell in the superlattices, so that the supercell is repeated periodically in the whole superlattice. The supercell, if it exists, is defined by two vectors $\mathbf{L}_1$ and $\mathbf{L}_2$. These two *superlattice vectors* give the smallest period of the superlattice. The condition to form such a supercell

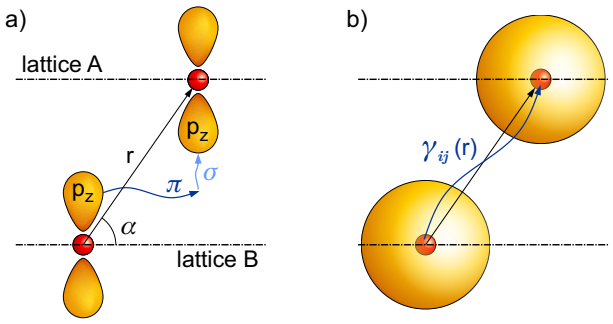

Figure 4.1: Suppression of the angle dependence of the Slater-Koster (SK) parameters. **(a)** Schematic of two superposed lattices A and B. The p_z orbitals are not symmetric in the direction of the vector $\mathbf{r}$. As described in table 1.1, the SK parameter has a component of a π bonding in the plane and of a σ bonding in the z direction. **(b)** In the tight-binding model, the angle dependence is ignored and the complete expression of the SK parameter is replaced by an expression γ_{ij} that only depends on the distance between the two atoms. In that situation, the p_z orbitals are replaced by s-like orbitals, having a spherical symmetry.

is that the two initial lattices share both the periodicity $\mathbf{L}_1$ and $\mathbf{L}_2$. This can be translated by the two conditions

$$\mathbf{L}_1 = k_1\mathbf{a}_1 + k_2\mathbf{a}_2 = \kappa_1\tilde{\mathbf{a}}_1 + \kappa_2\tilde{\mathbf{a}}_2 \tag{4.2a}$$
$$\mathbf{L}_2 = n_1\mathbf{a}_1 + n_2\mathbf{a}_2 = \eta_1\tilde{\mathbf{a}}_1 + \eta_2\tilde{\mathbf{a}}_2 \tag{4.2b}$$

with $\mathbf{a}_1$ and $\mathbf{a}_2$ the lattice vectors of the first lattice, and $\tilde{\mathbf{a}}_1$ and $\tilde{\mathbf{a}}_2$ those of the second lattice. A periodic supercell can be constructed if there exist two couples of integers (k_1, k_2) and (κ_1, κ_2) such as condition 4.2a is fulfilled, and two couples of integers (n_1, n_2) and (η_1, η_2) such as condition 4.2b is fulfilled. It indicates that the two lattices share a periodicity in common, along two different directions. Those directions correspond to the superlattice vectors $\mathbf{L}_1$ and $\mathbf{L}_2$. Section 4.2.2 illustrates this theoretical definition in the case of a lattice of graphene placed on a lattice of hBN.

Finally, an incommensurate lattice is a superlattice where it is not possible to define a periodic supercell. No couple of integers fulfils the conditions 4.2a and 4.2b.

4.2.2 Derivation of the parameters of a commensurate lattice

In the literature [16, 22], a description of a moiré lattice can be found for a system of graphene on hBN. The unit cell parameters are given as a function of the angle of rotation θ and the lattice mismatch ϵ between graphene and hBN. The lattice parameter L of the supercell is given by the following expression

$$L = \frac{1+\epsilon}{\sqrt{\epsilon^2 + 2(1+\epsilon)(1+\cos\theta)}}a \tag{4.3}$$

where a is the lattice parameter of graphene if ϵ is defined as $a_{\text{hBN}} = (1+\epsilon)a_{\text{G}}$ or a is the lattice parameter of hBN if ϵ is defined as $a_{\text{G}} = (1+\epsilon)a_{\text{hBN}}$. The supercell is then described by two vectors $\mathbf{L}_1$ and $\mathbf{L}_2$ having both a norm L. The angle ϕ between one of the vectors $\mathbf{L}_i$ and its corresponding primitive vector of graphene (resp. hBN) $\mathbf{a}_i$ is given by

$$\phi = \arctan\left(\frac{-\sin\theta}{1+\epsilon-\cos\theta}\right) \tag{4.4}$$

A consequence of this property is that the angle between $\mathbf{L}_1$ and $\mathbf{L}_2$ is the same as that between $\mathbf{a}_1$ and $\mathbf{a}_2$: 60°. However, the relations 4.3 and 4.4 are necessary but not sufficient to guarantee the periodicity of the supercell in order to form a commensurable lattice, as discussed in section 4.2.1. Some extra conditions have to be added.

The graphene lattice and the hBN lattice must be arranged in such a way that the supercell can be repeated to form a periodic moiré lattice. The starting point is to place the two lattices with an atom of

carbon on top of an atom of boron at the origin of the supercell, that is, at the $x-y$ coordinate $(0,0)$. The condition to ensure a periodic structure is to have an atom of boron and an atom of carbon at positions $\mathbf{L}_1$, $\mathbf{L}_2$ and $\mathbf{L}_1+\mathbf{L}_2$, as discussed in section 4.2.1. It is illustrated for the atoms of boron in figure 4.2 with the atoms labelled from I to IV.

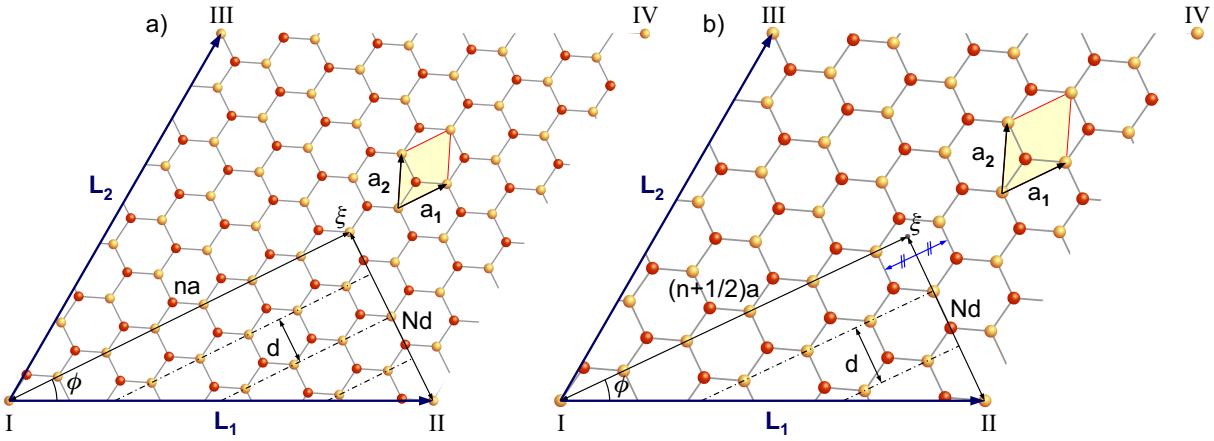

Figure 4.2: Construction of the supercell for the hBN lattice. Boron atoms are in yellow and nitrogen atoms in red. **(a)** Disposition of the atoms for $n=7$ and $N=4$. The supercell is periodic since there is an atom of boron in each corner of the supercell. **(b)** Disposition of the atoms for $n=5$ and $N=3$.

First, the presence of a boron atom at position $\mathbf{L}_1$ guarantees the presence of a boron atom at each corner of the supercell. This is because the angles between the vectors of the supercell $\mathbf{L}_i$ and between the hBN primitive vectors $\mathbf{a}_i$ are the same. In other words, if the condition 4.2a is fulfilled, condition 4.2b is also fulfilled. It is therefore sufficient to derive the conditions of periodicity with the atom at the bottom right corner of the supercell, now called atom II.

In figure 4.2, it appears that the boron atoms are aligned, logically, along straight lines parallel to primitive vector $\mathbf{a}_1$ (dotted lines in figure 4.2). The distance between two parallel nearby lines is denoted by d. A first condition to have a boron atom at position $\mathbf{L}_1$ is that one of those straight line passes by this point. It implies that the line passing by atom I and the one passing by atom II are separated by an integer multiple of d, therefore a distance Nd. This is the distance between atom II and position ξ in figure 4.2.

A second condition must be added to ensure atom II is located at position $\mathbf{L}_1$ and not elsewhere on the dotted line. Two cases must be distinguished. The case where N is even, and the case where N is odd.

- If N is even, the atoms on the line, including atom I, are aligned to the atoms of the line including atom II. The condition is thus to have an atom at position ξ in figure 4.2, directly above the position of atom II, by taking the perpendicular to the lines. The distance between atom I and position ξ must be an integer multiple n of the lattice parameter a of hBN, that is na.
- If N is odd, the atoms of the line passing by atom I are shifted by half the lattice parameter, $a/2$, compared to the line passing by atom II. To be sure to have an atom at position II, there must be an atom at a distance $a/2$ from position ξ. The distance between atom I and position ξ is therefore $(n+1/2)a$.

To group the two cases in one notation the distance between atom I and position ξ must be $\tilde{n}a$ with $\tilde{n}=n$ if N is even and $\tilde{n}=n+1/2$ if N is odd, with n the number of atom between atom I and position ξ.

By determining a value of n and N, the angle ϕ can be easily found by the relation

$$\phi = \arctan\left(\frac{Nd}{\tilde{n}a}\right) \tag{4.5}$$

In the same way the value of L is given by

$$L = \frac{\tilde{n}a}{\cos\phi} \tag{4.6}$$

However, graphene must still be added on top of the hBN lattice.

By hypothesis 1 of section 4.1, the system is made of a rigid substrate of hBN on top of which is deposited the layer of graphene. In order to conserve the periodicity of the lattice, graphene must adjust on top of hBN to have both an atom at position $(0,0)$ and at position $\mathbf{L}_1$, on top of the boron atom II of figure 4.2a. The condition is thus the same as relation 4.5 and4.6. However, the parameters a, d, N and $\tilde{n}$ of hBN must be replaced by those of graphene, labelled with a subscript G. The angle θ between the lattices of graphene and hBN must also be taken into account. It gives the two relations

$$\phi - \theta = \arctan\left(\frac{N_G d_G}{\tilde{n}_G a_G}\right) \tag{4.7}$$

$$L = \frac{\tilde{n}_G a_G}{\cos(\phi - \theta)} \tag{4.8}$$

In relation 4.8, L is fixed by condition 4.6. The lattice parameter of graphene is given by $a_G = (1+\epsilon)a$ with $\epsilon < 0$, the lattice mismatch. There are then two free parameters: θ and ϵ. Those to parameters are fixed by the values of $\tilde{n}_G$ and N_G. Because $a_G < a$, the number of atoms $\tilde{n}_G$ between atom I and position ξ' in graphene must be greater than $\tilde{n}$ in hBN. Further more, the angle θ is defined negative. It then gives a number of carbon atoms layers $N_G < N$.

A moiré supercell depends on two initial parameters, θ and ϵ, that determine the values of L and ϕ. However, in order to be commensurate, these four parameters must be expressed in terms of four integers $\tilde{n}$, N, $\tilde{n}_G$ and N_G, as made in equations 4.5 to 4.7. A Python code allowing to find the values of these four parameters that approach as close as possible the initial data θ and ϵ is given in section E.2 of appendix E. Figure 4.3b shows the final supercell of a periodic system of graphene on hBN for $n = 7$, $N = 4$ and $\theta = 3°$.

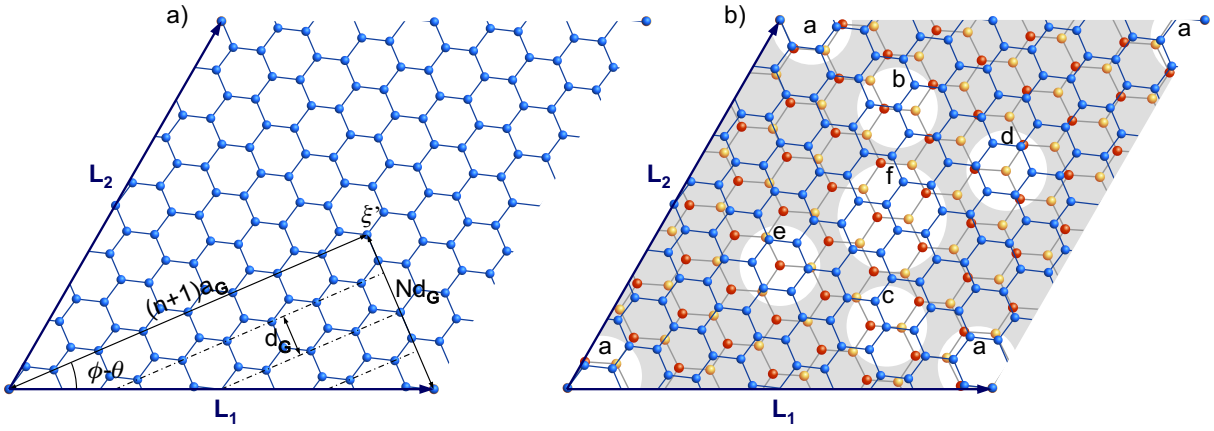

Figure 4.3: Adaptation of the graphene lattice to the supercell constructed in figure 4.2a. **(a)** Representation of the graphene lattice in the supercell, as made for hBN in figure 4.2. **(b)** Superposition of the graphene lattice on the hBN lattice described in figure 4.2a. The white circles highlight different stacking configurations. Each stacking configuration is labelled with a letter that refers to figure 4.4.

4.2.3 The different stacking configurations

As presented in figure 4.3b, different notable stacking configurations can be extracted from a moiré pattern. Those configurations are listed in figure 4.4. Based on these different configurations, DFT calculations have been performed by Simon Dubois in order to extract the hopping parameters between a carbon atom, and a boron or nitrogen atom. The inter-atomic distance between an atom in graphene and an atom in hBN varies depending on the configuration. It allows the extraction of parameters that depend on this inter-atomic distance, in the frame described by hypothesis 11 of section 4.1.

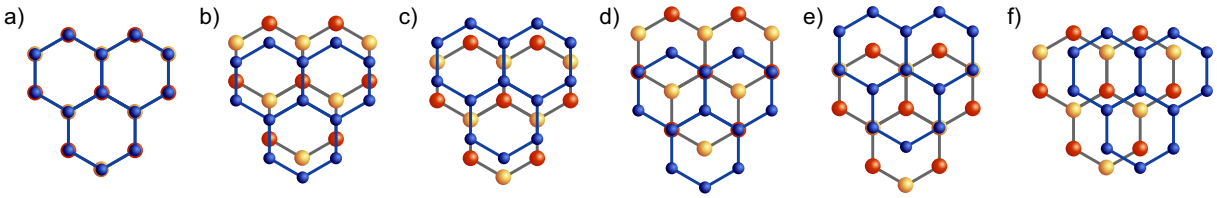

Figure 4.4: View of the different stacking configurations that appear in a moiré lattice. Carbon atoms are in blue, boron atoms in yellow and nitrogen atoms in red. Inspired by [23]. **(a-f)** The different configurations can be spotted in the moiré lattice of figure 4.3b.

4.2.4 Interlayer distance

The interlayer distance between the plane of graphene and of hBN has not yet been reported experimentally in the litterature. However, DFT calculations allow it to be estimated by considering Van der Waals interactions between the two planes [23]. However, as discussed in the beginning of chapter 1, it is not possible to perform DFT calculations in a complete moiré structure. The interlayer distance is then computed for the different stacking configurations of figure 4.4.

The stable interlayer distance turns out to be different for each configuration [23]. These distances were calculated by Simon Dubois with DFT calculations (see appendix C). They are reported in table 4.1.

Stacking configuration	(a)	(b)	(c)	(d)	(e)	(f)
Interlayer distance (Å)	3.60	3.57	3.54	3.57	3.42	3.51

Table 4.1: List of the interlayer distances for the different configurations (denoted by the letters a to f) of figure 4.4

The interlayer distance between graphene and hBN must normally stands between the interlayer distances of bulk graphite and bulk hBN [82]. The value of bulk graphite is 3.34 Å [83, 84] and the one of hBN is 3.3 Å [48, 49]. The values reported in table 4.1 are then probably slightly overestimated, since the more compact configuration - (e) in figure 4.4 - is larger than the range given by exprimental data.

By hypothesis 4 of section 4.1, the interlayer distance is considered to be constant. This constant value is established by the mean value of the parameters of table 4.4 and is equal to 3.535 Å.

4.3 Implementation of the magnetic field in the tight-binding model

In section 1.1.3, the method to include the magnetic field in the TB model is discussed. The magnetic field induces a phase term in the hopping parameter (between two atoms i and j) expressed by equation 1.24 as

$$t_{ij}(\mathbf{B}) = \exp\left(\frac{ie}{\hbar}\int_{\mathbf{R}_i}^{\mathbf{R}_j}\mathbf{A}\cdot\mathrm{d}\mathbf{r}\right)t_{ij}(\mathbf{B}=0) \tag{4.9}$$

where $\mathbf{B} = \boldsymbol{\nabla}\times\mathbf{A}$.

However, some problems appear for implementation of the TB model. To see that, a constant magnetic field $\mathbf{B}_z$ can be considered. In the Landau gauge, the vector potential is expressed as $\mathbf{A} = (0, B_z x, 0)$. The vector potential of the Landau gauge is not periodic in space. It leads to a non-periodic hopping parameter from one unit cell to another, which prevents use the Bloch theorem. The Landau gauge cannot be used to implement the TB model, and a periodic gauge is therefore needed.

4.3.1 Construction of a periodic potential vector

A nonperturbative gauge solution of this problem was given by A. Trellakis in 2003 [85]. Its development departs from the Hamiltonian

$$\frac{1}{2m}(\hat{\mathbf{p}} + e\mathbf{A})^2 + V(\mathbf{r}) \tag{4.10}$$

where $V(\mathbf{r})$ is the lattice potential and $\mathbf{A}$ is the vector potential of a constant magnetic field, such as $\mathbf{A} = \mathbf{B}_z \times \mathbf{r}$. The goal is to find a gauge transformation that makes the vector potential periodic in order to find the Hamiltonian

$$\frac{1}{2m}(\hat{\mathbf{p}} + e\mathbf{A}_p)^2 + V(\mathbf{r}) \tag{4.11}$$

with $\mathbf{A}_p$ the new vector potential that is periodic. This Hamiltonian must give the same eigenvalues and eigenvectors in order to keep the physical system intact. This is achieved in [85] by taking a magnetic field such as $\mathbf{B}_z = \boldsymbol{\nabla} \times \mathbf{A}_p$, given by

$$\mathbf{B}_z = B\mathbf{e}_z - \phi \sum_{\mathbf{R}_l} \delta(\mathbf{r} - \mathbf{R}_l)\mathbf{e}_z \tag{4.12}$$

The last term, called *flux lines lattice* (FLL) and denoted by $\mathbf{B}_{fl}$, is essential. It describes a periodic lattice of infinitely thin flux lines, where ϕ is the magnetic flux, δ is the delta function and $\mathbf{R}_l$ is a vector that has the periodicity of the FLL. $\mathbf{R}_l = n_1\mathbf{c}_1 + n_2\mathbf{c}_2$ with $\mathbf{c}_1$ and $\mathbf{c}_2$ the lattice vectors of the FLL. This FLL is represented in figure 4.5.

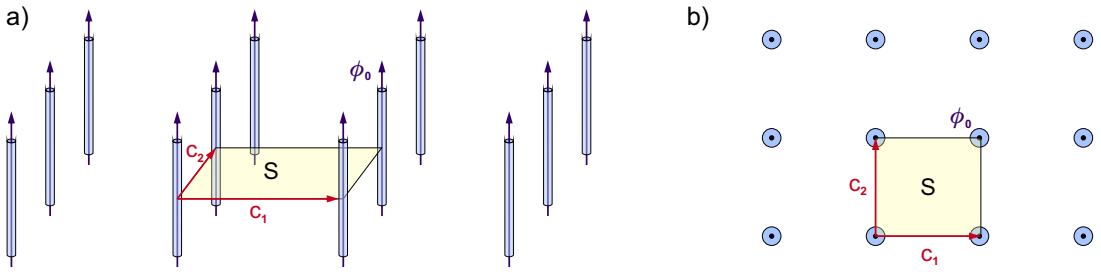

Figure 4.5: Representation of the flux line lattice (FLL). Inspired by [87]. **(a)** Three-dimensional view of the FLL. $\mathbf{c}_1$ and $\mathbf{c}_2$ are the lattice vectors. Each flux line contains a flux equal to the magnetic flux quantum ϕ_0. The magnetic flux lines are oriented along the z direction.**(b)** Two-dimensional view of figure a).

In order to guarantee the periodicity, the magnetic field B of equation 4.12 must cancel the average magnetic flux and is then given by

$$B = B_{fl} = \frac{\phi}{|\mathbf{c}_1 \times \mathbf{c}_2|} \tag{4.13}$$

with $|\mathbf{c}_1 \times \mathbf{c}_2| = S$, the surface of the magnetic unit cell. Before going further in the development, it is important to show that the presence of the FLL does not affect the physical behaviour of the system.

In equation 4.12, an FLL $\mathbf{B}_{fl}$ has been substracted to the constant magnetic field $B\mathbf{e}_z$. The physical behaviour of the system remains unchanged if the presence of the FLL does not affect any experimental measurement. In other words, the presence of the magnetic flux lines must not affect the transport of electrons. As seen in section 1.1.3, the vector potential $\mathbf{A}_{fl}$ related to the FLL $\mathbf{B}_{fl}$ introduces a phase shift when an electron is translated in the lattice. If two electrons take a different path and aquire a different phase, they interfere and the electronic transport is modified; this is the Aharonov-Bohm effect [86].

The phase difference can be studied for two electrons that travel on the borders of the FLL unit cell. The first electron travels at the right of the flux quantum (blue path in figure 4.6a) and the second at its left (orange path in figure 4.6a). The first undergoes a translation $\hat{T}_{\mathbf{c}_1}\hat{T}_{\mathbf{c}_2}$ whereas the second $\hat{T}_{\mathbf{c}_2}\hat{T}_{\mathbf{c}_1}$. The phases brought by those two translations must be identical, that is, $\hat{T}_{\mathbf{c}_1}\hat{T}_{\mathbf{c}_2} = \hat{T}_{\mathbf{c}_2}\hat{T}_{\mathbf{c}_1}$ [87]. With the use of the properties 1.17a and 1.17b, this equality can be written as

$$\hat{T}_{\mathbf{c}_1}\hat{T}_{\mathbf{c}_2} = \hat{T}_{\mathbf{c}_1}\hat{T}_{\mathbf{c}_2}\hat{T}_{-\mathbf{c}_2}\hat{T}_{-\mathbf{c}_1}\hat{T}_{\mathbf{c}_2}\hat{T}_{\mathbf{c}_1} \tag{4.14}$$

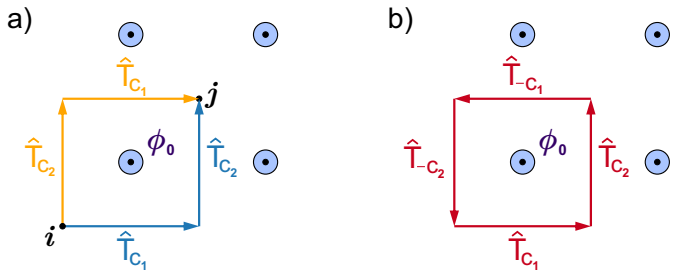

Figure 4.6: Apparition of a phase for electrons travelling around a flux line.v**(a)** An electron that follows the blue path (described by the translation operators $\hat{T}_{\mathbf{c}_1}\hat{T}_{\mathbf{c}_2}$) acquires a phase Δ_{1ij}. An electron that follows the orange path (described by the translation operators $\hat{T}_{\mathbf{c}_2}\hat{T}_{\mathbf{c}_1}$) acquires a phase Δ_{2ij}. **(b)** The phase difference $\Delta = \Delta_{1ij} - \Delta_{2ij}$ is equal to $\Delta_{1ij} + \Delta_{2ji}$. It corresponds to the phase difference caused by the red path (described by the translation operators $\hat{T}_{\mathbf{c}_1}\hat{T}_{\mathbf{c}_2}\hat{T}_{-\mathbf{c}_1}\hat{T}_{-\mathbf{c}_2}$).

The final condition for the two electrons to have the same phase is

$$\hat{T}_{-\mathbf{c}_2}\hat{T}_{-\mathbf{c}_1}\hat{T}_{\mathbf{c}_2}\hat{T}_{\mathbf{c}_1} = \mathbb{1} \tag{4.15}$$

This operator corresponds to four successive translations that form a cycle along the borders of the magnetic cell, as show in figure 4.6b. With the use of equation 1.20, the phase shift Δ brought by the operator $\hat{T}_{-\mathbf{c}_2}\hat{T}_{-\mathbf{c}_1}\hat{T}_{\mathbf{c}_2}\hat{T}_{\mathbf{c}_1}$ is given by

$$\Delta = \frac{e}{\hbar}\oint \mathbf{A}_{fl}\cdot \mathrm{d}\mathbf{r} \overset{\text{Stokes}}{=} \frac{e}{\hbar}\int_S \mathbf{B}_{fl}\cdot \mathrm{d}\mathbf{S} = \frac{2\pi\phi}{\phi_0} \tag{4.16}$$

This development has been performed with the Stokes formula. ϕ is the magnetic flux across the surface S of the magnetic unit cell and ϕ_0 is the magnetic flux quantum.

The phase difference Δ caused by the magnetic flux lines has no influence on the electronic transport when it is a multiple of 2π. This condition fulfils the relation 4.15 and guarantees that the presence of the FLL $\mathbf{B}_{fl}$ does not introduce any interference experimentally detectable. Therefore, the magnetic flux ϕ must be an integer multiple of the magnetic flux quantum $\phi_0 = e/h$ such as

$$\mathbf{B}_z = B_0\mathbf{e}_z - N\phi_0\sum_{\mathbf{R}_l}\delta(\mathbf{r}-\mathbf{R}_l)\mathbf{e}_z \qquad \text{with } N = 0, 1, 2, ... \tag{4.17}$$

Condition 4.13 imposes that $B_0 = N\phi_0$.

The periodic vector potential $\mathbf{A}_p$ of equation 4.11 still needs to be determined. It is found in [85] by taking the ansatz $\mathbf{A}_p(x,y) = \mathbf{e}_z \times \boldsymbol{\nabla}\chi(x,y)$. The solution is given by the two relations

$$\chi(\mathbf{r}) = -\frac{\phi_0}{4\pi}\ln\left(\sum_{\mathbf{G}} a_{\mathbf{G}}(1-\cos(\mathbf{G}\cdot\mathbf{r}))\right) \tag{4.18a}$$

$$a_{\mathbf{G}} = (-1)^{k_1+k_2+k_1k_2+1}\exp\left(\frac{-SG^2}{8\pi}\right) \tag{4.18b}$$

where $\mathbf{G} = k_1\mathbf{d}_1 + k_2\mathbf{d}_2$, with $\mathbf{d}_1$ and $\mathbf{d}_2$ the reciprocal vectors of the FLL.

4.3.2 Precautions to follow for the implementation

In section 4.3.1, equation 4.18 gives an expression for a periodic vector potential. However, some important precautions must be taken before to include this formalism in the tight-binding model. Indeed, the presence of the FLL may lead to numerical problems. The easier way to see that problems concerns the expression 4.18. The periodic vector potential directly depends on $\chi(\mathbf{r})$. However, $\chi(\mathbf{r})$ goes to infinity when $\mathbf{G}\cdot\mathbf{r} = 2\pi n$, with n an integer. It corresponds to the position of the flux lines in the FLL. As explained in [85], this divergence comes from the gauge transformation that is singular.

In expression 4.9, the vector potential leads to a phase in the hopping parameter between atom i and j. The phase is given by the integration of the vector potential along a path between atoms i and j. It is essential that no flux line stands on (and even too much close to) the integration path. Indeed it would lead to numerical errors due to divergent behaviour of the vector potential.

4.3.3 Construction of a commensurable flux lines lattice

In order to follow the Bloch theorem, the FLL that leads to the periodic vector potential must be commensurable with the atomic lattice. The condition of commensurability was described in section 4.2.1. The cases of a simple atomic lattice and of a moiré lattice are treated in this section.

In a simple atomic lattice

The easier way to have a commensurate system is to take the same lattice vectors for the atomic lattice and the FLL. That is, $\mathbf{c}_1 = \mathbf{a}_1$ and $\mathbf{c}_2 = \mathbf{a}_2$, with $\mathbf{c}_{1,2}$ the lattice vectors of the FLL and $\mathbf{a}_{1,2}$ the lattice vectors of the atomic lattice.

However, this definition does not allow to cover an interesting range of the magnetic field. Indeed, only one flux line is located in each unit cell of the atomic lattice. By equation 4.17, the value of the flux in the flux line is $N\phi_0$. It leads to a value of the magnetic field of $B = N\phi_0/S$. Two problems emerge from this expression,

- The first problem is related to the magnitude of the field. As described in figure 3.10, the surface of the unit cell is extremely small. It leads to an unrealistic value of the magnetic field.

- The second problem concerns equation 3.6. It expresses the value $\alpha = \phi/\phi_0$ that is at the basis of the construction of the Hostadter's butterfly. It appears that, for values of $\phi = N\phi_0$, α only takes integer values N. In Hofstadter's butterfly, each integer value of α gives the same energy dispersion. Therefore, the range of magnetic field available does not allow to study the internal structure of the butterfly.

The way to remedy to that problem is to create a supercell made of $n_1 \times n_2$ cells of the simple atomic lattice. The superlattice vectors are thus $\mathbf{L}_1 = n_1\mathbf{a}_1$ and $\mathbf{L}_2 = n_2\mathbf{a}_2$. By setting N magnetic flux quanta in the supercell, it will give a magnetic flux $\phi = N\phi_0/(n_1n_2)$. It leads to a value of alpha $\alpha = N/(n_1n_2)$.

By looking back to equation 3.11, it appears that the two essential coefficients p and q can be determined by adjusting the size of the supercell n_1n_2 and the number of quanta N so that

$$p \equiv N \qquad \text{and} \qquad q \equiv n_1n_2 \tag{4.19}$$

In the moiré superlattice

The moiré superlattice has already a large area so that the value $\alpha = \phi/\phi_0 = 1$, where ϕ is the flux through the supercell, leads to a weak value of the magnetic field, as discussed in section 3.3.1. However, to reproduce the internal structure of Hofstadter's butterfly, as depicted in figure 3.15a and 3.19d, it is necessary to explore values $\alpha < 1$. This is achieved by creating a *super-supercell*. A still bigger supercell is created by duplicating the moiré supercell, as made with the unit cell for the simple lattice.

4.4 The Ewald potential model

As discussed in section 3.3.1, hBN acts as a weak potential on graphene. In section 2.1.2, it is shown that a weak potential opens gaps at the crossing of two energy bands. Those gaps are visible in the DOS of graphene placed on top of hBN (see figure 3.13a). Experimental studies have also highlighted the opening of gaps due to a potential associated to hBN [26, 77, 78]. The purpose of this section is to develop an effective potential caused by the substrate of hBN on the layer of graphene.

4.4.1 Construction of an electrostatic potential

The first idea was simply to take the electrostatic potential of the charged atoms of boron and nitrogen. The value of this potential at each position $\mathbf{r} = (x, y)$ in the graphene plane is

$$U(\mathbf{r}) = \sum_{\mathbf{r}_B} \frac{q_B}{\sqrt{(\mathbf{r} - \mathbf{r}_B)^2 + \delta^2}} + \sum_{\mathbf{r}_N} \frac{q_N}{\sqrt{(\mathbf{r} - \mathbf{r}_N)^2 + \delta^2}} \tag{4.20}$$

q_B and $\mathbf{r}_B$ are the charge and the positions (in the $x - y$ plane) of the boron atoms, q_N and $\mathbf{r}_N$ the charge and the positions of the nitrogen atoms and δ is the interlayer distance (along the z direction) between graphene and hBN. As discussed in section 4.1, δ is considered to be constant. Obviously, the positions $\mathbf{r}_A$ and $\mathbf{r}_B$ are given by the periodicity of the lattice. Finally, the electronic charge lost by boron is won by nitrogen such as $q_N = -q_B$.

However, expression 4.20 can not be used in its actual form. Indeed, the sum on the boron atoms and the sum on the nitrogen atoms have the unfortunate habit to be divergent. Indeed they are series that go as 1 over the distance r. Fortunately, the divergence of expression 4.20 can be avoided by using what is known as the Ewald summation [88]. The basic idea of the Ewald summation is to separate the sum into short-range terms and long-range terms. The sum over the short-range terms converge quickly in the real space and the sum over the long-range terms converge quickly in the Fourier space. The potential is then created from two terms as

$$U(\mathbf{r}) = U^S(\mathbf{r}) + U^L(\mathbf{r}) \tag{4.21}$$

where $U^S(\mathbf{r})$ is the short-range term and $U^L(\mathbf{r})$ the long-range term. The development of those two terms is made in the case of graphene on hBN in the *supporting informations* of reference [82]. The final expressions are given in E.3. Figure 4.7b gives the shape of the renormalized potential due to hBN in the plane of graphene. This potential is plotted on a rectangular cell that can be juxtaposed periodically to form the whole hBN lattice (as shown in figure 4.7a).

However, the amplitude of the electrostatic potential is extremely small. It has an amplitude $U_{max} \approx 1.5 \cdot 10^{-6}$ eV ($\approx 5 \cdot 10^{-5}$ Ha, coherent with [82]). This potential is too weak to have a visible effect on the electronic properties of graphene. A first conclusion is that the only electrostatic potential of the hBN atoms is not sufficient to explain the apparition of gaps as shown in figures 3.13a and 3.18a.

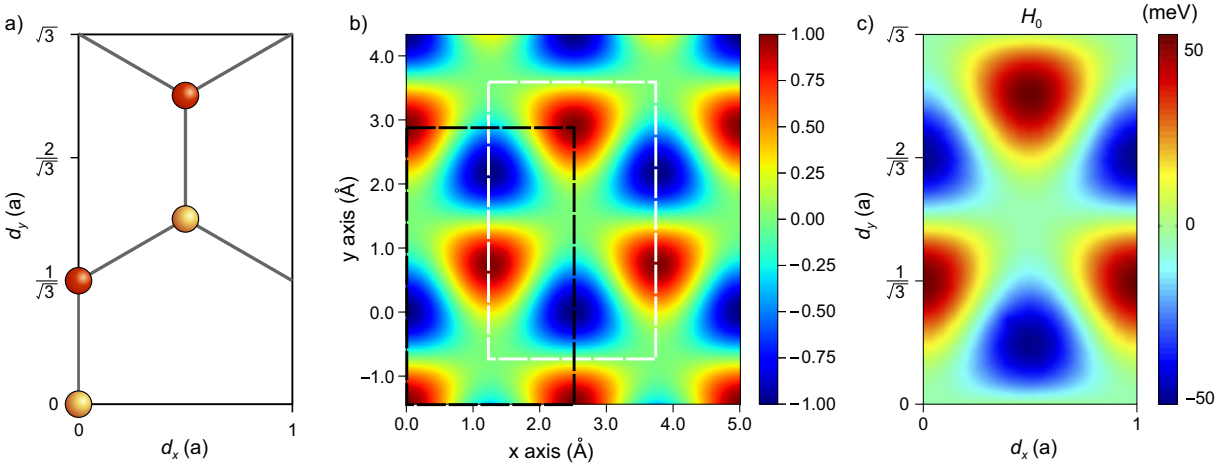

Figure 4.7: Potential due to the hBN substrate in the graphene plane. **(a)** The rectangle represents the cell used to build the periodic potential of hBN. The boron atoms are in yellow and the nitrogen atoms in red. **(b)** $1/r$ potential computed by using the Ewald calculation. The potential is renormalized and has an amplitude of 1. The black rectangle represents the cell in a) and the white rectangle the one in c). **(c)** Potential computed by using *ab initio* calculations. The potential of figure c) is borrowed from [27]

In order to make the effect of the potential visible, its amplitude has to be changed. In the following, the renormalized potential of figure 4.7b is used. The amplitude of the potential is simply adjusted by multiplying the potential by a given value of U_{max}.

Finally, one can ask if this potential has still a physical meaning. Indeed, the initial electrostatic potential loose its physical substance since its amplitude is adjusted by hand, by many orders of magnitude. Two arguments played in favour of the use of a $1/r$ potential with a chosen amplitude,

1. The shape of the potential gives a very good representation of the symmetries of hBN, as seen on figure 4.7b. It is not the case of a cosine-like potential for instance. Further more, the potential is due to the charge interactions between graphene and hBN. Even if those interactions are more complex than the simple electrostatic potential, the idea to associate them to a $1/r$ potential seems to be a reasonable assumption.

2. As a more persuasive argument, the shape of the $1/r$ potential is totally coherent with elaborated results found in litterature. Figure 4.7c gives the shape of the potential due to the hBN lattice found with a complete *Ab initio* calculation [27]. It is the same potential as the one of figure 4.7b.

4.4.2 The potential in the tight-binding model

The potential due to the hBN substrate transforms the initial Hamiltonian of the free graphene layer $\hat{H}_{\mathrm{G}}$ as

$$\hat{H} = \hat{H}_{\mathrm{G}} + U(\mathbf{r}) \tag{4.22}$$

The TB matrix element H_{ij} of equation 1.9 is therefore given by

$$H_{ij}^{\text{G-hBN}} = \frac{1}{N}\sum_{\mathbf{R}_j}\sum_{\mathbf{R}_i}\exp\left(i\mathbf{k}\cdot(\mathbf{R}_i-\mathbf{R}_j)\right)\int \phi_j^*(\mathbf{r}-\mathbf{R}_j)\left[\hat{H}_{\mathrm{G}}+U(\mathbf{r})\right]\phi_i(\mathbf{r}-\mathbf{R}_i)\mathrm{d}\mathbf{r} \tag{4.23}$$

This equality can be expressed with two terms as

$$H_{ij}^{\text{G-hBN}} = H_{ij}^{\mathrm{G}} + \frac{1}{N}\sum_{\mathbf{R}_j}\sum_{\mathbf{R}_i}\exp\left(i\mathbf{k}\cdot(\mathbf{R}_i-\mathbf{R}_j)\right)\int \phi_j^*(\mathbf{r}-\mathbf{R}_j)U(\mathbf{r})\phi_i(\mathbf{r}-\mathbf{R}_i)\mathrm{d}\mathbf{r} \tag{4.24}$$

where H_{ij}^{G} is the matrix element of graphene without hBN, related to $\hat{H}_{\mathrm{G}}$. Because the potential $U(\mathbf{r})$ is a scalar, it does not act on the wave functions. Therefore, by hypothesis 6 of section 4.1, The function $U(\mathbf{r})\phi_i(\mathbf{r}-\mathbf{R}_i)$ is always orthogonal to $\phi_j^*(\mathbf{r}-\mathbf{R}_j)$. It leads to the suppression of all the terms with $\mathbf{R}_i \neq \mathbf{R}_j$. The only potential terms that are not cancelled in equation 4.24 are the on-site terms expressed as

$$U_{ii} = \frac{1}{N}\sum_{\mathbf{R}_i'}\sum_{\mathbf{R}_i}\int \phi_i^*(\mathbf{r}-\mathbf{R}_i')U(\mathbf{r})\phi_i(\mathbf{r}-\mathbf{R}_i)\mathrm{d}\mathbf{r} \tag{4.25}$$

where $\mathbf{R}_i'$ and $\mathbf{R}_i$ account for the position of atom i in two different unit cells. Here, another hypothesis must be made. The orbitals overlap of the atoms i in two distinct unit cells is negligible, such that the equation 4.25 is only different from 0 for $\mathbf{R}_i \neq \mathbf{R}_i'$. Finally, one sum over the $\mathbf{R}_i$ subsists and give N integrals of identical values.

As a last hypothesis, the potential can be considered as constant around the position $\mathbf{R}_i$ of atom i. It then takes the value $U(\mathbf{R}_i)$ and, for normalized wave functions, the on-site term becomes simply

$$U_{ii} = U(\mathbf{R}_i) \tag{4.26}$$

As a conclusion, the effect of the potential is only added to the diagonal terms ii of the matrix $\mathbf{H}$ of the TB system 1.8. Further more, the potential terms ii simply take the value of the external potential at the position of atom i. The potential due to the hBN on graphene in a commensurate moiré lattice is shown in figure 4.8. The different stacking configurations are clearly highlighted in this figure.

4.5 The complete tight-binding model

In the previous section, a model based on an electrostatic-like potential has been presented. However, it is an extremely simple model and it ignores a lot of interactions that occur between the two atomic layers of graphene and hBN. Indeed, in the potential model, only the diagonal terms U_{ii} of equation 4.26 are added to the TB Hamiltonian $\hat{H}_{\mathrm{G}}$ of the free graphene layer. A totally complete Hamiltonian

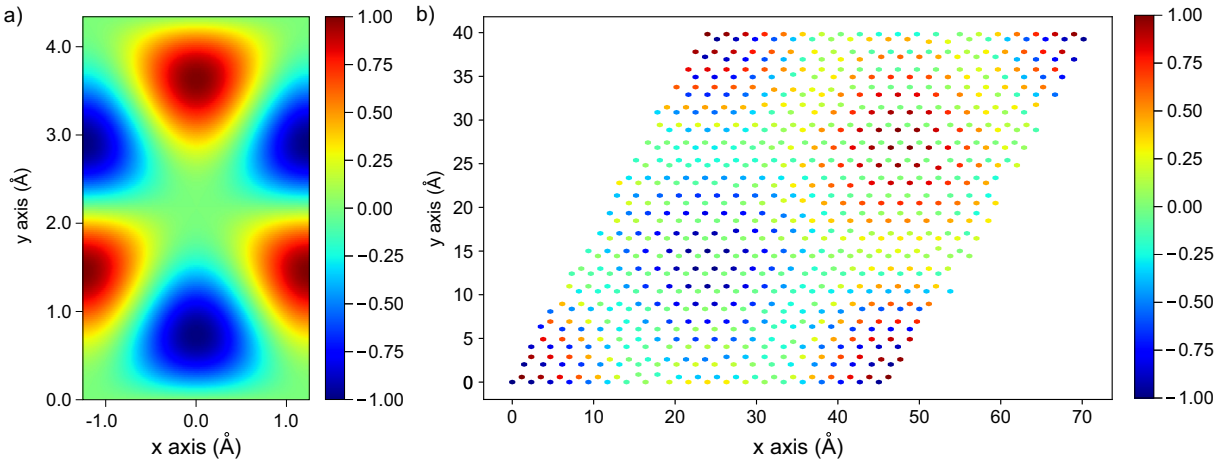

Figure 4.8: Description of the on-site potential due to hBN on the graphene layer. The figures has been plotted by using the code of the potential presented in section E.3 of appendix E. **(a)** Map of the renormalized potential as illustrated in figure 4.7b. **(b)** Map of the on-site potential for each atom of carbon. Each dot corresponds to a graphene atom and its color gives the magnitude of the potential due to the presence of the hBN layer. The magnitude of the potential can be compared to figure a). The different stacking configurations are clearly highlighted in this figure. It can be compared to figure 4.3b and 4.4.

would consider the whole system of graphene on hBN. Its expression is derived in section 4.5.1. Based on that definition, the tight-binding Hamiltonian is constructed in section 4.5.2. Finally a method to light the tight-binding system is presented in section 4.5.3. The goal of this model is to compute Hofstadter's butterfly in a single layer of graphene placed on an hBN substrate and to compare it to the experimental results of section 3.3.3.

4.5.1 Development of the general interaction Hamiltonian

As a starting point, one can consider the Hamiltonian $\hat{H}_{\text{ni}}$ of two non-interacting layers of graphene and hBN. This Hamiltonian and the related Schrödinger equation can be written as

$$\hat{H}_{\text{ni}} = \begin{pmatrix} \hat{H}_{\text{G}} & 0 \\ 0 & \hat{H}_{\text{hBN}} \end{pmatrix}, \qquad \hat{H}_{\text{ni}} \begin{pmatrix} \psi_{\text{G}} \\ \psi_{\text{hBN}} \end{pmatrix} = E_{\text{ni}} \begin{pmatrix} \psi_{\text{G}} \\ \psi_{\text{hBN}} \end{pmatrix} \tag{4.27}$$

The two systems are totally decorrelated and the total Hilbert space is a direct product of the Hilbert spaces of graphene and hBN **cite Cohen?**. The band structure of graphene and hBN are not modified.

By introducing an interaction between the two atomic planes, the total Hamiltonian is changed, as the total wave function. The two initial systems are not decorelated anymore. It is translated by the apparition of off-diagonal terms in Hamiltonian 4.27 [22] as

$$\hat{H}_{\text{tot}} = \begin{pmatrix} \hat{H}_{\text{G}} & \hat{H}_{\text{int}}^{\dagger} \\ \hat{H}_{\text{int}} & \hat{H}_{\text{hBN}} \end{pmatrix}, \qquad \hat{H}_{\text{tot}}\psi = E_{\text{tot}}\psi \tag{4.28}$$

4.5.2 Definition of the tight-binding Hamiltonian

The TB Hamiltonian can be build from the construction of the Hamiltonian 4.28. At the term $\hat{H}_{\text{G}}$ corresponds the matrix elements H_{ij}^{G} where i and j are carbon atoms in the graphene plane. At the term $\hat{H}_{\text{hBN}}$ corresponds the matrix elements H_{ij}^{hBN}, where i and j are boron or nitrogen atoms. Finally, at the term $\hat{H}_{\text{int}}$ corresponds the matrix elements H_{ij}^{int} where i corresponds to a carbon atom and j corresponds to either a nitrogen or a boron atom.

The hopping parameters

By equation 1.11 and definition 1.14, each matrix element for $i \neq j$ can be expressed as

$$H_{ij} = \sum_{\mathbf{R}} \exp(-i\mathbf{k}\cdot\mathbf{R})\gamma_{ij}(\mathbf{R}) \tag{4.29}$$

By hypothesis 7 of section 4.1, the hopping parameter is limited to the third nearest-neighbour in the plane of graphene and hBN. By hypothesis 8, a cut-off radius is defined for the bond between the carbon atoms from one hand and the boron or nitrogen atoms on the other hand. With those two hypotheses, the hopping parameters $\gamma_{ij}(\mathbf{R})$ can be defined as it is made in figure 4.9. In the case of a supercell, the dimensions of that supercell are generally much more higher than the maximal distance between two nearest-neighbours. There is consequently only one term in the sum of equation 4.29 because all the links are contained in the supercell.

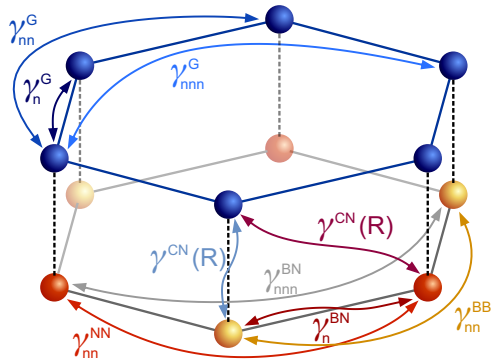

Figure 4.9: Definition of the hopping parameters between a layer of graphene and of hBN. The carbon atoms are coloured in blue, the boron atoms in yellow and the nitrogen atoms in red. The hopping parameters are limited to the third nearest-neighbour in the plane. A cut-off radius is defined for the interlayer parameters.

In the case of graphene, the nearest-neighbouring atoms are at the same distance in all the lattice. This is the same for the second and third nearest-neighbours. The values of the hopping parameters are therefore uniquely defined as γ^{C}_{n}, γ^{C}_{nn} and γ^{C}_{nnn}, following the same definitions as in section 1.2.

In the hBN layer, the nearest-neighbours form a couple of boron and nitrogen atoms. It is denoted by γ^{BN}_{n}. The two second nearest-neighbours are two atoms of the same type. There are then one hopping parameter for boron, γ^{BB}_{nn}, and one hopping parameter for nitrogen, γ^{NN}_{nn}. The third nearest-neighbours form again a couple of a boron and a nitrogen atom and is expressed as γ^{BN}_{nnn}.

The interplanar hopping parameters depend on the distance between a carbon atom in the graphene plane and a boron or nitrogen atom in the hBN plane. As explained by hypothesis 11, only the distance between two atoms of different layers matters. The expression of the two associate hopping parameters are $\gamma^{CB}(\mathbf{R})$ and $\gamma^{CN}(\mathbf{R})$. As described in hypothesis 11, for a same distance $\mathbf{R}_0$, $\gamma^{CB}(\mathbf{R}_0) = -\gamma^{CN}(\mathbf{R}_0)$. Finally, the dependence on the distance $\mathbf{R}$ of the hopping parameters is given by the following arbitrary function,

$$\gamma(\mathbf{R}) = \gamma_0 \left[\alpha \exp(-\beta \left|\mathbf{R}\right|^{\eta})\right] \tag{4.30}$$

where γ_0 is the hopping parameter for the crystal in its free configuration and the parameters α, β and η are parameters that give the spacial dependence of the hopping parameter.

The on-site parameters

The on-site parameters correspond to the matrix elements H_{ij} with $i = j$. The value of the on-site parameter of an atom is given by the energy of this atom, compared to a reference. Here the energy of the carbon atoms is taken as reference such as $H^{G}_{ii} = 0$. The on-site parameters of the boron and nitrogen atoms are determined from this reference such as

$$H^{B}_{ii} - H^{G}_{ii} = \Delta^{B} \qquad\qquad H^{N}_{ii} - H^{G}_{ii} = \Delta^{N} \tag{4.31}$$

Numerical values of the matrix elements

With the definition off all those hopping parameters, it has been possible to fit the tight-binding band structure on a band structure obtained by DFT calculation. The parameters of graphene were also computed for different distances $|\mathbf{R}|$ in order to take the variation of the lattice parameter into account. Its lattice parameter can varies in the way described by hypothesis 3. The spatial dependence is expressed by the function of equation 4.30. The result of the fits are given in section C.2 of appendix C.

The matrix elements H_{ij}^{G} contain all the terms that depend on the hopping parameters of graphene, γ_n, γ_{nn} and γ_{nnn}. The matrix elements H_{ij}^{hBN} contain all the terms that depend on the hopping parameters of hBN, γ_n^{BN}, $\gamma_{nn}^{\mathrm{BB}}$, $\gamma_{nn}^{\mathrm{NN}}$ and $\gamma_{nnn}^{\mathrm{BN}}$. The numerical values of these parameters are given in table 1.2 for graphene and 1.3 for hBN.

The matrix elements H_{ij}^{int} contain all the terms that depends on the interlayer hopping parameters $\gamma^{\mathrm{CB}}(\mathbf{R})$ and $\gamma^{\mathrm{CN}}(\mathbf{R})$. These parameters have a spacial dependence expressed by equation 4.30. The numerical values of γ_0, α, β and η are presented in table 4.2.

TB param.	γ_0	α	β	η
γ^{CB}	-1	5.983	1.515	1
γ^{CN}	1	5.983	1.515	1

Table 4.2: Table of the coefficients of equation 4.30 that gives the interlayer hopping parameters between graphene and hBN found by adjusting the TB band structure on the DFT band structure.

Finally, the on-site parameter of boron and nitrogen, expressed by equation 4.31 are expressed in table 4.3

on-site param.	value (eV)
Δ^B	2.7
Δ^N	-2.0

Table 4.3: Table of the on-site coefficients of boron and nitrogen expressed by equation 4.31.

4.5.3 Decimation of the interaction terms

The complete TB Hamiltonian of the previous section is extremely heavy. Indeed, it includes a large number of hopping parameters, defined along a large number of inter-atomic paths. It has a strong impact on the diagonalisation time and, in the first version of the code, it was a real problem to find the position of the magnetic flux lines, as discussed in section 4.3.2.

Nevertheless, the size of the TB matrix can be reduced. The interaction between the graphene layer and the hBN layer is weak. It results in small interlayer hopping parameters. An approximation can be effectuated by departing from the Hamiltonian 4.28. The interaction Hamiltonian $\hat{H}^{\mathrm{int}}$, because it is weak, can be treated as a perturbation. The total Hamiltonian can be expressed in the second order perturbation as [22]

$$\hat{H}_{\mathrm{tot}}^{\mathrm{dec}} = \hat{H}_{\mathrm{G}} + \hat{H}_{\mathrm{int}}^{\dagger}(-\hat{H}_{\mathrm{hBN}})^{-1}\hat{H}_{\mathrm{int}} \tag{4.32}$$

Based on this Hamiltonian, each matrix element of graphene H_{ij}^{G} can be modified to take the effect of hBN into account. At the second order approximation, each matrix element of graphene has the form

$$\tilde{H}_{ij}^{\mathrm{G}} = H_{ij}^{\mathrm{G}} - \sum_n \frac{H_{in}^{\mathrm{int}} H_{nj}^{\mathrm{int}}}{H_{nn}^{\mathrm{hBN}}} \tag{4.33}$$

where i and j are labels of graphene atoms and n the label of an hBN atom. $\tilde{H}_{ij}^{\mathrm{G}}$ is the matrix element that accounts of the interaction with hBN and H_{nn}^{hBN} is the onsite term of atom n. The in-plane interaction terms of hBN are neglected.

4.5.4 Bilayer graphene on hBN

As described in section 3.3.2, Hofstadter's butterfly has also been observed in Bernal-stacked bilayer graphene (BLG), exhibiting a moiré pattern when placed on an hBN substrate. The Bernal-stacked configuration is shown in figure 4.10. The purpose of this section is to describe the model that is used to represent this system.

As outlined by hypothesis 9 of section 4.1, the hopping parameters are only considered for the neighbouring layers. The layer of graphene on top of the heterostructure does not interact with the hBN substrate. The model is therefore very similar to the one with single graphene of section 4.5. The model is changed by adding the links between the two layers of graphene, that are considered to be independent from the hBN substrate.

The hopping parameters that describe the interlayer interactions between two planes of graphene are abundant in litterature [89, 90, 91]. The interlayer parameters are adopted from [89]. Three hopping parameters outside the graphene planes are considered in this model. They are shown in figure 4.10. The parameters are denoted by γ_1, γ_3 and γ_4 to remain coherent with the notation of [89] and their values are given in table 4.4.

hopping parameter	γ_1	γ_3	γ_4
value (eV)	0.364	0.319	0.177

Table 4.4: Table of the hopping parameters between the two planes of graphene. The hopping parameters γ_1, γ_3 and γ_4 are represented in figure 4.10. The parameters are taken from [89].

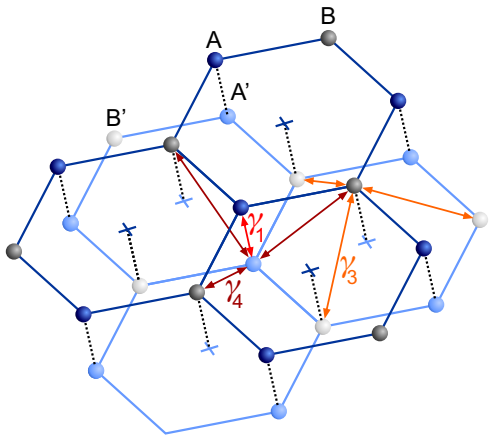

Figure 4.10: Definition of the hopping parameters between the two planes of a Bernal-stacked bilayer graphene. The darker atoms belong to the upper layer and the lighter atoms belong to the lower layer. The blue atoms form the sublattice A (resp. A') and the grey atoms form the sublattice B (resp B'). The atoms of sublattices A and A' are superposed whereas an atoms of sublattice B and B' are located in the center of a hexagonal cell of the opposite layer. The center of the hexagonal cells are marked with a cross. The model considered three hopping parameters γ_1, γ_3 and γ_4. γ_1 is defined between two neighbouring atoms of lattices A and A'. γ_3 is defined between the closest atoms of sublattices B and B'. γ_4 is defined between the closest atoms of sublattices A (resp. A') and B' (resp. B). Inspired from [89]

chapter 5

Results and discussions

This chapter presents the results associated with the two models developed previously. The first is the Ewald potential model of section 4.4, and the second is the complete tight-binding model of section 4.5. This last model has been developed for both mono-layer graphene on hBN (section 4.5.2) and bilayer graphene on hBN (section 4.5.4). For each model, electronic properties are illustrated with the band structure (BS) and the density of states (DOS). The method used to calculate DOS is developed in section C.3 of appendix C. The main structure of Hofstadter's butterfly is also presented for the complete TB model.

Due to the large number of atoms and the size of the matrices to diagonalize, the number of values of the magnetic field used to build Hofstadter's butterfly must be limited. Indeed, values of $\alpha < 1$ are needed to prospect the internal structure of the butterfly. It requires the formation of *super-supercell*, as explained at the end of section 4.3.3, that still increases the number of atoms.

5.1 Electronic properties for the Ewald potential model

This section presents the results obtained with the Ewald potential of section 4.4. First, the BS and the DOS are studied. Then, several conclusions are drawn, based on the potential strength and its effect on the electronic properties of graphene.

As discussed in section 4.4.1, the Ewald potential amplitude is determined manually. The potential is first normalized and then multiplied by amplitude A. The effect of amplitude A on the band structure is shown in figure 5.1, and the effect on the DOS is shown in figure 5.2.

As detailed theoretically in section 2.1.2, the presence of a weak potential opens gaps in the BS at the borders of the Brillouin zone and at the crossing of two bands. This is perfectly illustrated in figure 5.1. Figure 5.1a presents the BS of graphene under a potential of amplitude $A = 0.08$ eV. It can be compared with figure 5.1b with no potential and consequently no gap, and figure 5.1c obtained with an amplitude $A = 0.16$ eV.

Figure 5.2 shows the DOS of graphene determined in the same system from the BS, as explained in section C.3 of appendix C. The opening of gaps in figure 5.1 leads to the appearance of two dips, located around ± 0.2 eV. It correctly matches the experimental observations of section 3.3 where it is concluded that the dips are the signature of the hBN potential.

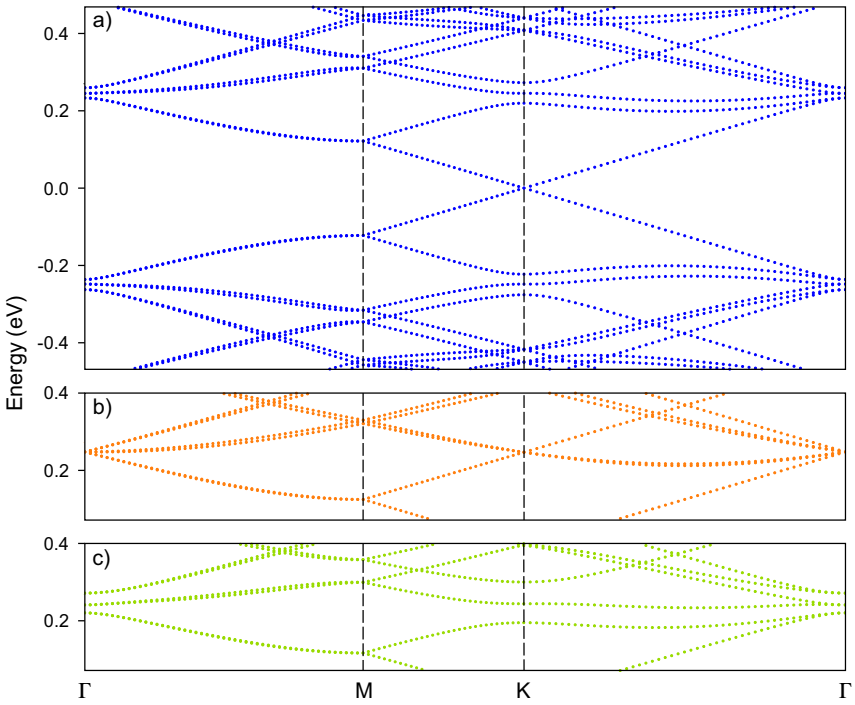

Figure 5.1: Band structure (BS) of graphene under a $1/r$ potential that represents the hBN substrate effect. BS is plotted for different values of potential amplitude A in a moiré lattice described by $\theta = 0.65°$ and $\epsilon = 0.018$. **(a)** BS obtained with an amplitude of the periodic potential equal to $A = 0.08$ eV. Gaps are clearly visible at the borders of the Brillouin zone and at the crossing of the bands. **(b)** BS of graphene without potential (free graphene). Logically, no gap is observed. This band structure is exactly the same as figure 1.4a, with the difference that it has been subject to a spectral wrapping due to the definition of the supercell. **(c)** BS of graphene under a potential of amplitude $A = 0.16$ eV. The BS behaves like in figure (a) but with wider gaps due to a higher potential.

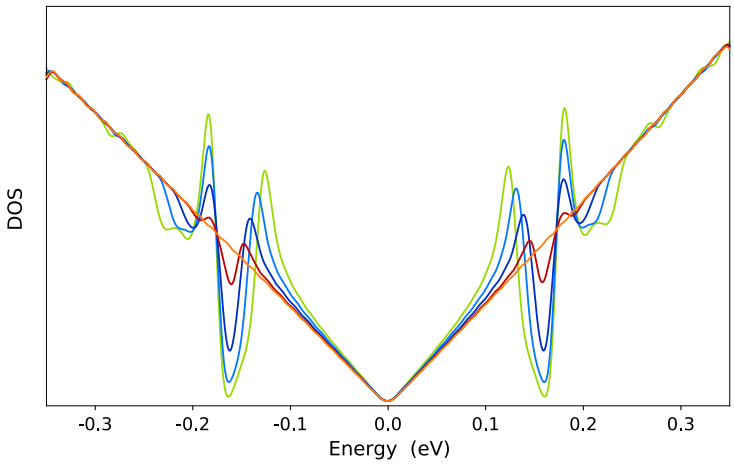

Figure 5.2: The DOS is plotted for different values of potential amplitude A in a moiré lattice described by $\theta = 0.65°$ and $\epsilon = 0.018$. The amplitudes are $A = \{0.00, 0.04, 0.08, 0.12, 0.16\}$ eV, and the corresponding DOS are given in the same order from the orange to the green curves. Dips appear in the DOS at energies around ± 0.2 eV. These dips are coherent with the experimental data of figures 3.13a and 3.18a. Value zero of the DOS is located at the lowest point of the curve at energy 0. The position of the dips and their opening are coherent with the BS of figure 5.1

The dips that appear in the valence and conduction bands in figure 5.2 are symmetric for each amplitude A. This is not coherent with experimental results. Indeed, figures 3.3a and 3.18a clearly highlight an asymmetry between the dips in the valence and conduction bands. As discussed in section 4.4, the potential model is too basic and fails to report on all interactions between graphene and hBN. However, the presence of the dips guarantees that the symmetry breaking of the graphene lattice, due to the hBN

potential, is well established. It is indispensable in order to observe Hofstadter's butterfly at low magnetic field.

5.2 Electronic properties for the complete tight-binding model

This section presents the results obtained with the complete tight-binding model of section 4.5. First, the BS and the DOS are presented for a single graphene layer and compared with the experiment and other theoretical studies. Then, the influence of different geometrical parameters on the electronic properties of graphene is discussed. Finally, the DOS of bilayer graphene (BLG) on hBN is presented and compared to that of a single graphene layer.

5.2.1 Band structure and density of states

In this section, the moiré supercell used to study the electronic properties of the moiré lattice is defined by a mismatch parameter $\epsilon = 0.0183$ and a angle $\theta = 0.67°$. These values give a moiré periodicity of $L = 11.5$ nm. This value is realistic and similar moiré periodicities have been used to highlight Hofstadter's butterfly in graphene (see section 3.3). These value lead to a supercell composed of 8608 atoms!

BS for the complete TB model is shown in figure 5.3. As for the potential model of the previous section, gaps appear at the borders of the Brillouin zone and at the crossing of two bands. However, the situation is no more the same as the symmetry between the valence and conduction bands is broken. As shown with the grey zone in figure 5.3, a large gap opens in the valence band, whereas the gaps in the conduction band are far less marked. This result is coherent with previous theoretical studies that clearly highlight the same behaviour of the BS [22, 24]. One other interesting feature of this BS is the behaviour around the K point. First, the appearance of a gap is observed; a zoom on this gap is shown in figure 5.4. Then, the BS can be compared with the energy dispersion of free graphene, shown by red lines in figure 5.3. The slope of graphene on an hBN substrate is lower than for free graphene. It indicates that the Fermi velocity of Dirac fermions is lowered by the hBN substrate, as expressed in section 1.2.3 by equation 1.43.

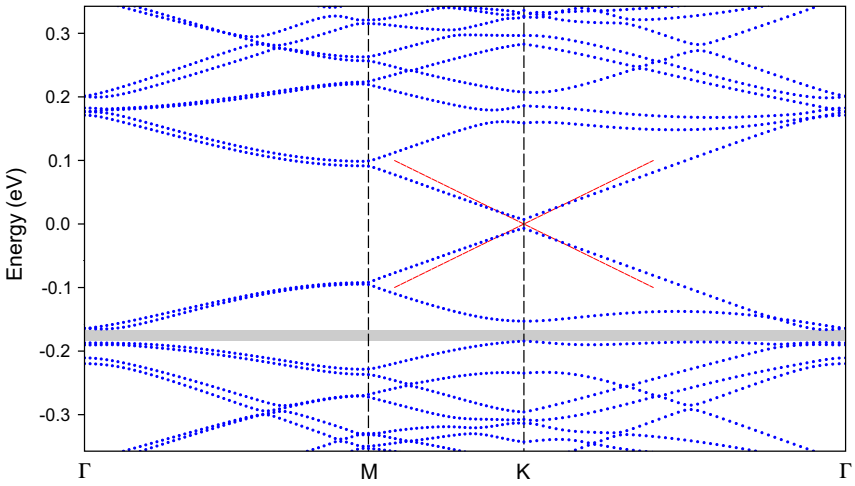

Figure 5.3: BS obtained for the complete TB model. As for the potential model of figure 5.1, gaps open at the borders of the Brillouin zone and at the crossing of two bands. However, the situation is no more symmetric between the valence and conduction bands. Gaps in valence band are wider than in conduction band. The grey zone indicates a large gap without any state located in it. The presence of a gap at the K point is also highlighted; a zoom of this gap is represented in figure 5.4. Red lines show energy dispersion around the K point for free graphene (taken from figure 5.1b).

In figure 5.3, the observation of a gap at the K point is clearly observed. Figure 5.4 is a zoom on this gap. The width of the gap is 0.014 eV. This value is very satisfactory as it is consistent with results reported by Slawinska *et al.* [28] and by Jung *et al.* in their paper *Origin of band gaps in graphene on hexagonal*

boron nitride [24]. In this last paper, the band gap is evaluated at 1 meV for non relaxed graphene on hBN, at 7 meV for relaxed graphene on hBN, and at 20 meV when the electron-electron interactions are taken into account in relaxed graphene. In my thesis, graphene is not relaxed as hypothesised in section 4.1.1. However, the complete TB model is based on DFT calculations where the functionals (see section A.3, appendix A), used to determine the hopping parameters between graphene and hBN, consider the electron-electron interactions. When considering electron-electron interactions but neglecting relaxation, it is logical to obtain a gap of around $20 - 7 \approx 14$ meV.

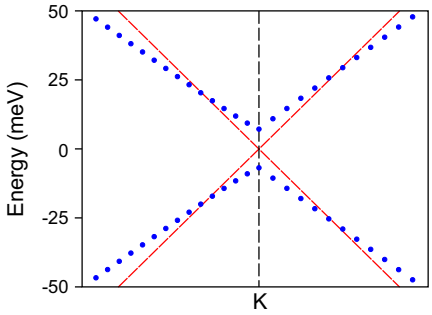

Figure 5.4: Zoom on the gap of figure 5.3 around the *K* point. The gap has a value of 14 meV. The red lines indicate the energy dispersion of free graphene.

The DOS can be determined from the BS of figure 5.3. As for the potential model, two dips appear around ± 0.2 eV. They are the signature of the effect of hBN on graphene. Due to the asymmetry of the BS, one can expect to see an asymmetry in the DOS too. This asymmetry is observed with the dips. The dip is more marked in the valence band than in the conduction band. The dip in the valence band corresponds to the absence of energy state in the grey zone of figure 5.3. Similar DOS have been obtained in other theoretical studies [24]. However, the dips asymmetry between the dips is generally much more marked in the literature.

The signature of the dips is also reported in experimental works [16, 19]. In these works, a perturbation in electronic properties is observed when doping graphene with holes or with electrons, as depicted in figures 3.13a and 3.18a. In this last figure, the resistivity exhibits two peaks. The first situated in the valence band and the second situated symmetrically in the conduction band. The peak in the valence band is much more taller than that in the conduction band. This is totally coherent with the presence of a larger dip in the valence band. Indeed, electronic density in the dip drops, leading to a larger resistivity.

The major difference between the potential model and the complete TB model is the asymmetry that appears in the second model. This asymmetry is due the construction of the complete TB Hamiltonian. As discussed below, the interlayer hopping parameters γ^{CB} and γ^{CN} breaks the symmetry of graphene. In the potential model, the potential due to hBN do not break any symmetry in the graphene Hamiltonian.

As a last comment, reference [19] deduces from figure 3.18a that the behaviour of resistivity is a clear signature of secondary non-gapped Dirac points due to the presence of long-wavelength hBN potential. The results of figure 5.5 suggest that secondary Dirac points are actually gapped, leading to the emergence of non-zero-mass Dirac fermions at the border of the Brillouin zone. The results of this work are coherent with the theoretical results found in [22] and [23]. Further work is needed to reconcile theory and experiment.

5.2.2 Effect of different parameters on the electronic propreties of graphene

This section presents the effects of different parameters on the electronic properties of graphene. The first studied parameter is the angle θ. The magnitudes of the interlayer hopping parameters such as the on-site parameter of hBN are changed to observe their influence on the electronic properties of graphene. Finally, the influence of hBN is described when the second and third neighbours in the TB model of graphene are neglected.

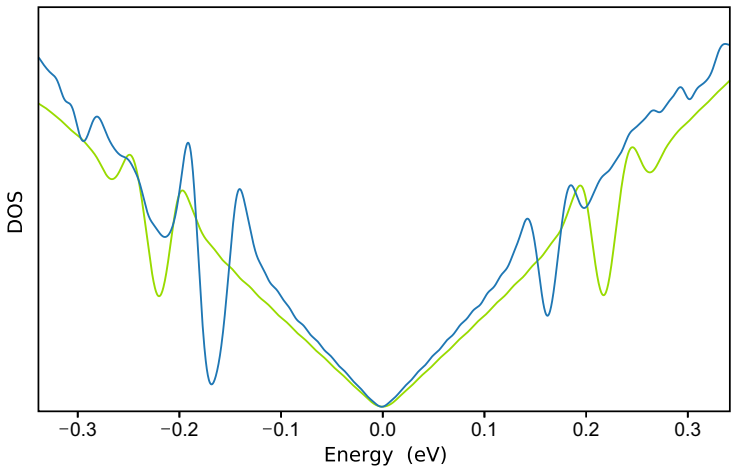

Figure 5.5: Density of state (DOS) of graphene placed on top of hBN. The blue curve represents the DOS of graphene in the complete TB model. Two dips appear around ± 0.2 eV and are the signature of the symmetry breaking provoked by the hBN substrate. The dip in the valence band is much greater than the one in the conduction band. This is coherent with figure 5.3 where a wider gap is present in the valence band (highlighted by the grey zone). The location of the dips is coherent with the position of the gaps at the border of the Brillouin zone in figure 5.3. The green curve represents the DOS of the potential model in figure 5.2 for amplitude $A = 0.08$ eV. Values zero of the DOS are located at the minimum of the curves at the energy 0.

Effect of the angle θ

As explained in section 4.2.2, a commensurate lattice of graphene on hBN is built with two initial parameters, the lattice mismatch coefficient ϵ and angle θ between the lattices of graphene and hBN. Theoretically, coefficient ϵ must remain close to the value 0.018 that corresponds to the mismatch between two free layers of graphene and hBN. An excessive increase of this parameter would lead to a sharp rise in the strain energy of the graphene layer, which is not possible spontaneously in real systems. However, in order to reduce the number of atoms in the supercell and therefore to reduce the computation time, a mismatch parameter $\epsilon = 0.028$ has been used to study the effect of angle θ.

In real systems, angle θ can be modulated on a wide range of values. The choice of θ determines the wavelength of the superlattice. Experimental data reports a wavelength that goes from 2.4 nm to 15.5 nm [16, 19]. One can then ask what is the effect of this angle on the electronic properties of graphene. The DOS of graphene is plotted for different values of θ in figure 5.6.

Looking at figure 5.6 gives interesting results. At small values of θ, the asymmetry of the gap between electrons and holes sides is strong. However, this asymmetry tends to disappear when increasing the angle. In other words, reducing the moiré wavelength decreases the asymmetry of the DOS. With an increase of the angle, the DOS behaves more and more like in figure 5.2, where only an effective potential is applied. It tends to indicate that the influence of the interlayer hopping parameters, at the origin of the asymmetry in the DOS, is less and less important when the superlattice wavelength is decreased. **further discussions?**

Effect of the interlayer parameters

The interlayer hopping parameters γ^{CB} and γ^{CN} are at the origin of the interaction between graphene and hBN in the complete TB model. Without these parameters, the graphene layer and the hBN layer would be totally independant. The effect of their magnitude on the electronic properties of graphene are shown in figure 5.7. More the magnitude of the interlayer parameters is important, more the dips in the DOS are large. These parameters have therefore a predominant role in the effective potential caused by hBN on the graphene layer.

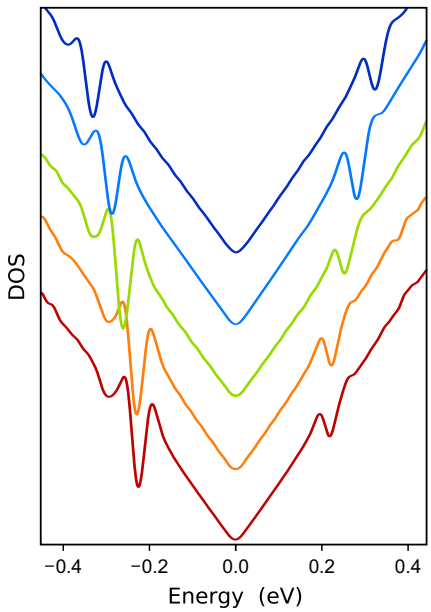

Figure 5.6: Effect of angle θ on the DOS for a moiré system described by $\epsilon = 0.028$. The angles are $\theta = \{0°, 0.8°, 1.6°, 2.4°, 3.2°\}$ and the corresponding moiré wavelength are $L = \{8.76\text{ nm}, 7.60\text{ nm}, 5.90\text{ nm}, 4.75\text{ nm}, 3.78\text{ nm}\}$. The DOS are given in the same order as the angles from the red curve ($\theta = 0°$) to the blue curve ($\theta = 3.2°$). Asymmetry between the two dips is reduced when increasing θ. For clarity, the DOS are shifted vertically. Zero values of DOS are always located at the minimum of the curves, at energy 0.

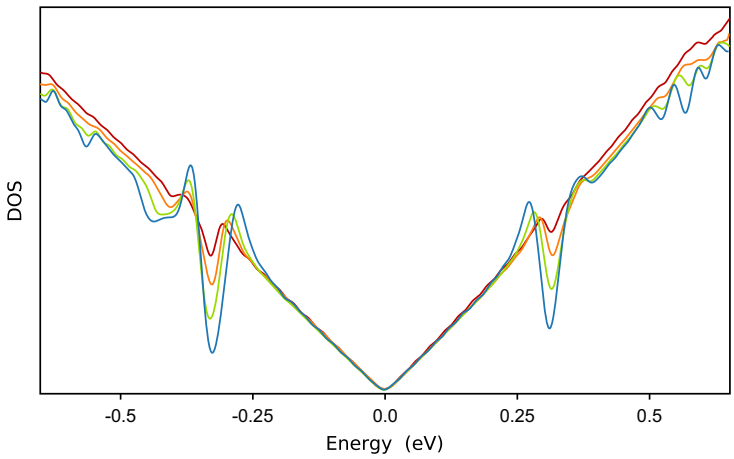

Figure 5.7: Influence of the interlayer hopping parameters magnitude on the electronic properties of graphene for a moiré lattice described by $\theta = 0.95°$ and $\epsilon = 0.03$. The absolute values of the parameter γ_0 defined in table 4.2 are $\{0.8, 1.0, 1.2, 1.4\}$ eV. The corresponding curves follow the same order from red to blue.

Effect of the on-site parameters of hBN

The influence of the on-site parameters magnitude, associated to boron and nitrogen, is studied here. As seen in section 4.5.2, they on-site parameters are represented respectively by Δ^{B} and Δ^{N}. Figure 5.8 shows the results associated to a variation of the magnitude of these on-site parameters. A stricking observation concerns the significant variation of the dips size in the conduction band whereas the dips remains mainly the same in the valence band. The conclusion is that the gap that causes the dips in the valence (see figures 5.3 and 5.5) band is mostly due to the interlayer hopping parameters. This hypothesis is supported by the discussion that closes this section.

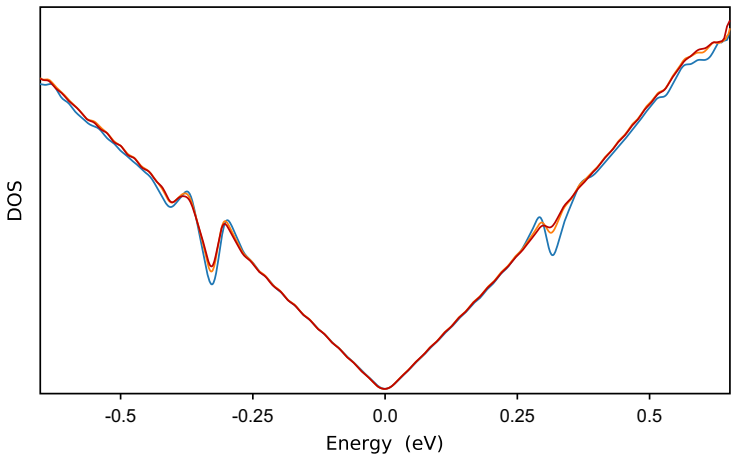

Figure 5.8: Influence of the on-site parameters magnitude of hBN on the electronic properties of graphene for a moiré lattice described by $\theta = 0.95°$ and $\epsilon = 0.03$. The values Δ^{B} and Δ^{N} have been multiply by the factors $\{0.6, 0.8, 1.0, 1.2\}$. The corresponding curves follow the same order from red to blue. The effect of the variation of the on-site term is essentially visible in the conduction band.

Effect of the second and third neighbours

As discussed in section 1.3.1, the hopping parameters of the second and third nearest-neighbours are at the origin of the asymmetry of the band structure between the valence and the conduction bands. One can then make the assumption that the assymetry between the dips in the valence and conduction bands are due to the asymmetry of the bands themselves. In figure 5.9, the BS and the DOS are shown by ignoring the influence of the second and third nearest neighbours. Valence and conduction bands are therefore totally symmetric. To push the symmetry further, the on-site parameters are also defined symmetric such that $\Delta^{B} = -\Delta^{N} = 2.35$ eV. However, despite the symmetry of the system, the dip in the valence band is again greater that the dip in the conduction band.

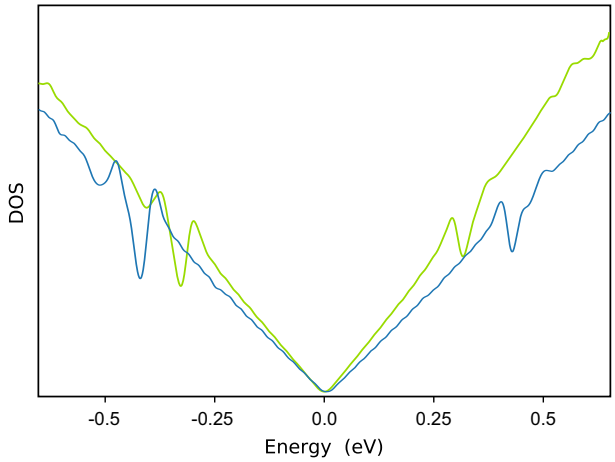

Figure 5.9: DOS of graphene on hBN by considering only the nearest neighbours in the graphene layer and by imposing a $\Delta^{B} = -\Delta^{N}$. As illustrated in figure 1.5, the DOS of free graphene in the nearest neighbour approximation is totally symmetric. However, when adding hBN, the dip in the valence band is larger than the dip in the conduction band. It indicates that the interlayer parameters are at the origin of the symmetry breaking.

As a conclusion of this section, the interlayer hopping parameters γ^{CB} and γ^{CN} are at the origin of the asymmetry between the dips in the valence and conduction bands.

5.2.3 Bilayer graphene on hBN

When two layers of graphene are stacked to form bilayer graphene, their energy dispersion is no linear anymore, as it would be the case for single graphene (see section 1.2.1) [8, 92]. It implies that Dirac fermions acquire a mass near the *K*-point due to the curvature of the band structure. The origin of this change in the band structure of the two graphene layers comes from the interlayer hopping parameters introduced in the model of section 4.5.4. The BS and the DOS of bilayer graphene obtained with this model are shown in 5.10. The effect of a constant potential imposed between the two layers of graphene is also depicted in this figure.

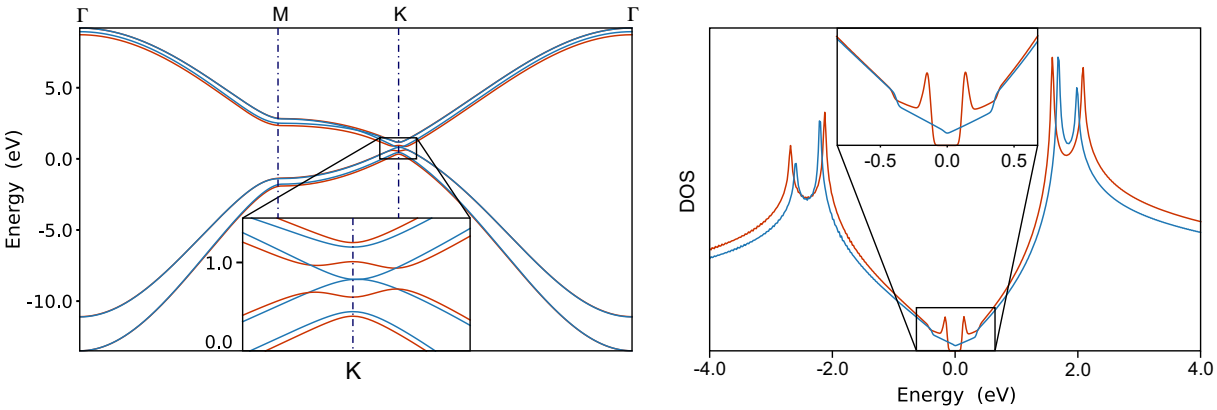

Figure 5.10: Band structure (BS) and density of state (DOS) of bilayer graphene (BLG). A potential difference ΔV between the two layers of graphene modifies the electronic properties of BLG. Blue curves show the case without potential ($\Delta V = 0$ eV and red curves show the case with a potential $\Delta V = 0.2$ eV. **(a)** BS of BLG. The two lower curves correspond to the valence bands and the upper curves correspond to the conduction bands. The inset zooms on the BS around the K point. The potential opens a gap between the valence and the conduction bands. **(b)** DOS of BLG. The inset zooms on the DOS around the Fermi energy (energy 0). The gap shown in figure (a) is also highlighted in the DOS.

The electronic properties of bilayer graphene presented in figure 5.10 are coherent with the literature [8, 92] and therefore constitutes a good starting point to observe the effect of hBN.

As for single graphene, BLG forms a moiré lattice when placed on hBN (see section 3.3.2). The supercell used for BLG is the same as that of single graphene described in section 5.2.1, with a moiré periodicity $L = 11.5$ nm. The only deference being the second graphene layer placed on top of the initial system in a Bernal-stacked configuration as described in the model of section 4.5.4.

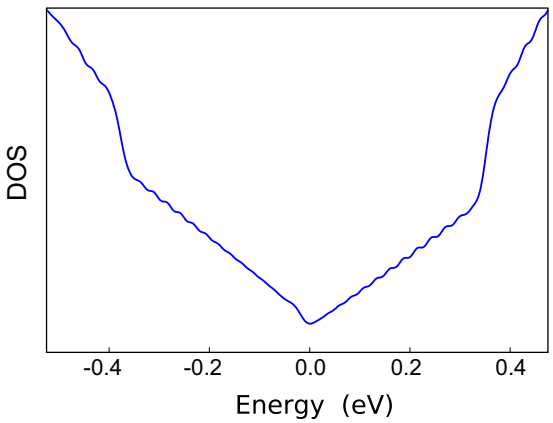

Figure 5.11: DOS of BLG computed around the energy zero. The DOS is extremely similar the DOS of free BLG in figure 5.10b. As for single graphene on hBN, the apparition of gaps at energies close to ± 0.2 eV is expected. It does not appear in this graph. A more complete model is therefore necessary to properly represent the electronic properties of BLG placed on hBN.

The DOS plotted for BLG on hBN is shown in figure 5.11. Immediately, it appears that the effect of hBN is not visible in the DOS. Indeed, as for single graphene on hBN, gaps should open at the borders of the Brillouin zone, leading to the apparition of some dips in the DOS around energy zero. More work has to be performed to properly represent the interaction of hBN. An improvement of the model could be to recalculate all the hopping parameters based on DFT calculations for a complete system of BLG on hBN. This model could therefore include the interactions between hBN and the upper graphene layer.

5.3 Hofstadter's butterfly

This section presents the signature of Hofstadter's butterfly in the complete TB model the moiré lattice described in section 5.2.1 ($\epsilon = 0.0183$, $\theta = 0.67°$ and $L = 11.5$ nm). The results found in the frame of this model are discussed based on the experimental results of section 3.3.

Presentation of the results

In order to study Hofstadter's butterfly, magnetic field must have a value such as $\alpha < 1$. As described in section 4.3.3, α is given by the ratio p/q, where p is the number of magnetic flux quanta, and q is the number of unit cells in which are located the p quanta. In order to highlight the fractal-like behaviour due to the superlattice potential, q must represent the number of supercells in which are located p quanta. It is therefore necessary to construct a *super-supercell* made of q initial supercells. Each figure in this section will refer to the couple $(q,\ p)$ that gives the value of the magnetic field used.

However, the initial supercell already contains 8608 atoms. In order to construct the graph used by *SuperTB* to elaborate the TB Hamiltonian (see section C.1, appendix C), about one hour is needed by considering until the third nearest neighbours. This time goes as the square of the number of atoms. The construction of a *super-supercell* made of 9 initial supercells takes therefore about 81 hours! It imposes a limit on the value q that prevents to go deep into the internal structure of Hofstadter's butterfly. The computations have been performed for three different *super-supercells* that are therefore characterized by small values of q. The first is constructed with 4 initial supercells, the second with 5 and supercells and the last one with 7 supercells.

As discussed in chapter 3, Hofstadter's butterfly is characterized by the splitting of the Landau levels (LLs) into subbands. The subbands appear because of the effect of the periodic atomic lattice. When graphene on hBN exhibits a moiré pattern, the LLs are predicted to split at relatively low value of magnetic field, due to the presence of the superllatice potential. The splitting of the LLs constitutes a proof of the presence of Hofstadter's butterfly.

The LLs splitting is observed with this model. This is illustrated in figure 5.12 with comparison to the same *super-supercell* of graphene but without hBN. The DOS of free graphene (blue line) presents the characteristic Landau quantization that depends on the square root of the energy and presented in section 2.2.3. The DOS of graphene on hBN (red curve) matches the LLs but each LLs is split into sublevels. The splitting in the valence band is much more important than in the conduction band. This is compatible with the asymmetry observed in the DOS, in figure **??**.

Hofstadter's butterfly in a superlattice must obey to the rule of construction presented in section 3.1. That is, when $\alpha = 1$, each LL must be continuous in energy, without internal gap. This feature is observed in the DOS obtained with the model for $\alpha = 1$. This is illustrated in figure 5.14.

In figure 5.12 it was shown that the splitting of the LLs is stronger in the valence band. Figure 5.15 gives the DOS at low magnetic field. The influence the dip in the valence band in figure 5.5 is clearly visible. Its presence modifies the LLs at energies close to -0.2 eV.

Discussion of the results

The signature of Hofstadter's butterfly has been highlighted in the DOS of graphene on hBN, for different couples of values $(p,\ q)$. However, these results must be compared to experimental results.

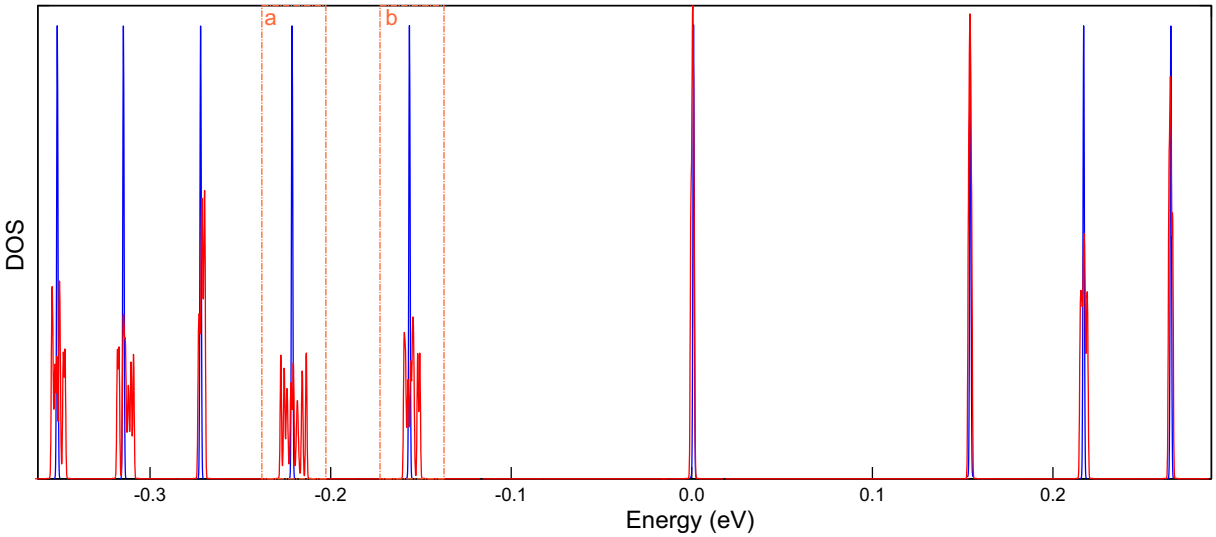

Figure 5.12: DOS computed with 5 supercells and 4 magnetic flux quanta. The blue curve shows the Landau levels (LLs) of free graphene subject to the same magnetic field. The red curve gives the DOS of graphene when considering the interactions with hBN. The LLs are split in sub-levels. This is the signature of Hofstadter's butterfly. The two orange rectangle refer to the zooms of figure 5.13. The smearing used to obtain the DOS is $\lambda = 10^{-3}$ eV (see section C.3)

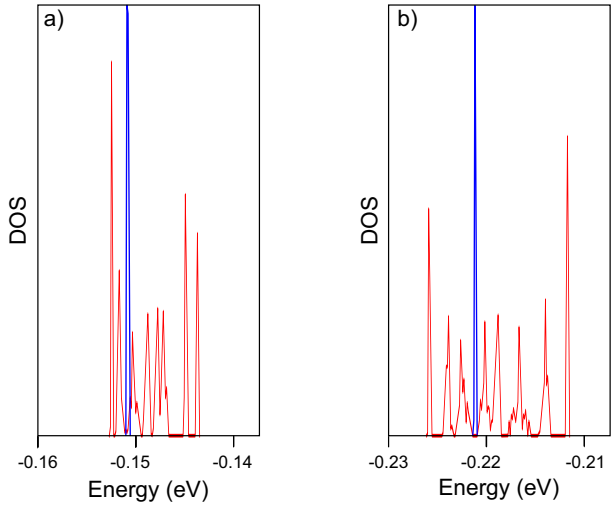

Figure 5.13: Zooms on the DOS situated in the two zones depicted in figure 5.12. These two figures highlight the substructure of each LL when graphene interacts with hBN (red curve). The smearing used to obtain the DOS is $\lambda = 10^{-4}$ eV (see section C.3)

As a first comment, the observation of a stronger splitting in the valence band is coherent with the experimental results of section 3.3.3 where the fractal behaviour is also stronger in valence band (see figures 3.19a and 3.19b as well as 3.17 for BLG). Nevertheless, the splitting in the valence band is not sufficiently important to explain the experimental results. Indeed, as explained in section 3.1.4, when the Fermi energy stands inside a gap, the conductance takes integer values of e^2/h. In order to observe variations of the conductance coherent with the butterfly's fractal-like behaviour, as it is reported in sections 3.3.2 and 3.3.3, the gaps within each LL much be large[1]. In figure 5.13 that zooms on the internal structure of a LL, the gaps appear to be too thin for really highlighting the fractal behaviour in a real system.

Another comment concerns the influence of the dips in the DOS, shown in figure **??**. As illustrated in figure 3.19, the moiré superlattice must normally induce a dip in the electronic density that is also

[1]Too narrow gaps are not visible in experimental system, because of the broadening of each energy level, caused by electrons scattering and temperature

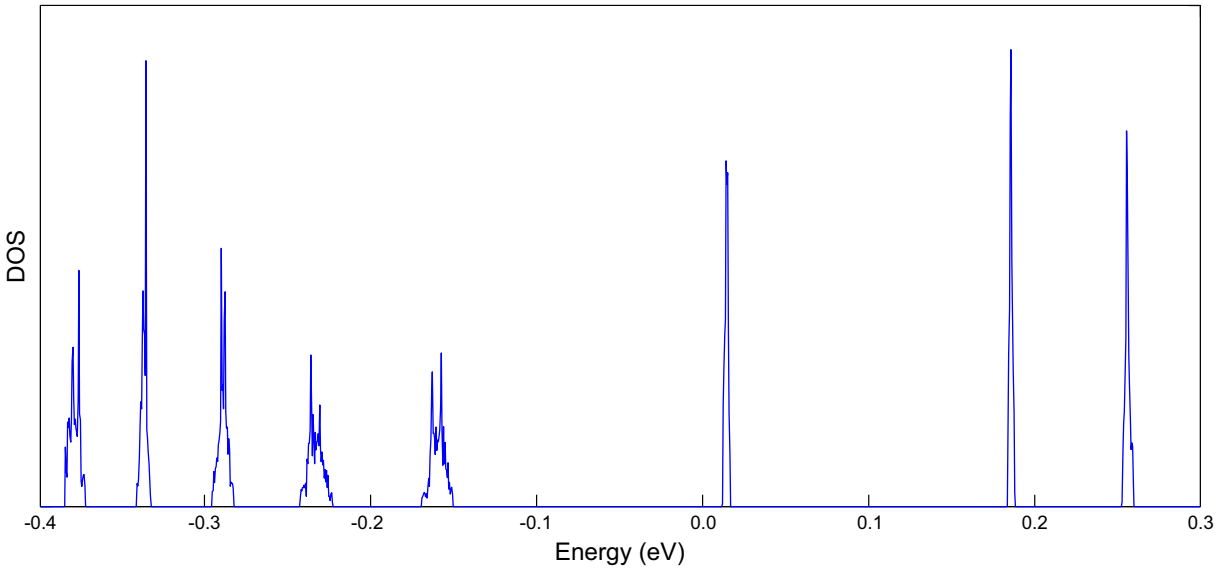

Figure 5.14: DOS computed with 4 supercells and 4 magnetic flux quanta (which is equivalent to 1 supercell and 1 quantum). As predicted by the theory, the LLs are composed of continuous energies. No gap is visible inside each LL, contrary as the LLs in figure 5.12 and **??**. The smearing used to obtain the DOS is $\lambda = 10^{-4}$ eV (see section C.3)

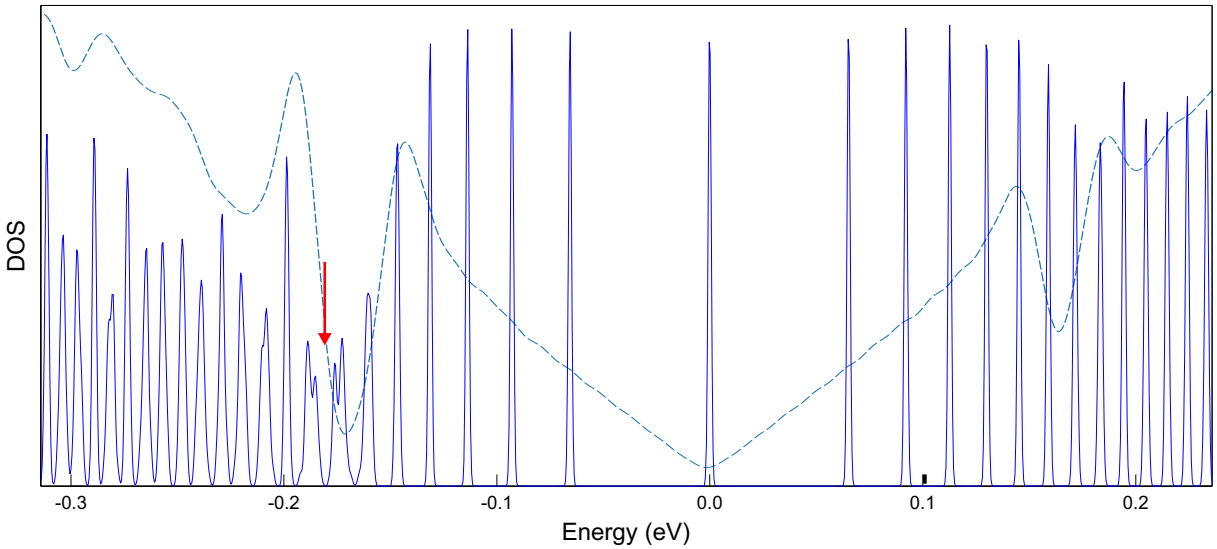

Figure 5.15: DOS computed with 7 supercells and 1 magnetic flux quantum. The presence of the gap presented in figure 5.5 is also visible at low magnetic field. Its signature is highlighted with the red arrow. At this position, the presence of the gap modifies the position of the LLs. The dotted line represents the DOS of figure **??**, found for the same system without magnetic field. The smearing used to obtain the DOS is $\lambda = 10^{-3}$ eV (see section C.3)

present at higher magnetic field. In the DOS computed in this master thesis, the presence of the dip in the valence band modifies the LLs around energies close to -0.2 but is not clearly visible at higher values of the magnetic field, as illustrated in figure 5.15 by comparing the DOS with and without magnetic field. The dip in the conduction band has almost no influence. Furthermore, the emergence of Dirac fermions at the energy of the dips must also lead to a clear Landau quantization around each dip, as illustrated in figure 3.19. Once again, this behaviour is not observed in the DOS of figures 5.12 and 5.15.

As a conclusion of this discussion, it appears that the interaction between graphene and hBN, represented in the complete TB model, is too weak to highlight with realism the behaviour of Hofstadter's butterfly observed by experiment. The influence of the dips in both the conduction and the valence band is too weak when increasing the magnetic field. With a stronger influence of the hBN substrate, the splitting of each LL would be stronger and the presence of a second Landau quantization around the dip in the valance band would lead to the appearance of larger gaps, as described in other theoretical works [19, 22].

Conclusion and perspectives

In my master thesis, I have developed two tight-binding models used to study the electronic properties of graphene placed on an hBN substrate and exhibiting a moiré pattern. The first model represents the effect of hBN on graphene as a simple potential. The focus of this model is to show that the potential is at the origin of the dips in the DOS, observed by experiments. However, it does not highlight the asymmetry between the valence and conduction bands. The second model is a complete tight-binding model that takes into account the interactions between graphene and hBN with interlayer hopping parameters. The success of this model is to properly represent the asymmetry in the electronic properties. The results obtained by this model are coherent with both experimental and other theoretical studies. However, this model shows its limitations for bilayer graphene on hBN. The effect of the moiré pattern has not been highlighted.

Based on the complete tight-binding model, I have highlighted the fractal-like behaviour of energy that appears at high magnetic field, due to the moiré superlattice. However, the signature of Hofstadter's butterfly found in this master thesis is not sufficiently strong to explain the success of the experimental observations. The conclusion is that the interaction between graphene and hBN is not sufficiently strong in the frame of this model to represent the behaviour of graphene at high magnetic field.

Appropriate final results are important to crown the work of one complete semester. But even more important are the skills and knowledge I acquired from this work. Of course, my understanding of the physical concepts used to establish the models has improved, but I also developed more general competences, for which I am extremely grateful. For instance, one year ago, I knew nothing of Python and Linux despite their importance in science. I still have much to learn, but first steps are always the more challenging and they are now behind me. Secondly, my master thesis constitutes a good introduction to the world of research. Working outside the established guidelines of traditional lectures is very formative. Finally, I have made important progress in adopting the good habits necessary when conducting simulations. I have learned much from all the irrelevant simulations and the time lost with beginner's mistakes!

This work , as explained in appendix C, has also been useful to test the limits of the code *SuperTB*. It has led to many improvements since the first version of the code, one year ago. The testing of the code constitutes a secondary achievement of my master thesis.

Based on this thesis, many perspectives can be foreseen for future work. As a first objective, a more realistic system can be developed by considering the relaxation of graphene when placed on the hBN substrate. The change in electronic properties due to the stress field could lead to interesting results.

As another perspective, other substrates for graphene can replace hBN. Recently, dichalcogenide metals, composed of two-dimensional layers stacked with Van der Waals forces, have received growing interest for use in electronic and optical applications. The use of dichalcogenide materials as substrate for graphene is also the subject of many studies [93-96]. The interest in these materials is their strong spin-orbit coupling [97]. An interesting theoretical study could concern the effect of spin-orbit coupling on Hofstadter's butterfly.

And for future work, the study of Hofstadter's butterfly in bilayer graphene on hBN could also be pertinent as it can be compared to the experimental results of reference [3]. A first model has been developed in this master thesis, but it has not been able to properly represent the effect of hBN on the electronic properties of bilayer graphene. The deeper study of the physical effects of hBN substrate on energy dispersion could also be interesting, such as explaining theoretically the asymmetry of the dips between the valance and the conduction bands.

Appendices

appendix A

Brief presentation of the DFT calculation

Density functional theory (DFT) constitutes a revolution in the world of science. It is a method used to solve numerically the Schrödinger equation with a high accuracy [98]. DFT has allowed huge progresses in material physics, in chemistry and now in biology where it allows to simulate molecules [99]. A brief introduction to the main principles of DFT is achieved in this annex.

A.1 Resolution of the Schrödinger equation

This section describes the usual approximations made in a many-body system in order to solve the Schrödinger equation. The Schrödinger equation for a system of n electrons and N nuclei can be written as[1]:

$$\hat{H}\Psi = \sum_N \sum_n \left(\frac{-\nabla^2_{n,N}}{2} + V_{n,N}(\mathbf{r}_{n,N}) \right) \Psi = E\Psi \tag{A.1}$$

The first approximation is the Born-Oppenheimer approximation. It says that, because nuclei move much more slowly than electrons, the wavefunction of electrons and nuclei are decoupled. The total wave function can written as

$$\Psi = \phi(\mathbf{r}_1, \mathbf{r}_2, ..., \mathbf{r}_n) \otimes \Theta(\mathbf{R}_1, \mathbf{R}_2, ..., \mathbf{R}_N) \tag{A.2}$$

with $\mathbf{r}_i$ are the electrons coordinates and $\mathbf{R}_j$ the nuclei coordinates. The equation A.1 can now be written for a system of n electrons as

$$\hat{H}\Psi = \sum_n \left(\frac{-\nabla^2_n}{2} + V_{ext}(\mathbf{r}_n) + \sum_{m>n} \frac{1}{|\mathbf{r}_n - \mathbf{r}_m|} \right) \phi = E\phi \tag{A.3}$$

where

- $-\nabla^2_n/2$ is the kinetic operators for the electrons. This operator is expressed with the notation

$$\hat{T}_e \equiv \sum_n \frac{-\nabla^2_n}{2}$$

- $V_{ext}(\mathbf{r}_n)$ is the external potential which, among others, contains the potential of the N nuclei.
- $\sum_{m>n} 1/|\mathbf{r}_n - \mathbf{r}_m|$ is the electron-electron interaction potential. This term is extremely problematic when solving the Schrödinger equation. Indeed, the charge of each electron is not confined in a small fixed area as the charge of nuclei. The shape of the orbitals and the dynamic interactions, as

[1] The Atomic units are used here where $\hbar = m_e = 1$

the Van der Waals interactions, make the calculation of the exact potential impossible. This potential is expressed by the notation

$$\hat{V}_{ee} = \sum_{n} \sum_{m>n} \frac{1}{|\mathbf{r}_n - \mathbf{r}_m|}$$

The difficulty is to properly solve numerically the Schrödinger equation for the wavefunction ϕ of the electrons. DFT is used to this end.

A.2 Density Functional Theory

DFT is a numerical method based on the Hohenberg-Kohn theorem [32]. This theorem says that, for a system of N_e electrons, the external potential $V_{ext}(\mathbf{r})$ is uniquely determined by the ground-state density $n(\mathbf{r})$ up to a constant. $n(\mathbf{r})$ has the expression

$$n(\mathbf{r}) = N_e \int \phi^*(\mathbf{r}_1, ..., \mathbf{r}_n)\phi(\mathbf{r}_1, ..., \mathbf{r}_n)d\mathbf{r}_1...d\mathbf{r}_n \tag{A.4}$$

The external potential is then said to be a functional of the ground-state density. A functional can be seen as a function that takes a vector in input and that gives a real number as output [98]. This explains the name *Density Functional Theory*.

In each physical system, the energy evolves to be minimized. In the Hohenberg-Kohn theory, the minimisation of the energy is computed according to the density and is expressed as

$$E = \min_{n} \left\{ F[n] + \int n(\mathbf{r}) V_{\text{ext}} d\mathbf{r} \right\} \tag{A.5}$$

Where $F[n]$ is a functional of the density expressed using the Dirac notation as

$$F[n] = \min_{\phi \to n} \left\{ \langle \phi | \, \hat{T}_e + \hat{V}_{ee} \, | \phi \rangle \right\} \tag{A.6}$$

The minimisation here is effectuated with wavefunctions that contribute to the ground-state density $n(\mathbf{r})$ [98]. However, the troublesome term $\hat{V}_{ee}$ described above comes again in the formalism.

Because $F[n]$ represents a large part of the total energy, it is critical to make approximations on it. An idea is then to subtract well-known terms from $F[n]$ in order to make approximations on a less significant part of the total energy. Kohn and Sham has developed such an approach based on a kinetic term of non-interacting electrons [100]. The use of non-interacting electrons in the kinetic term strongly reduces the complexity of the computation. They departed from the following expression

$$T_0[n] = \min_{\phi \to n} \left\{ \langle \phi | \, \hat{T}_e \, | \phi \rangle \right\} \tag{A.7}$$

They also used the Hartree energy given by the expression

$$E_H[n] = \frac{1}{2} \int \frac{n(\mathbf{r})n(\mathbf{r}')}{|\mathbf{r} - \mathbf{r}'|} d\mathbf{r} d\mathbf{r}' \tag{A.8}$$

The functional $F[n]$ of the expression A.6 can then be written as

$$F[n] = T_0[n] + E_H[n] + E_{xc}[n] \tag{A.9}$$

The term $E_{xc}[n]$ is called *exchange-correlation energy functional*. It takes into account the electron-electron interactions. In order to minimize the total energy and because all the other terms are known, $E_{xc}[n]$ must be minimized too. By using the Lagrange formalism, one can define the Kohn-Sham potential

$$V_{KS}(\mathbf{r}) = V_{\text{ext}}(\mathbf{r}) + \underbrace{\int \frac{n(\mathbf{r})}{|\mathbf{r} - \mathbf{r}'|} d\mathbf{r}'|}_{V_H} + \underbrace{\frac{\delta E_{xc}[n]}{\delta n}}_{V_{xc}} \tag{A.10}$$

where

- V_H is the Hartree potential
- V_{xc} is the exchange-correlation potential. It has to be properly approximated. Further explanations will be provided in section A.3

It now remains to solve the Schrödinger equation with this Khon-Sham potential. Thanks to the use of non-interacting electrons in the kinetic term, the Schrödinger equation is now in its very simple one-electron form. It is called the Khon-Sham equation

$$\left(\frac{-\boldsymbol{\nabla}^2}{2} + V_{KS}(\mathbf{r})\right)\phi_n^{KS} = \epsilon_n^{KS}\phi_n^{KS} \tag{A.11}$$

This equation can be solved self-consistently by using the following density

$$n(\mathbf{r}) = \sum_n \left|\phi_n^{KS}\right|^2 \tag{A.12}$$

A schematic of a typical self-consistent computation is illustrated in figure A.1. To start the calculation, a trial density $n_0(\mathbf{r})$ is needed.

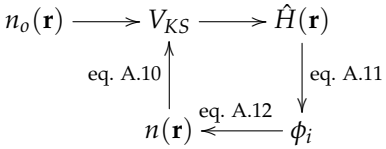

Figure A.1: Self-consistent calculation in order to determine the wavefunctions ϕ_i and the total energy $E = \sum_i \epsilon_i$

A.3 The pseudopotentials

As said in the previous section, the Khon-Sham potential contains an exchange-correlation potential (see equation A.10) that can not be known. However, it can be replaced by an approximation called *pseudopotential*. The first role of the potential is to separate the core electrons and the valence electrons in order to reduce the number of electrons that have to be taken into account in the computations. Indeed, only the valence band are considered to be able to interact and to make links with neighbouring atoms. The density becomes thus:

$$n(\mathbf{r}) = \sum_{i\in\text{core}} |\phi_i(\mathbf{r})| + \sum_{j\in\text{val.}} |\phi_j(\mathbf{r})| \tag{A.13}$$

Two main approximations are generally used in atomistic simulation:

- The Local density approximation (LDA) considers the potential to be only a function of the density

$$\hat{V}_{xc}^{LDA} = f(n(\mathbf{r})) \tag{A.14}$$

- The generalized gradients approximation (GGA) considers that the potential is also a function of the gradient of the density

$$\hat{V}_{xc}^{GGA} = f\left(n(\mathbf{r}), |\nabla n(\mathbf{r})|, \nabla^2 n(\mathbf{r})\right) \tag{A.15}$$

LDA and GGA pseudopotentials have pros and cons. One is used instead of the other depending on the situation. However, those two approximations fail to reproduce the effects of Van der Waals interactions (VdW) [84]. With the growing interest for two-dimensional VdW heterostructure [101], new pseudopotentials have been developed to represent the VdW interactions [102, 103, 104]

appendix B

A few words about the Dirac equation

The Schrödinger equation, published in 1926, has been a real revolution in physics. The wave description of the particles has led to real improvements in the understanding of the World. However, the Schrödinger equation does not respect the special relativity introduced by Einstein a few years before, in 1905. A more general description of the wave behaviour of the particles was necessary. It has been achieved by Paul Dirac in 1928 [47]. The purpose of this appendix is to give an overview of the derivation of the Dirac equation by departing from the Schrödinger equation. A particular case of the Dirac equation is treated for a massless particle. It is called the Weyl equation.

B.1 From Schrödinger to Dirac

The very well known Schrödinger equation has the form

$$\frac{-\hbar^2}{2m}\boldsymbol{\nabla}_{\mathbf{r}}^2\psi(\mathbf{r}) + V(\mathbf{r})\psi(\mathbf{r}) = -i\hbar\frac{\partial\psi(\mathbf{r})}{\partial t}$$

All the terms can be expressed in term of their operator

$$\hat{\mathbf{P}} = -i\hbar\frac{\partial\bullet}{\partial\mathbf{x}} \qquad\qquad E = -i\hbar\frac{\partial\bullet}{\partial t} \tag{B.1}$$

The Schrödinger equation then becomes

$$\frac{\hat{\mathbf{P}}^2}{2m}\psi + V\psi = E\psi$$

However, this equation does not take the special relativity into account. Indeed, the equation is not an invariant under the Lorentz transformations. The Schrödinger equation must then be transformed in order to consider equally the time and the space, as made in special relativity.

Here are some basics of special relativity. In the Einstein's theory, the energy E, the impulsion $\mathbf{p}$ and the mass m are linked in an invariant relation under the Lorentz transformations

$$\underbrace{E^2 - \mathbf{p}^2c^2}_{P^\mu P_\mu} = m^2c^4 \tag{B.2}$$

where P^μ the four-vector impulsion such that $P^\mu = (E/c, \mathbf{p})^T$ with $\mathbf{p}$ the three-vector impulsion such as $p_i = \gamma m(dx_i/dt) = \gamma m v_i$. γ is the Lorentz factor such that $\gamma = 1/\sqrt{1-(v/c)^2}$. By considering a speed

$v \ll c$, the Lorentz factor becomes $\gamma \approx 1$ and then $\mathbf{p} \approx m\mathbf{v}$. The classical expression of the energy can be obtained from this approximation. Indeed, B.2 is equivalent to

$$E = \pm c\sqrt{m^2c^2 + \mathbf{p}^2} \tag{B.3}$$

In mechanics, the sign + is the only term that has a physical meaning. Nevertheless the sign $-$ turns out to be essential in the Dirac equation. Because $\mathbf{p}^2 \approx m^2\mathbf{v}^2 \ll m^2c^2$, one can make a Taylor development such as

$$E \approx mc^2 + \frac{1}{2}m\mathbf{v}^2 \tag{B.4}$$

This expression is nothing but the classical kinetic energy $E_k = m\mathbf{v}^2/2$. The term mc^2 is the very popular rest-mass energy $E_0 = mc^2$. By replacing the operators B.1 in B.4, the Schrödinger equation is obtained, with the additional term mc^2 which gives the energy in the referential of the particle.

In order to construct a relativistic equivalent to the Schrödinger equation, it seems logical to depart from relation B.2 and to put the operators B.1 inside this expression so that, in the classical limit, it would give back the Schrödinger equation. This is the Klein-Gordon equation which is

$$-\frac{\hbar^2}{c^2}\frac{\partial^2\psi}{\partial t^2} + \hbar^2\boldsymbol{\nabla}^2\psi = m^2c^2\psi \tag{B.5}$$

where, ψ is a function of the four-vector x^μ. It is a field that depends both on time and space. By adopting the covariant notations $\partial_\mu \equiv \frac{\partial}{\partial x_\mu}$ and $x_\mu = (ct, x, y, z)$ expression B.5 becomes

$$-\hbar^2\partial^\mu\partial_\mu\psi - m^2c^2\psi = 0 \tag{B.6}$$

This equation has a good head but hides something terrible. Indeed, by departing from B.6, The term $i\psi^*$ can be applied on the left of the equation so that

$$i\hbar^2\psi^*\partial^\mu\partial_\mu\psi + i\psi^*m^2c^2\psi = 0$$

And therefore, by inverting ψ and ψ^*:

$$i\hbar^2\psi\partial^\mu\partial_\mu\psi^* + i\psi m^2c^2\psi^* = 0$$

By subtracting the first by the second equation, the following expression is obtained

$$\partial^t\underbrace{\left(i\hbar^2\left(\psi^*\partial_t\psi - \psi\partial_t\psi^*\right)\right)}_{\rho} + \partial^\mu\underbrace{\left(-i\hbar^2\left(\psi^*\partial_\mu\psi - \psi\partial_\mu\psi^*\right)\right)}_{j_\mu} = 0 \tag{B.7}$$

This expression ($\partial^t\rho - \partial^\mu j_\mu = 0$) is nothing else than the conservation law for the probability [105]. Indeed,

- ρ is the probability density
- j_μ is the probability density current

And here comes the issue. Indeed, the probability density does not guarantee to be positive. And a negative probability of presence brings some physical troubles...

It is here that Dirac enters the game. Dirac wanted to find an equation which, of course, guarantees the probability density of being positive but also which is in a first derivative degree. He then searched to find an expression that, multiplied by its conjugate, gave the Klein-Gordon equation B.6 to come back to the relativistic invariant B.4. The equation which is the candidate to have all those properties has the form [105]:

$$-i\hbar\frac{\partial\psi}{\partial t} = \left(c\boldsymbol{\alpha}\cdot(i\hbar\boldsymbol{\nabla}) + \beta mc^2\right)\psi \tag{B.8}$$

However, this equation has four combinations of $\boldsymbol{\alpha}$ and β which fulfil the conditions enunciated above. It is convenient here to define some 4×4 matrices that represent these values ($\gamma^0 \equiv \beta$ and $\gamma^i \equiv \beta\alpha^i$) so that

$$\gamma^0 = \begin{pmatrix} \mathbb{1}_2 & 0 \\ 0 & -\mathbb{1}_2 \end{pmatrix} \qquad \gamma^i = \begin{pmatrix} 0 & \sigma^i \\ -\sigma^i & 0 \end{pmatrix}$$

with $i = x, y, z$ and σ^i the Pauli matrices expressed as

$$\sigma^x = \begin{pmatrix} 0 & 1 \\ 1 & 0 \end{pmatrix} \qquad \sigma^y = \begin{pmatrix} 0 & -i \\ i & 0 \end{pmatrix} \qquad \sigma^z = \begin{pmatrix} 1 & 0 \\ 0 & -1 \end{pmatrix}$$

With those definitions, the Dirac equation can be expressed in the covariant form

$$-i\hbar\gamma^\mu\partial_\mu\psi - mc\psi = 0 \tag{B.9}$$

Here ψ is a vector carrying four components $\psi = (\psi_1, \psi_2, \psi_3, \psi_4)^T$. It is called a *spinor* because the two upper (resp. lower) components ψ_1, ψ_2 (resp. ψ_3, ψ_4) are eigenstates of the Pauli matrices. The Dirac equation then gives a formal description of the spin

$$|\psi_1\rangle = |\phi\rangle \otimes |\uparrow\rangle \qquad |\psi_2\rangle = |\phi\rangle \otimes |\downarrow\rangle$$

But the Dirac equation hides something even more extraordinary. It predicts the anti-particles! Indeed, in the particle referential, ψ_1 and ψ_2 are associated to a positive energy and ψ_3 and ψ_4 to a negative one. It directly comes from equation B.3 which gives a positive and a negative value for E. However it can be seen in another way. By considering the field ψ for both a free particle (E) and a free antiparticle ($-E$):

$$\psi_{1,2} \sim \exp\left(-i\frac{E}{\hbar}t\right) \qquad \psi_{3,4} \sim \exp\left(i\frac{E}{\hbar}t\right)$$

One can see that the antiparticle is similar to a particle of positive energy E but which goes back in the time... To meditate.

B.2 The Weyl equation in two dimensions

The Weyl equation describes the Dirac equation for a massless fermion. The Dirac equation B.9 becomes:

$$-i\hbar\gamma^\mu\partial_\mu\psi = 0$$

In this equation, one can observe that the two upper components of the spinor ψ and the two lower respond perfectly to the same relation. The two lower equations are simply the upper ones multiplied by -1. The Dirac equation can be simplified as

$$-i\hbar\mathbb{1}_2\partial_t\psi + i\hbar\sigma^i\partial_i\psi = 0$$

In two dimensions (in the plane $x - y$), the terms for $\mu = z$ vanishes. By remembering the relation between the energy and its associate operator, $E = -i\hbar\partial/\partial t$, the Weyl equation becomes

$$-i\hbar c\boldsymbol{\sigma} \cdot \boldsymbol{\nabla}\psi = E\psi \tag{B.10}$$

where $\boldsymbol{\sigma} = (\sigma_x, \sigma_y)$. The factor c comes from $\partial_t \equiv \frac{\partial}{\partial x_0} = \frac{1}{c}\frac{\partial}{\partial t}$ where x_0 is the first component of the four-vector position $x_\mu = (ct, x, y, z)$

appendix C

Implementation of the Tight-binding model

This appendix presents some informations about the implementation of the tight-binding (TB) model used for this work. First, the code *superTB* will be presented. Then, the method used to extract the TB parameters from DFT calculations will be discussed.

C.1 The code *SuperTB*

SuperTB is a program build in Python™by Simon Dubois **add ref?** at UCL in the NAPS group. The first goal of the program is to fit the Slater Koster (SK) parameters, presented in section 1.1.2, on DFT calculations, presented in appendix A. This is achieved by adjusting the SK parameters to adjust the TB band structure on the DFT band structure. *SuperTB* has been also developped to build complete TB models with functionalities as many methods of DOS calcultation **add ref?**, influence of an external potenial or the effect of magnetic field. All the TB calculation of this work were performed by using *SuperTB*.

SuperTB used many python packages to build the TB hamiltonian. It includes *Scipy*, *pymatgen*, *NetworkX*, *CoverTree* and *Pysparse*.

Scipy

Scipy is:" *a collection of open source software for scientific computing in Python, and particularly a specified set of core packages*".

from `https://www.scipy.org/about.html`

Scipy includes some widely used python packages as *NumPy*, that contains all the numerical tools essantial to make operations on matrices or *Matplotlib* that contains all the functionalities to produce graphs. Those packages are used to deal with the mathematical formalism behind the TB model and to plot the results of the computations.

Pymatgen

"Pymatgen (Python Materials Genomics) is a robust, open-source Python library for materials analysis." It contains, for example *"highly flexible classes for the representation of Element, Site, Molecule, Structure objects."*

from `http://pymatgen.org/`

Pymatgen is used to build the unit cell of the crystal that need to be studied with the tight-binding model. It constitues an easy way to arrange the atoms in the unit cell and to access all their informations (type, position, distance between the other atoms and so on).

NetworkX

NetworkX is a Python language software package for the creation, manipulation, and study of the structure, dynamics, and functions of complex networks.

from `https://networkx.github.io/`

After having creating the atomic structure with Pymatgen, it is necessary to determine, for each atom, what are its nearest neighbours, its next-nearest neighbours and so on. In *SuperTB*, this is achieved by constructing a graph with NetworkX. Each node of this graph represents an atom and all the data of this atom are associated to the node. Edges are added between each atom and its neighbours. Each edge is labelled by an *order*. If the order is 1, this is the edge between two nearest neighbours, if the order is 2, between two next-nearest neighbours and so on.

Pysparse

"Pysparse is a fast sparse matrix library for Python. It provides several sparse matrix storage formats and conversion methods. It also implements a number of iterative solvers, preconditioners, and interfaces to efficient factorization packages."

from `http://pysparse.sourceforge.net/`

Sparse matrix are matrices that are mainly composed of 0. Instead of working with $n \times m$ components, with n and m the dimensions of the matrix, it is better to only consider the non-zero components in order to reduce the computing time and to reduce the storage space. The use of sparse matrices is common in quantum computing [106, 107].

With all those packages, *SuperTB* is able to construct the hamiltonian of equation 1.8 and to find the eigenvalues of this same equation. From those eigenvalues, it is possible to plot the band structure or the DOS of the studied system.

C.2 Results of the fits on DFT band structures

As detailed in sections 1.3 and 4.5, the hopping parameters are determined with DFT calculations. The code *SuperTB* allows to extract the hopping parameters by fitting the band TB band structure on the band structure obtained with DFT.

The hopping parameters for graphene (section 1.3.1), for hBN (section 1.3.2) and for the complete system of graphene on hBN, including the interlayer interactions (section 4.5.2), were determined by Simon Dubois for the purpose of this master thesis. Here is a description of the methods used for the DFT calulation:
The first-principles calculations have been realized within the framework of the density functional theory as implement in VASP. The exchange-correlation energy is evaluated within the generalized gradient approximation using the Perdew-Burke-Ernzerhof parametrization. The wave functions are expanded using the projector augmented wave method, with a plane waves cutoff energy of 600 eV. Integration over the Brillouin zone have been performed using a $40 \times 40 \times 1$ Monkhorst-Pack k-point grid. A Fermi distribution function with a temperature of 300K has been used to populate the electronic eigenstates. Dispersion corrections have been introduced by means of the zero damping DFT-D3 method of Grimme, so as to account for the interlayer van der Waals inerations.[1]

The TB band structure have been optimized to fit correctly the DFT band structure in a energy range going from -1.5 eV to 1.5 eV**ask precisions to Simon**. This interval has been choosen because the electronic properties of graphene on hBN are obseved at low energies around the Fermi level, as discussed in section 5.2. The results of the fits of TB band structures on DFT band structures are shown for three of the six configurations of figure 4.4 in figures C.1, C.2 and C.3. These three configurations present large difference in the interlayer distance between graphene and hBN. The distance were determined with the DFT calculations and are reported in table 4.1.

[1] Informations given by Simon Dubois

Due to the interaction with hBN, the energy dispersion of graphene exhibits a gap at the *K* point. The gap is slightly underestimated in the TB band structure for the configurations of figure C.1 and C.2 but is correctly fitted in the configuration of figure C.3.

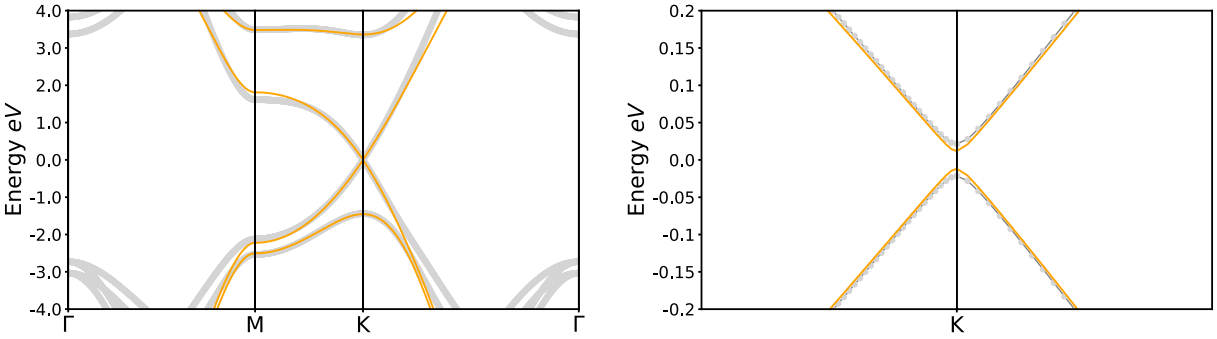

Figure C.1: Fit of the TB band structure (orange curves) on the DFT band structure (gray curves) for a system of graphene on hBN in the configuration shown in figure 4.4a. The interlayer distance found for this configuration with DFT calculation is 3.60 Å. **(a)** Representation of the band structure on the path Γ-M-K-Γ depicted in figure 1.5b. **(b)** Zoom on the band structure around the *K*-point.

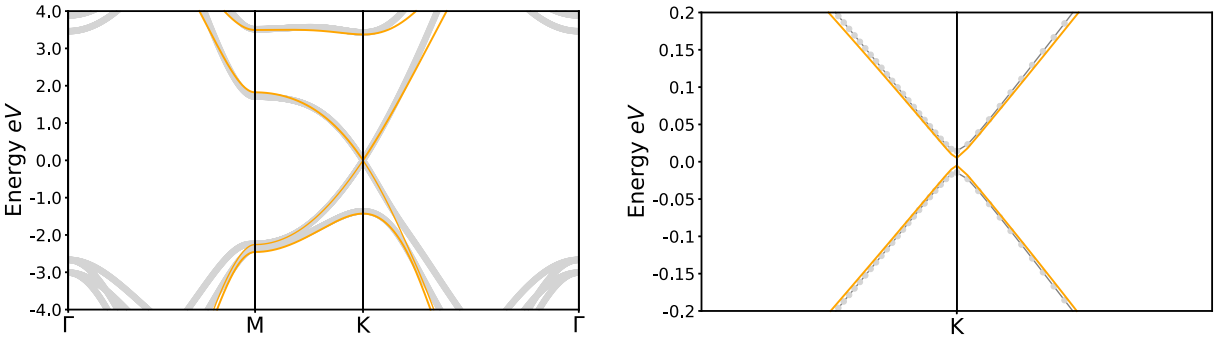

Figure C.2: Fit of the TB band structure (orange curves) on the DFT band structure (gray curves) for a system of graphene on hBN in the configuration shown in figure 4.4e. The interlayer distance found for this configuration with DFT calculation is 3.42 Å. **(a)** Representation of the band structure on the path Γ-M-K-Γ depicted in figure 1.5b. **(b)** Zoom on the band structure around the *K*-point.

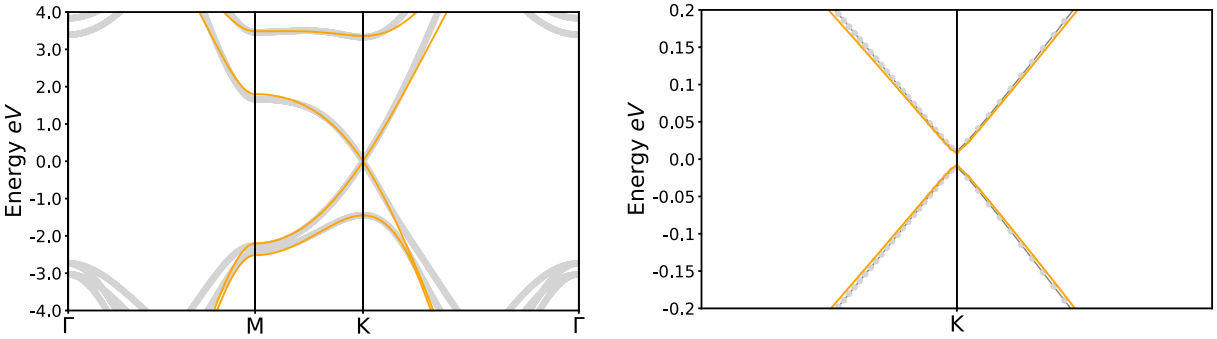

Figure C.3: Fit of the TB band structure (orange curves) on the DFT band structure (gray curves) for a system of graphene on hBN in the configuration shown in figure 4.4f. The interlayer distance found for this configuration with DFT calculation is 3.51 Å. **(a)** Representation of the band structure on the path Γ-M-K-Γ depicted in figure 1.5b. **(b)** Zoom on the band structure around the *K*-point.

C.3 Calculation of the density of state

The DOS in *SuperTB* is directly computed from the energy distribution. An homogen grid of eigenvalues is ceated in the reciprocal space and the TB Hamiltonian is diagonalised for each *k*-point of the grid. A

set of eigenvalues is therefore associated to each k-point. Each eigenvalue is then projected on the energy axis. The DOS is obtained by associating a distribution function to each eigenvalue on the energy axis. This is illustrated for a 1D example in figure C.4.

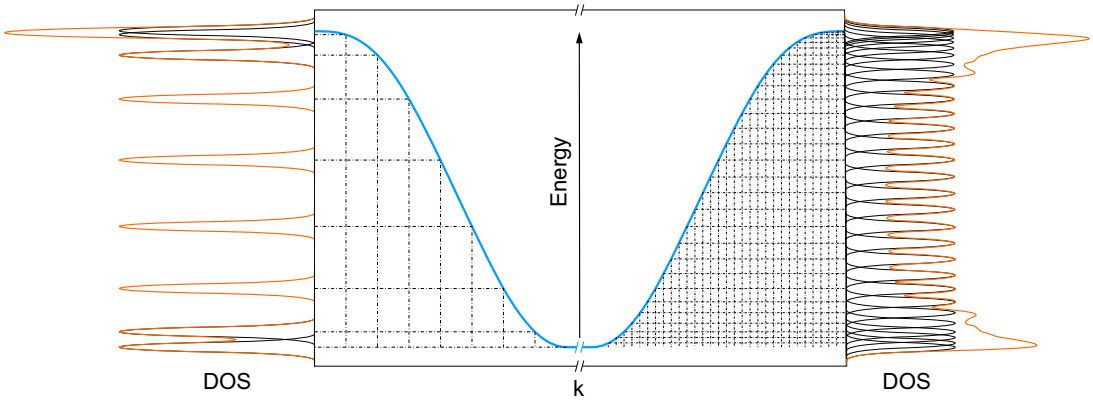

Figure C.4:

SuperTB proposes two distribution functions for the DOS calculation. In this work, a gaussian function is used. The gaussian is expressed as

$$g_i(E) = \exp\left(-\left(\frac{E - E_i}{\lambda_{\text{smear}}}\right)^2\right) \tag{C.1}$$

where E_i is the ith eigenvalue and λ_{smear} is the smearing factor that gives the opening of the gaussian. Most the number of k-points is high, most the coefficient λ_{smear} can be small, leading to a more precise definition of the DOS. The final expression of the DOS is expressed as

$$G(E) = \sum_i g_i(E) = \sum_i \exp\left(-\left(\frac{E - E_i}{\lambda_{\text{smear}}}\right)^2\right) \tag{C.2}$$

C.4 Contributions of this work to the code

I was the external user to work with *SuperTB*, besides Simon that has created the code of course. Therefore, my master thesis was the perfect occasion to test the limits of the first implementation of the code. The supercell used to represent a realistic moiré pattern contains an impressive number of atoms and, with the inclusion of the magnetic field, a stable and very efficient program is required. Some problems appeared when performing the calculations, due to the memmory needed to stock data, to the formalism used for the magnetic field, to the computation time and so. All those problems were resolved by Simon that strongly improved his code. Even if I did not make the canges to the code by myself, I think it is important to mention the improvements consequent upon my work.

The magnetic field

This part follow the discussion of section 4.3.3. In its first version, the code *SuperTB* (see annexe C.1) only allowed to set the N quanta in N distinct magnetic flux lines. A FLL was created with the N flux lines and had to be adjusted on the atomic lattice in order to be commensurate. However, it led to problems due to the integration paths for the hopping parameters, as discussed in 4.3.2. By setting a number of quanta N prime with both n_1 and n_2, it was difficult to find a shift between the atomic lattice and the FLL for which all the flux line were far from the integration path. This is illustrated in figure C.5.

These observations led to two following ameliorations of the code

- The difficulty to find a good position of the FLL in the atomic lattice, as illustrated in figure C.5, has simply been solved by setting only one flux line with N magnetic flux quanta in it. The possibility to find a appropriate shift to be far from the integration paths is directly more easy.

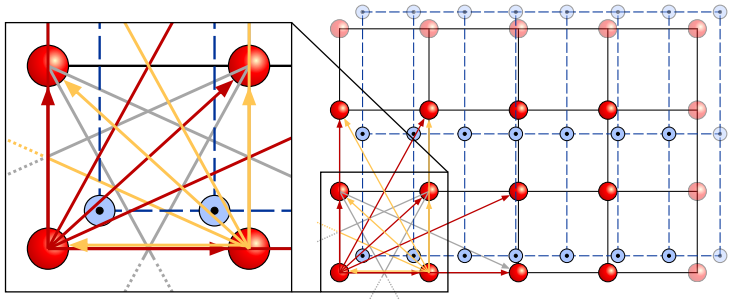

Figure C.5: Illustration of the problem linked to the choice of the location of the FLL. A supercell is constructed on the atomic lattice (the atoms are shown in red). The parameters of the supercell are $n_1 = 4$ and $n_2 = 3$ (see equation 4.19). A FLL is added in the system, with 14 flux lines in the supercell. The flux lines are shown in blue. The FLL is commensurable with the atomic lattice. The integration paths (see equation 4.16) are indicated by coloured arrows in the unit cell in the lower left corner. No flux line is allowed to be on a path (or even too close to a path) because the vector potential goes to infinity at the position of the flux line (equation 4.18). Further more, the paths of the other unit cells must also be considered for all the FLL. The good position of the FLL is then difficult to find and if there are too much paths, it can even be impossible to avoid the numerical errors due to the divergence of the vector potential. The inset shows a zoom on the first considered unit cell.

- The second amelioration directly concerns the integration paths. The integration of the vector potential in equation 4.9 does not depends on the path between atom i and j. In the first implementation of the code, the paths were defined by straight lines between two atoms, as illustrated in figure C.5. In order to free space to set the magnetic flux lines, the integration paths have been changed to follow the lattice vectors of the atomic lattice.

The memory needed to store the graph

As explained in section C.1, it is necessary to construct a graph that gives all the neighbours of each atom. This is achieved in *SuperTB* with the use of NetworkX. Due to the enormous number of atoms in the supercells (around 8000 for graphene on hBN) used in this work, the memory required to stock the graph was enormous when considering until the third nearest neighbours. Indeed, all the data related to each atom and to each interatomic link were stocked in the graph, making it too heavy.

The amelioration brought by Simon was to only give labels to each element of the graph. When *SuperTB* uses the graph, it takes the labels to access informations stocked elsewhere in the code.

Combining good precision with fast calculation

In graphene on hBN moiré lattices, the effect of hBN is visible at small energies (± 0.2 eV) around the Fermi energy in the electronic properties of graphene (see section 3.3 and 5.2). In its first version, *SuperTB* only allowed to compute all the eigenvalues of the TB Hamiltonian (typically from -6 eV to 12 eV in graphene). The number of eigenvalues of such a system is proportional to the number of atoms (still very high in a supercell) and proportional to the number of k-points. The number of k-points needed to have a precision much more higher than 0.2 eV leads to an enormous TB matrix. Because *SuperTB* computed all these eigenvalues in its first version, the calculations were too long to prospect the small desired energy range (typically from -0.5 eV to 0.5 eV).

Simon then included an option *sparse* that allow to only compute a given number of eigenvalues around a precised energy. It is implemented by the function `scipy.sparse.linalg.eigsh`. Further information on `https://docs.scipy.org/doc/scipy-0.18.1/reference/generated/scipy.sparse.linalg.eigsh.html`

appendix D

The second quantization

This appendix presents the second quantization formalism. The first section presents the passage from the first to the second quantization. Then, the formalism for the fermions and the bosons will be developed.

D.1 From the first to the second quantization

In the frame of the first quantization, each particle is described by a wave function, that are the eigenfunctions of the physical system. The physical system is described in term of operators, that act on the wave functions of the different particles. The different physical quantities, such as the energy, the position or the impulsion are given by the eigenvalues of the associated operators. Those operators are called the *observables* of the system because their eigenvalues are the results of the measurements of a real quantum system. The cornerstone of quantum mechanic is the statistical character of the measurements [59]. In the first quantization, the quantum state of a N-particles system is described by a wave function of the form

$$|\Psi\rangle = |\psi_1\rangle\,|\psi_2\rangle\cdots|\psi_N\rangle \tag{D.1}$$

The second quantization was introduced to manipulate systems of indistinguishable particles in a more practical formalism than the representation of equation D.1. The first step is to define a set of the different states $|\nu_j\rangle$ of the system: $\{|\nu_1\rangle,\ |\nu_2\rangle,\ |\nu_3\rangle,...\}$. The system of the expression D.1 can be represented more easily in what is called the occupation number representation. The goal is to count the number of particles n_j in each states $|\nu_j\rangle$ to describe the wave function of the N-particles system [74],

$$|\Psi\rangle = |n_1, n_2, n_3, ...\rangle \qquad \text{with} \qquad \sum_j n_j = N \tag{D.2}$$

This representation suggests to define a new operator whose eigenvalue is the number of particles in one state. It is called the occupation number operator and is defined as

$$\hat{n}_j\,|n_j\rangle = n_j\,|n_j\rangle \tag{D.3}$$

In a indistinguishable system, the Pauli exclusion principle forbids to have two fermions in the same state whereas there is no limit for the bosons. The eigenvalues of the operator $\hat{n}_j$ can then take the following values

$$n_j = \begin{cases} 0, 1 & \text{for fermions} \\ 0, 1, 2, ... & \text{for bosons} \end{cases} \tag{D.4}$$

D.2 For the bosons

Based on the representation of equation D.2, two new operators can be created. They are called the annihilation operator $\hat{b}_j$ and the creation operator $\hat{b}_j^\dagger$. As their names indicate, they remove or create a boson in the state $|\nu\rangle_j$. For bosons, there is no limit for the number particles n in the a state ν_j.

The **annihilation operator** acts on the state of expression D.2 as

$$\hat{b}_j \left|...,n_{j-1},n_j,n_{j+1},...\right\rangle = b_-(n_j) \left|...,n_{j-1},n_j-1,n_{j+1},...\right\rangle \tag{D.5}$$

$$n_j = 0 \ : \ b_-(n_j) = 0 \qquad \text{and} \qquad n_j = n \ : \ b_-(n_j) = n-1$$

In the same way, the **creation operator** acts on the state of expression D.2 as

$$\hat{b}_j^\dagger \left|...,n_{j-1},n_j,n_{j+1},...\right\rangle = b_+(n_j) \left|...,n_{j-1},n_j+1,n_{j+1},...\right\rangle \tag{D.6}$$

$$n_j = 0 \ : \ b_+(n_j) = 1 \qquad \text{and} \qquad n_j = n \ : \ b_+(n_j) = n+1$$

The bosonic character of a particle is described in term of its commutations relations. For a boson,

$$[\hat{b}_j^\dagger, \hat{b}_k^\dagger] = 0 \qquad [\hat{b}_j, \hat{b}_k] = 0 \qquad [\hat{b}_j^\dagger, \hat{b}_k] = \delta_{jk} \tag{D.7}$$

With $[A,B] = AB - BA$, the anti-commutation operation.

From those definitions, each quantum state can be constructed from the ground state $|0\rangle$ by adding particles in each state with creation operators,

$$\left|...,n_i,...,n_j,...,n_k,...\right\rangle = \cdots \left(c_i^\dagger\right)^{n_i} \cdots \left(c_j^\dagger\right)^{n_j} \cdots \left(c_k^\dagger\right)^{n_k} \cdots |0\rangle \tag{D.8}$$

Those properties also allow to express the occupation number operator $\hat{n}_j$ of equation D.3 in term of annihilation and creation operators,

$$\hat{n}_j = \hat{c}_j^\dagger \hat{c}_j \tag{D.9}$$

D.3 For the fermions

For fermions, a creation and an annihilation operator can also be defined as it was made for the fermions. They are called respectively $\hat{c}_j^\dagger$ and $\hat{c}_j$. In a fermionic system, the number of particles in the state n_j can take all the integer values greater than 0.

The **annihilation operator** acts on the state of expression D.2 as

$$\hat{c}_j \left|...,n_{j-1},n_j,n_{j+1},...\right\rangle = c_-(n_j) \left|...,n_{j-1},n_j-1,n_{j+1},...\right\rangle \tag{D.10}$$

$$n_j = 0 \ : \ c_-(n_j) = 0 \qquad \text{and} \qquad n_j = 1 \ : \ c_-(n_j) = 1$$

In the same way, the **creation operator** acts on the state of expression D.2 as

$$\hat{c}_j^\dagger \left|...,n_{j-1},n_j,n_{j+1},...\right\rangle = c_+(n_j) \left|...,n_{j-1},n_j+1,n_{j+1},...\right\rangle \tag{D.11}$$

$$n_j = 0 \ : \ c_+(n_j) = 1 \qquad \text{and} \qquad n_j = 1 \ : \ c_+(n_j) = 0$$

As for the fermion, the bosonic character of a particle is described in term of its commutations relations. For a boson,

$$\{\hat{c}_j^\dagger, \hat{c}_k^\dagger\} = 0 \qquad \{\hat{c}_j, \hat{c}_k\} = 0 \qquad \{\hat{c}_j^\dagger, \hat{c}_k\} = \delta_{jk} \tag{D.12}$$

With $\{A,B\} = AB + BA$, the commutation operation.

D.4 The operators

But not only the occupation number operator can be expressed in term of $\hat{c}_j^\dagger$ and $\hat{c}_j$. This is indeed the case of all the operators [74]. Let us consider an single-particle operator $\hat{\mathcal{A}}_i = \hat{\mathcal{A}}(\mathbf{r}_i, \mathbf{p}_i)$, acting on particle i. For a N-particles system, a general operator can be constructed,

$$\hat{A} = \sum_{i=1}^{N} \hat{\mathcal{A}}_i \tag{D.13}$$

From this definition, the operator $\hat{A}$ is expressed in term of creation and annihilation operators in the second quantization theory [74],

$$\hat{A} = \sum_{\alpha,\beta} \langle \beta | \, \hat{\mathcal{A}}_{\alpha\beta} \, | \alpha \rangle \, c_\beta^\dagger c_\alpha \tag{D.14}$$

Where,

$$\langle \beta | \, \hat{\mathcal{A}}_{\alpha\beta} \, | \alpha \rangle = \int \psi_\beta^*(\mathbf{r}_i) \hat{\mathcal{A}}_i \psi_\alpha(\mathbf{r}_i) \mathrm{d}\mathbf{r}_i \tag{D.15}$$

A similar development can also be made for many-particles operators [74]

appendix E

Presentation of the codes

This chapter presents the different codes used for this work and referenced in the document.

E.1 Graphene band structure

The band structure of graphene presented in figure 1.3 has been plotted by using Matlab. The code is presented in this section.

```
b=2*pi/(sqrt(3)*a);
kx=linspace(-2,2,1000);
ky=linspace(-2,2,1000);
gamma=2.8;
gammap=0.2*gamma;
fk=2*ones(1000,1)*cos(sqrt(3)*ky*a)+4*cos((3/2)*kx*a)'*cos((sqrt(3)/2)*ky*a);
Ep=gamma*sqrt(3+fk)+gammap*fk;
Em=-gamma*sqrt(3+fk)+gammap*fk;
mesh(kx,ky,real(Ep))
hold on;
mesh(kx,ky,Em)
alpha(.4)
```

E.2 Construction of a graphene on hBN commensurate supercell

The Python code created to construct the commensurate moiré supercell of graphene placed on an hBN substrate is presented in this section. The theoretical background behind this code is developed in section 4.2.2. This section is closed by the presentation of some results confirming that the code works properly.

```
import supertb as stb
from numpy import *

"""
Definition of the general parameters of the moire superlattice. The condition of commensurability is not yet
      imposed
"""

# angle of rotation (in degrees) between the graphene and the BN lattices
angle = 0.65
theta = angle*pi/180.    # the angle is transformed in radian

# Definition of the mismatch parameter that expresses the lattice parameter of hBN as a function of the
     lattice parameter of graphene. It is defined as a_hBN = (epsiGhBN+1) a_G
epsiGhBN=0.02

# Definition of the mismatch parameter that expresses the lattice parameter of graphene as a funciton of the
      lattice parameter of hBN.
epsiprem=1/(1+epsiGhBN)-1

```

```
# Definition of the general expression of the norm of the superlattice vector, based on epsi and theta. This definition does not guarantee the commensurability of the lattice
Lprem=(1+epsiprem)/(sqrt(epsiprem**2+2*(1+epsiprem)*(1-cos(theta))))*a

# Definition of the angle of rotation between the lattice vectors of hBN and the superlattice vectors
phiprem=arctan((-sin(theta))/(1+epsiprem-cos(theta)))

"""
Definition of the lattice parameters L1 and L2 of the commensurate supercell. The hBN substrate is consider to be fixed. The graphene layer adjust itself on top of hBN to produce the commensurate lattice.

"""

# Length of the projection of the superlattice vector L1 along the axis defined by the hBN lattice vector a1
A = Lprem*cos(phiprem)

# Number of atoms situated on the length A, the transformation to an integer value of the ratio A/a is the first step towards the commensurability
n = int(A/a)

# Condition to remain as closer as possible to the initial parameters
if A-n*a < a/2.:
    n = n-1

# Definition of d and N (see theoretical backgrounds)
d = a*sqrt(3.)/2.
N = int(Lprem*sin(phiprem)/D)

ratda = d/a # ratio between value d an a that is equal for graphene and hBN

# Definition of the new values of phi and L for the commensurate lattice that depends on the parity of the number of atoms n
if N % 2 != 0:
    n = n + 1./2

phi = arctan(N/n*ratda))
L = n*a/(cos(phi))

# Determination of the value of NG (see theoretical backgrounds) so that the angle theta of the commensurate lattice is as close as possible to the initial angle thetaprem. vecnG and vecNG are to mattrices that allow to cover all the combinations of nG and NG. nG is taken such as nG = n + nsupp with 1 < nsupp < 5 and NG such as 0 <= NG <= N.
vecnG = matmul(transpose(ones(N + 1)[newaxis]), n + array(range(1,6))[newaxis])
vecNG = matmul(transpose(array(range(N +1))[newaxis]), (ones(5))[newaxis])
# find the combination (nG, NG) such as theta is as close as possible to thetaprem
FindMin = abs(phi - arctan(divide(vecNG, vecnG)*ratda) - thetaprem )
coord = unravel_index(FindMin.argmin(), FindMin.shape)

NG = coord[0]
nG = n + coord[1]+1

# Final values for the commensurate supercell
theta = phi - arctan(NG/nG*ratda))   # value of theta given by nG and NG
aG = L * cos(phi - theta)/nG         # final value of the lattice parameter of graphene aG
epsi = aG/a - 1                      # final value of the mismatch parameter

# Construction of the rotation matrices associated to the angle theta (between the graphene and hBN lattice) and phi (between the hBN lattice vector a1 and the superlattice vector L1)
R=matrix([[cos(theta),sin(theta), 0], [-sin(theta),cos(theta), 0],[0., 0., 0.]])
Phi=matrix([[cos(phi),-sin(phi), 0], [sin(phi),cos(phi), 0],[0., 0., 0.]])

# Construction of the strain matrix, that adapt the lattice of graphene to ensure the commensurability with the one of hBN
M=matrix([[1+epsi, 0, 0], [0,1+epsi, 0],[0., 0., 0.]])

"""
Construction of an object 'lattice' with the class Lattice of SuperTB that extends the class Lattice of Pymatgen
http://pymatgen.org/_modules/pymatgen/core/lattice.html

"""
lattice = stb.Lattice.from_parameters(L, L, 30., 90., 90., 60.)

""""
Construction of two lists. The first 'pos' with the positions of all the atoms located in the supercell ( defined by the object lattice) and the second 'at_list' with the type of atoms corresponding to the position of the list 'pos'.

"""

# Definition of the two lattice parameters of the unit cell of hBN
ahBN1=array([a, 0., 0.])                        # a1
ahBN2=array([a*1./2., a*sqrt(3.)/2., 0.])       # a2

# Definition of the vector delta that define the position of the atom of nitrogen in the unit cell of hBN. The boron atoms are at the corner of the unit cell
deltaN = 1./3.*ahBN1+1./3.*ahBN2
```

```
92
93  h=3.35 # interlayer distance between the plane of graphene and the plane of hBN
94
95  pos=[]        # Creation of an empty list where the positions of each atom in the supercell will be added
        aferwards
96  at_list=[]    # Creation of an empty list where the type of each atom will be added aferwards
97
98  B=0 ; N=0 ; C=0 # Set three counter to zero. They count respectively the boron, the nitrogen and the carbon
        atoms.
99
100 # Definition of a maximal number of atoms along each superlattice vectors. The code will check if each of
        those atoms stands inside the supercell
101 Nmax=4*int(L/a)
102
103 # In order to avoid the numerical errors due to atoms that are positioned just at 0., a small shift is added
        to be sure that the atoms will be taken in the unit cell. Without the shift, some atoms can miss.
104 dx_shift = 0.01 ; dy_shift = 0.01
105
106 # The position of each atoms delimited in the range -Nmax:Nmax in the two lattice direction is checked by
        using two for loops. If the position is in the supercell limits, the atom is added.
107
108 for i in range(-Nmax, Nmax):
109     for j in range(-Nmax, Nmax):
110         # Position of the atom of boron labeled by (i , j)
111         atot = i*ahBN1+j*ahBN2
112         # Rotation of that position with the angle Phi
113         arot=asarray(dot(Phi, atot)).reshape(-1)
114         # Definition of the vector delta with the rotation
115         delta = asarray(dot(Phi, deltaN)).reshape(-1)
116         # x and y components of the atom of boron
117         xhBN=arot[0] + dx_shift
118         yhBN=arot[1] + dy_shift
119         # Shift along x (L1) as a funtion to the position in y given by yhBN
120         L1=yhBN*tan(30.*pi/180.)
121
122         # Check if the boron atom is in the supercell. If yes, the atom type and pisition are added to the
        lists.
123         if 0. <= yhBN < (L*sqrt(3.)/2.) and L1 <= xhBN < (L + L1):
124             pos.append(array([xhBN, yhBN, 0]))
125             at_list.append('B')
126             B=B+1
127
128         # Defintion of the position of the nitrogen atom in the unit cell labelled by (i, j)
129         xhBNd=xhBN+delta[0]
130         yhBNd=yhBN+delta[1]
131         L1=yhBNd*tan(30.*pi/180.)
132
133         # Check if the nitrogen atom is in the supercell. If yes, the atom type and pisition are added to
        the lists.
134         if 0. <= yhBNd < (L*sqrt(3.)/2.) and L1 <= xhBNd < (L + L1):
135             pos.append(array([xhBNd, yhBNd, 0]))
136             at_list.append('N')
137             N=N+1
138
139         # Definition of the position of the first carbon atom labelled in the unit cell (i , j)
140         aG=asarray(dot(dot(R, M), array([xhBN, yhBN, 0]))).reshape(-1)
141         xG=aG[0]
142         yG=aG[1]
143         L1=yG*tan(30.*pi/180.)
144
145         # Check if the carbon atom is in the supercell. If yes, the atom type and pisition are added to the
        lists.
146         if 0. <= yG < (L*sqrt(3.)/2.) and L1 <= xG < (L + L1):
147             pos.append(array([xG, yG, h]))
148             at_list.append('C')
149             C=C+1
150
151         # Definition of the position of the second carbon atom labelled in the unit cell (i , j)
152         aGd=asarray(dot(dot(R, M), array([xhBNd, yhBNd, 0]))).reshape(-1)
153         xGd=aGd[0]
154         yGd=aGd[1]
155         L1=yGd*tan(30.*pi/180.)
156
157         # Check if the carbon atom is in the supercell. If yes, the atom type and pisition are added to the
        lists.
158         if 0. <= yGd < (L*sqrt(3.)/2.) and L1 <= xGd < (L + L1):
159             pos.append(array([xGd, yGd, h]))
160             at_list.append('C')
161             C=C+1
162
163 """
164 Construction of a 'structure' object with the class Structure of SuperTB that extends the class Structure of
        Pymatgen:
165 http://pymatgen.org/_modules/pymatgen/core/structure.html
166
167 """
168 struct = stb.Structure(lattice, at_list, pos, coords_are_cartesian=True,  validate_proximity=True)
```

```
169
170 # make a super-supercell of scal initial supercells along L1 and scal supercells along L2
171 superstruct = struct*[scal, scal, 1]
```

	init.	comm.
ϵ	0.0180	0.0183
θ	0.65°	0.67°
L [nm]	11.74	11.51
ϕ	32.78°	33.12°
a_G [nm]	0.460	0.459

	init.	comm.
ϵ	0.0180	0.0173
θ	3.45°	3.62°
L [nm]	3.95	3.79
ϕ	75.22°	76.62°
a_G [nm]	2.460	2.461

	init.	comm.
ϵ	0.0250	0.0254
θ	1.45°	1.51°
L [nm]	6.99	6.81
ϕ	46.43°	47.11°
a_G [nm]	2.442	2.443

Table E.1: Presentation of the results obtained with three sets of the initial values θ and ϵ. The first column of each table presents the initial values of θ, ϵ, L, ϕ and a_G. The the second column presents the values of the same parameters obtained with the Python code for an incommensurate lattice. In the first table, $\theta = 0.65°$ and $\epsilon = 0.018$. This value of ϵ is approximatively the mismatch parameter between two free layers of graphene and hBN. In the second table, $\theta = 3.45°$ and $\epsilon = 0.018$. In the third table, $\theta = 1.45°$ and $\epsilon = 0.025$.

E.3 Ewald potential

This section will present the implementation of the Ewald potential presented in section 4.4.1. The Ewald potential is decomposed in a short and long-range as expressed in equation 4.26. Those two terms U^L and U^S are expressed in the supporting informations of [82] by the two following expressions. The long-range term is

$$U^L(\mathbf{r}) = \frac{2}{a}\sum_{n=1}^{\infty}\sum_{m=1}^{\infty}\frac{1}{\sqrt{9n^2+3m^2}}\left[e^{2\pi/(3a)\sqrt{3n^2+m^2}|z|}\mathrm{erfc}\left(\left(\frac{2\pi\lambda}{3a}\right)\sqrt{3n^2+m^2}+\frac{|z|}{2\lambda}\right)+ e^{-2\pi/(3a)\sqrt{3n^2+m^2}|z|}\mathrm{erfc}\left(\left(\frac{2\pi\lambda}{3a}\right)\sqrt{3n^2+m^2}-\frac{|z|}{2\lambda}\right)\right]\sum_{i=1}^{4}q_i\cos\left(\frac{2\pi n(x-x_i)}{\sqrt{3}a}\right)\cos\left(\frac{2\pi m(y-y_i)}{3a}\right)+ \frac{1}{\sqrt{3}a}\sum_{m=1}^{\infty}\frac{1}{m}\left[e^{2\pi m/(3a)|z|}\mathrm{erfc}\left(\frac{2\pi m\lambda}{3a}+\frac{|z|}{2\lambda}\right)+e^{-2\pi m/(3a)|z|}\mathrm{erfc}\left(\frac{2\pi m\lambda}{3a}-\frac{|z|}{2\lambda}\right)\right]\sum_{i=1}^{4}q_i\cos\left(\frac{2\pi m(y-y_i)}{3a}\right)+ \frac{1}{3a}\sum_{n=1}^{\infty}\frac{1}{n}\left[e^{2\pi n/(3a)|z|}\mathrm{erfc}\left(\frac{2\pi n\lambda}{3a}+\frac{|z|}{2\lambda}\right)+e^{-2\pi n/(3a)|z|}\mathrm{erfc}\left(\frac{2\pi n\lambda}{3a}-\frac{|z|}{2\lambda}\right)\right]\sum_{i=1}^{4}q_i\cos\left(\frac{2\pi n(x-x_i)}{3a}\right) \quad \text{(E.1)}$$

And the short-range term is

$$U^S(\mathbf{r}) = \sum_{i=1}^{4}q_i\sum_{n=-\infty}^{\infty}\sum_{m=-\infty}^{\infty}\frac{\mathrm{erfc}\left(\sqrt{\left(x+n\sqrt{3}a-x_i\right)^2+(y+3ma-y_i)^2+z^2}/(2\lambda)\right)}{\sqrt{\left(x+n\sqrt{3}a-x_i\right)^2+(y+3ma-y_i)^2+z^2}} \quad \text{(E.2)}$$

```
1  from numpy import *
2  from scipy import special
3
4  """
5  Function that takes as argument the coordinates (xpr,ypr) of an atom and return the renormalized Ewald
       Potential at this position
6
7  """
8
9  def evaluate(xpr,ypr):
10
11     ang = pi*60./180. # Angle between the vector lattice a1 and a2 of hBN
12     a_hBN=2.504 # lattice parameter of hBN expressed in angstrom
13
14     # The two following expressions take the coordinates (xpr, ypr) and give the label of the unit cell of
        hBN in which they are located. lattice
15     Nx=int((xpr - ypr/tan(ang))/a_hBN)
```

```
16      Ny=int(ypr/(a_hBN*sin(ang)))
17
18      # The two following expressions take the coordinates (xpr, ypr) located in the unit cell labelled by (Nx
         ,Ny) and give the correspondant coordinates (x,y) in the first unit cell of hBN. Indeed, the potential
         has the same periodicity as the hBN
19      y=ypr-(Ny*a_hBN*sin(ang))
20      x=xpr-(Nx*a_hBN+Ny*a_hBN*cos(ang))
21
22      a=1.445685 # interatomic distance of hBN (in angstrom)
23      # The unit cell of hBN is a rectangle of height sqrt(3)*a_hBN and width a_hBN. The four following
         expressions give the positions of the atoms in the unit cell. a1 and a3 acount for boron whereas a2 and
          a4 account for nitrogen.
24      a1=a*matrix([[0., 0.]])
25      a2=a*matrix([[0., 1.]])
26      a3=a/2*matrix([[sqrt(3.), 3.]])
27      a4=a/2*matrix([[sqrt(3.), 5.]])
28      ra=concatenate((a1.T, a2.T, a3.T, a4.T), axis=1)
29
30      # interlayer distance
31      dist=3.35
32
33      y=y+a # Shift along y in order to ajust the graphene unit cell on the square h-BN unit cell used to
         build the potential
34
35      N=4 # number of layers of neighboring cells considered to build the potential
36
37      param=20. # cuting parameter lambda that defines the limit between the long range potential and the
         short range potential. This parameter has been found by converging the potential
38
39      # the following lines allow to compute the Ewald potential using the tools of numpy and scipy in an
         efficient way, by avoiding the for loops.
40      n=matrix(ones((N,1))*arange(1,N+1))
41      m=matrix(swapaxes(matrix(arange(1,N+1)),0,1)*ones((1,N)))
42      V_L=zeros((N,N))
43
44      n2=ones((2*N+1,1))*arange(-N,N+1)
45      m2=swapaxes(matrix(arange(-N,N+1)),0,1)*ones((1,2*N+1))
46      V_S=zeros((2*N+1,2*N+1))
47
48      lambd=(param-1.)/param*a
49
50      nm=matrix(2*pi/(3*a)*sqrt(3*square(n)+square(m)))
51      nm_fact=matrix(multiply(1/(sqrt(9*square(n)+3*square(m))), (multiply(exp(nm*dist), special.erfc(nm*lambd
         +dist/(2*lambd)))+\
52          multiply(exp(-nm*dist), special.erfc(nm*lambd-dist/(2*lambd))))))
53
54      fact_2=2*pi*m/(3*a)
55
56      m_fact=matrix(multiply(1/m, (multiply(exp(fact_2*dist), special.erfc(fact_2*lambd+dist/(2*lambd)))+\
57          multiply(exp(-fact_2*dist), special.erfc(fact_2*lambd-dist/(2*lambd))))))
58
59      fact_3=2*pi*n/(sqrt(3)*a)
60
61      n_fact=matrix(multiply(1/n, (multiply(exp(fact_3*dist), special.erfc(fact_3*lambd+dist/(2*lambd)))+\
62          multiply(exp(-fact_3*dist), special.erfc(fact_3*lambd-dist/(2*lambd))))))
63
64      V_S=zeros((2*N+1,2*N+1))
65      V_L=zeros((N,N))
66
67      for sum_i in range(4):
68          leng=sqrt(square(x-ra[0,sum_i]+n2*sqrt(3)*a)+square(y-ra[1,sum_i]+m2*3*a)+dist**2)
69          V_S=V_S+(-1)**sum_i*multiply((special.erfc(leng)/(2*lambd)), 1/leng)
70
71          ra0=ra[0,sum_i]
72          ra1=ra[1,sum_i]
73
74          V_L=V_L+(-1)**sum_i*(2/a*multiply(nm_fact, multiply(cos(2*pi/(sqrt(3)*a)*n*(x-ra0)),\
75              cos(2*pi/(3*a)*m*(y-ra1))))+\
76              1/(sqrt(3)*N*a)*multiply(m_fact, cos(2*pi/(3*a)*m*(y-ra1)))+\
77              1/(3*N*a)*multiply(n_fact, cos(2*pi/(sqrt(3)*a)*n*(x-ra0))))
78
79
80      V_Stot=sum(V_S) # Short-range potential
81      V_Ltot=sum(V_L) # Long-range potential
82
83      Pot_max =  2.458e-07 # maximal value of the potential computed on a grid of 1000x1000 that cover the
         unit cell of hBN
84
85      pot=(V_Stot+V_Ltot)/Pot_max # computation of the total renormalized potential at position (xpr , ypr)
86
87      return pot
```

Bibliography

[1] D. R. Hofstadter, *Energy levels and wave functions of Bloch electrons in rational and irrational magnetic fields*, Phys. Rev. B **14**, 2239 (1976).

[2] A. H. MacDonald, *Landau-level subband structure of electrons on a square lattice*, Phys. Rev. B **28**, 6713 (1983).

[3] C. R. Dean et al., *Hofstadter's butterfly and the fractal quantum Hall effect in moirée superlattices*, Nat. Lett. **497**, 598 (2013).

[4] R. R. Gerhardts et al., *Magnetoresistance oscillations in a grid potential: Indication of a Hofstadter-type energy spectrum*, Phys. Rev. B **43**, 5192 (1991).

[5] C. Albrecht et al., *Evidence of Hofstadter's fractal energy spectrum in the quantized Hall conductance*, Phys. Rev. Lett. **86**, 147 (2001).

[6] M. C. Geisler, *Detection of a Landau band-coupling-induced rearrangement of the Hofstadter butterfly*, Phys. Rev. Lett. **92**, 256801 (2004).

[7] K. S. Novoselov et al., *Electric Field Effect in Atomically Thin Carbon Films*, Science **306**, 666 (2004).

[8] A. H. Castro Neto et al., *The electronic properties of graphene*, Rev. Mod. Phys. **81**, 109 (2009)

[9] A. K. Geim and K. S. Novoselov, *The rise of graphene*, Nat. Mat. **6**, 183 (2007)

[10] S. Cho and M. S. Fuhrer, *Charge transport and inhomogeneity near the minimum conductivity point in graphene*, Phys. Rev. B **77**, 081402(R) (2008).

[11] Y. Zhang et al., *Origin of spatial charge inhomogeneity in graphene*, Nat. Phys. **5**, 722 (2009)

[12] C. R. Dean et al., *Boron nitride substrates for high-quality graphene electronics*, Nature Nanotech. **5**, 722 (2010)

[13] W. Gannett et al., *Boron nitride substrates for high mobility chemical vapor deposited graphene*, App. Phys Lett. **98**, 242105 (2011)

[14] L. Banszerus et al., *Ballistic Transport Exceeding 28 μm in CVD Grown Graphene*, Nano Lett. **16**, 1387 (2016)

[15] K.I. Bolotin. et al., *Ultrahigh electron mobility in suspended graphene*, Solid State Comm. **146**, 351 (2008)

[16] M. Yankowitz et al., *Emergence of superlattice Dirac points in graphene on hexagonal boron nitride*, Nat. Phys. **8**, 382 (2012)

[17] J. Xue et al., *Scanning tunnelling microscopy and spectroscopy of ultra-flat graphene on hexagonal boron nitride*, Nature Mater. **10**, 282 (2011)

[18] R. Decker et al., *Local electronic properties of graphene on a BN substrate via scanning tunneling microscopy*, Nano Lett. **11**, 2291 (2011)

[19] L. A. Ponomarenko et al., *Cloning of Dirac fermions in graphene superlattices*, Nat. Lett. **497**, 594 (2013).

[20] J. C. Slater and G. F. Koster, *Simplified LCAO method for the periodic potential problem*, Phys. Rev. **94**, 1498 (1954)

[21] P. J. Hasnip, *Density functional theory in the solid state*, Phil. Trans. R. Soc. A **372**, 20130270 (2014)

[22] P. Moon and M. Koshino, *Electronic properties of graphene/hexagonal-boron-nitride moiré superlattice*, Phys. Rev. B **90**, 155406 (2014).

[23] B. Sachs et al., *Adhesion and electronic structure of graphene on hexagonal boron nitride substrates*, Phys. Rev. B **84**, 195414 (2011).

[24] J. Jung et al., *Origin of band gaps in graphene on hexagonal boron nitride*, Nat. Comm. **6**, 6308 (2015)

[25] G. J. Slotman et al., *Effect of structural relaxation on the electronic structure of graphene on hexagonal boron nitride*, Phys. Rev. Lett. **115**, 186801 (2015).

[26] L. A. Chizhova et al., *Graphene quantum dot on boron nitride: Dirac cone replica and Hofstadter butterfly*, Phys. Rev. B **90**, 165404 (2014).

[27] J. Jung et al., *Ab intio theory of moiré superlattice bands in layered two-dimensional materials*, Phys. Rev. B **89**, 205414 (2014).

[28] J. Slawinska et al., *Energy gap tuning in graphene on hexagonal boron nitride bilayer system*, Phys. Rev. B **81**, 155433 (2010).

[29] J. R. Wallbank et al., *Generic miniband structure of graphene on a hexagonal substrate*, Phys. Rev. B **87**, 245408 (2013).

[30] P. San-Jose et al., *Electronic structure of spontaneously strained graphene on hexagonal boron nitride*, Phys. Rev. B **90**, 115152 (2014).

[31] R. Van Noorden et al., *The top 100 papers*, Nat. Lett. **514**, 533 (2014).

[32] P. Hohenberg and W. Kohn, *Inhomogeneous electron gas*, Phys. Rev. B **136**, B864 (1964).

[33] R. O. Jones, *Density functional theory: Its origins, rise to prominence, and future*, Rev. Mod. Phys. **87**, 897 (2015)

[34] D. R. Bowler and T. Miyazaki, $\mathcal{O}(N)$ *methods in electronic structure calculations*, Rep. Prog. Phys. **75**, 036503 (2012)

[35] C. M. Goringe, D. R. Bowler and E Hernandez, *Tight-binding modelling of materials*, Rep. Prog. Phys. **60**, 1447 (1997)

[36] J. E. Lennard-Jones, *The electronic structure of some diatomic molecules*, Trans. Faraday Soc. **25**, 668 (1929)

[37] R. S. Mulliken, *Electronic population analysis on LCAO-MO molecular wave functions*, J. Chem. Phys, **23**, 1833 (1955)

[38] F. Bloch, *Über die quantenmechanik der elekronen in kristallgittern*, Z. Phys. **52**, 555 (1929)

[39] D. A. Papaconstantopoulos and M. J. Mehl, *The Slater-Koster tight-binding method: a computationally efficient and accurate approach*, J. Phys.: Condens. Matter **15**, R413 (2003)

[40] R. Peierls, *On the theory of diamagnetism of conduction electrons*, Z. Phys. **80** 763 (1933)

[41] J. G. Analytis, *Landau levels, molecular orbitals, and the Hofstadter butterfly in finite systems*, Am. J. Phys. **72**, 613 (2004)

[42] J.-C. Charlier et al., *Electronic and transport properties of nanotubes*, Rev. Mod. Phys. **79**, 677 (2007)

[43] M. O. Goerbig, *Electronic properties of graphene in a strong magnetic field*, Rev. Mod. Phys. **83**, 1193 (2011)

[44] P.R. Wallace, *The band theory of graphite*, Phys. Rev. **71**, 622 (1947)

[45] Hwang, C. et al. *Fermi velocity engineering in graphene by substrate modification*, Sci. Rep. **2**, 590 (2012)

[46] K. S. Novoselov et al., *Two-dimensional gas of massless Dirac fermions in graphene*, Nat. Lett. **438**, 197 (2005).

[47] P. A. M. Dirac, *A theory of electrons and protons*, Proc. R. Soc. A **126**, 360 (1930)

[48] R. S. Pease, *An X-ray Study of Boron Nitride*, Acta Cryst **5**, 356 (1952)

[49] W. Paszkowicz et al., *Lattice parameters and anisotropic thermal expansion of hexagonal boron nitride in the 10–297.5 K temperature range*, Appl. Phys. A **75**, 431 (2002)

[50] D. A. Evans et al., *Determination of the optical band-gap energy of cubic and hexagonal boron nitride using luminescence excitation spectroscopy*, J. Phys.: Condens. Matter **20**, 075233 (2008)

[51] X. Z. Du et al., *Temperature dependence of the energy bandgap of two-dimensional hexagonal boron nitride probed by excitonic photoluminescence*, J. App. Phys **115**, 053503 (2014)

[52] G. Cassabois et al., *Hexagonal boron nitride is an indirect bandgap semiconductor*, Nat. Phot. **10**, 262–266 (2016)

[53] N. W. Ashcroft and N. D. Mermin, *Solid State Physics*, Holt, Rinehart and Winston (1976)

[54] T. Ando and Y Uemura, *Theory of quantum transport in a two-dimensional electron system under magnetic fields. I. characteristics of level broadening and transport under strong fields*, J. Phys. Soc. Jpn. **36**, 959 (1974)

[55] M. Kaplitg and J. N. Zemel, *Capacitance observations of Landau levels in surface quantization*, Phys. Rev. Lett. **21**, 212 (1968).

[56] F. F. Fang and P. J. Stiles, *Effects of a tilted magnetic field on a two-dimensional electron gas*, Phys. Rev. **174**, 823 (1968)

[57] G. Abstreiter et al., *Cyclotron Resonance of Electrons in an Inversion Layer on Si*, Phys. Rev. Lett. **32**, 104 (1974).

[58] P. Drude, *Zur Elektronentheorie der Metalle*, Annalen der Physik **306**, 566 (1900)

[59] C. Cohen-Tannoudji et al., *Mécanique quantique*, John Wiley & Sons (1977)

[60] K. v. Klitzing et al., *New Method for high-accuracy determination of the fine-structure constant based on quantized Hall resistance*, Phys. Rev. Lett. **45**, 494 (1980).

[61] B. I. Halperin, *Quantized Hall conductance, current-carrying edge states, and the existence of extended states in a two-dimensional disordered potential*, Phys. Rev. B **25**, 2185 (1982).

[62] M. Buttiker, *Absence of backscattering in the quantum Hall effect in multiprobe conductors*, Phys. Rev. B **38**, 9375 (1988).

[63] N. Pascher et al., *Imaging the Conductance of Integer and Fractional Quantum Hall Edge States*, Phys. rev. X **4**, 011014 (2014)

[64] B Jeckelmann and B Jeanneret, *The quantum Hall effect as an electrical resistance standard*, Rep. Prog. Phys. **64**, 1603 (2001)

[65] Huang et al., *Direct measurement of the spin gaps in a gated GaAs two-dimensional electron gas* Nano. Res. Lett., **8**, 138 (2013)

[66] S. Kim et al., *Spin-polarized to valley-polarized transition in graphene bilayers at $\nu = 0$ in high magnetic fields*, Phys. Rev. Lett. **107**, 016803 (2011).

[67] B.Jeanneret et al., *Observation of the integer quantum Hall effect by magnetic coupling to a Corbino ring*, Phys. Rev. B **51**, 9752 (1995).

[68] Y. Zhang et al., *Experimental observation of the quantum Hall effect and Berry's phase in graphene*, Nat. Lett. **438**, 201 (2005).

[69] P. G. Harper, *The general motion of conduction electrons in a uniform magnetic field, with application to the diamagnetism of metals*, Proc. Phys. Soc. A **68**, 879 (1955)

[70] G. H. Wannier, *A result not dependent on rationality for Bloch electrons in a magnetic field*, Phys. Stat. Sol. B **88**, 757 (1978)

[71] D. J. Thouless, M. Kohmoto, M. P. Nightingale and M. den Nijs, *Quantized Hall conductance in a two-dimensional periodic potential*, Phys. Rev. Lett. **49**, 405 (1982).

[72] A. H. MacDonald, *Landau-level subband structure of electrons on a square lattice*, Phys. Rev. B **28**, 6713 (1983).

[73] R. B. Laughlin, *Quantized Hall conductivity in two dimensions*, Phys. Rev. B **23**, 5632 (1981).

[74] H. Bruus and K. Flensberg, *Many-body quantum theory in condensed matter physics: an introduction*, Oxford University Press (2004)

[75] D. Osadchy and J. E. Avron, *Hofstadter butterfly as quantum phase diagram*, J. Math. Phys. **42**, 5665 (2001)

[76] Patrick Zeller and Sebastian Günther, *What are the possible moiré patterns of graphene on hexagonally packed surfaces? Universal solution for hexagonal coincidence lattices, derived by a geometric construction*, New J. Phys. **16**, 083028 (2014)

[77] C-H. Park et al., *Anisotropic behaviours of massless Dirac fermion in graphene under periodic potentials*, Nature Phys. **4**, 213 (2008)

[78] C-H Park et al., *New generation of massless Dirac fermions in graphene under external periodic potentials*, Phys. Rev. Lett. **101**, 126804 (2008).

[79] C. R. Woods et al., *Commensurate–incommensurate transition in graphene on hexagonal boron nitride*, Nat. Phys. **10**, 451 (2014)

[80] M. Yankowitz et al., *Pressure-induced commensurate stacking of graphene on boron nitride*, Nat. Comm. **7**, 13168 (2016)

[81] S. Reich et al., *Tight-binding description of graphene*, Phys. Rev. B **66**, 035412 (2002).

[82] O. Hod, *Graphite and hexagonal boron-nitride have the same interlayer distance. Why?*, J. Chem. Theory Comput. **8**, 1360 (2012)

[83] Y. Baskin and L. Meyer, *Lattice constants of graphite at low temperatures*, Phys. Rev. **100**, 544 (1955)

[84] B. Van Troeye, M. Torrent and X. Gonze, *Interatomic force constants including the DFT-D dispersion contribution*, Phys. Rev. B **93**, 144304 (2016).

[85] A. Trellakis, *Nonperturbative solution for Bloch electrons in constant magnetic fields*, Phys. Rev. Lett. **91**, 056405 (2003).

[86] Y. Aharonov and D. Bohm, *Significance of electromagnetic potentials in the quantum theory*, Phys. Rev. **115**, 485 (1959)

[87] S. Dubois, *Bloch electrons in constant magnetic fields, a tight-binding description*, Institute of Condensed Matter and Nanosciences (2016)

[88] P. P. Ewald, *Die Berechnung optischer und elektrostatischer Gitterpotentiale*, Ann. Phys. **369**, 253 (1921)

[89] J.-C. Charlier, X. Gonze and J.-P. Michenaud, *First-principles study of the electronic properties of graphite*, Phys. Rev. B **43**, 4579 (1991).

[90] P. Moon et al., *Optical absorption of twisted bilayer graphene with interlayer potential asymmetry*, Phys. Rev. B **90**, 155427 (2014).

[91] L. M. Zhang et al., *Determination of the electronic structure of bilayer graphene from infrared spectroscopy*, Phys. Rev. B **78**, 235408 (2008).

[92] G. M. Rutter et al., *Microscopic polarization in bilayer graphene*, Nat. Phys. **7**, 649–655 (2011)

[93] A. V. Kretinin et al., *Electronic properties of graphene encapsulated with different two-dimensional atomic crystals*, Nano Lett. **14**, 3270 (2014)

[94] M. Yankowitz et al., *Intrinsic disorder in graphene on transition metal dichalcogenide heterostructures*, Nano Lett. **15**, 1925 (2015)

[95] A. Azizi et al., *Freestanding van der Waals heterostructures of graphene and transition metal dichalcogenides*, ACS Nano **9**, 2015 (4882)

[96] A. M. Alsharari, *Mass inversion in graphene by proximity to dichalcogenide monolayer*, Phys. Rev. B **94**, 241106(R) (2016).

[97] J.A. Reyes-Retana and F. Cervantes-Sodi, *Spin-orbital effects in metaldichalcogenide semiconducting monolayers*, Sci. Rep. **6**, 24093 (2016)

[98] U. Von Barth, *Basic density-functional theory—An overview*, Physica Scripta **T109**, 9 (2004)

[99] D. J. Cole and N. D. M. Hine, *Applications of large-scale density functional theory in biology*, J. Phys.: Condens. Matter **28**, 393001 (2016)

[100] W. Kohn and L. J. Sham, *Self-consistent equations including exchange and correlation effects*, Phys. Rev. **140**, A1133 (1965)

[101] A. K. Geim and I. V. Grigorieva, *Van der Waals heterostructures*, Nat. Lett. **499**, 419 (2013).

[102] H. Rydberg et al., *Van der Waals density functional for layered structures*, Phys. Rev. Lett. **91**, 126402 (2003).

[103] K. Lee et al., *Higher-accuracy van der Waals density functional*, Phys. Rev. B **82**, 081101(R) (2010).

[104] K. Berland et al., *van der Waals forces in density functional theory: a review of the vdW-DF method*, Rep. Prog. Phys. **78**, 066501 (2015)

[105] F. Mandl and G. Shaw, *Quantum field theory*, John Wiley & Sons (1984)

[106] Saravan, C. et al., *Sparse matrix multiplications for linear scaling electronic structure calculations in an atom-centered basis set using multiatom blocks*, Comput. Chem. **24**, 618 (2003)

[107] B. Aradi et al., *DFTB+, a Sparse Matrix-Based Implementation of the DFTB Method*, J. Phys. Chem. A **111**, 5678 (2007)

Rue Archimède, 1 bte L6.11.01, 1348 Louvain-la-Neuve **www.uclouvain.be/epl**